PERFORMANCE OF AN AIRFOIL WITH A POWER-SAVING, TAB-ASSISTED FLAP SYSTEM

BY

JOSEPH RYAN BOTTALLA

THESIS

Submitted in partial fulfillment of the requirements
for the degree of Master of Science in Aerospace Engineering
in the Graduate College of the
University of Illinois at Urbana-Champaign, 2011

Urbana, Illinois

Adviser:

Dr. Michael B. Bragg

Abstract

This study investigated the feasibility of reducing control surface input power with the use of a tab-assisted flap. Wind tunnel tests were conducted at the University of Illinois at Urbana-Champaign (UIUC) on a NACA 3415 airfoil model with a flap including a trim tab. Measurements were taken for two configurations: a baseline fixed tab case where tab deflection was zero and a tabbed case where multiple flap and tab angle combinations were tested. Hinge moment measurements were taken for both the flap and tab for comparison between the two cases. In addition; lift, drag and moment measurements along with surface pressures were acquired to aid in the analysis of the concept and provide flow diagnostics. The data were compared to computational results which compared well with the exception of flap and tab deflection cases where large regions of unsteady separated flow were present. All data were taken at a Reynolds number of 1.8 million and Mach number of 0.18.

To analyze the power-savings capability of a tab-assisted flap, several studies were conducted: a generalized tab performance study evaluating hinge moment reduction and a quasi-dynamic study using the static data to calculate work savings for two simulated flap deflections. The generalized tab performance study revealed large hinge moment reductions for each of the flap deflections when using the tab to actuate the flap. These reductions came at the cost of increased drag, reduced lift and loss of flap effectiveness. The quasi-dynamic study produced significantly large work savings for both simulated flap deflection schedules. Even though this study ignored the effect on lift and drag, as well as the unsteady aerodynamics and control surface inertia, it suggests the large power-savings potential of a tab-assisted flap.

A flow visualization analysis was performed to further assess the loss of flap effectiveness observed in the tab performance calculations as well as the non-linear behavior in the lift, drag and hinge moment data. The results of the analysis showed the complex flowfield behavior in cases where the flap and tab deflections were of opposite sign and larger magnitude and identified the cause of behavior in other cases where data non-linearities existed.

Acknowledgments

First, I would like to thank my advisor, Professor Michael B. Bragg, for allowing me the opportunity to work in his research group and for the guidance and assistance given over my years as an undergraduate and graduate research assistant. I would also like to thank Phil Ansell for his extensive help during the initial wind-tunnel experimentation and his work on the LabView code.

This work was funded by The Boeing Company and supported by James J. Sheahan Jr., so I would like to thank him as well as Chad Winkler for providing the supporting computational investigation. Lastly, I would not be where I am now without the encouragement and support of my family and fiancée Hannah.

Table of Contents

List of Tables

List of Figures

Nomenclature

A	Axial force from balance
A_{ss}	Wind tunnel inlet settling section area
A_{ts}	Wind tunnel test section area
b	Model span
c	Model chord
c_f	Model flap chord
c_s	Model control surface chord (flap or tab)
c_t	Model tab chord
C	Test-section area
C_d	Drag coefficient
C_h	Hinge moment coefficient
$\overline{C_h}$	Hinge moment coefficient average over total number of samples
$C_{h,StDev}$	Standard deviation of the hinge moment coefficient sample
C_l	Lift coefficient
$C_{l,max}$	Maximum lift coefficient
C_m	Quarter-chord pitching moment coefficient
C_p	Pressure coefficient
D	Drag
D'	Drag per unit span
d_h	Calibration hinge moment arm for flap or tab
d_s	Flap or tab hinge moment arm
F_A	Axial force
$F_{A'}$	Axial force per unit span
F_N	Normal force
$F_{N'}$	Normal force per unit span

F_h	Load applied to hinge moment balance
h	Test-section height
H	Hinge moment
H'	Hinge moment per unit span
K	Reduced frequency
K_1	Body-shape factor
L	Lift
L'	Lift per unit span
M	Mach number
M	Pitching moment
$M_{c/4}$	Quarter-chord pitching moment
$M'_{c/4}$	Quarter-chord pitching moment per unit span
n	Number of model pressure taps
n_{rake}	Number of wake rake total pressure measurements
n_s	Number of flap or tab pressure taps
N	Number of samples
N	Normal force
P	Characteristic static pressure
$P_{0,\infty}$	Freestream total pressure
$P_{0,w}$	Wake total pressure
P_{amb}	Ambient air pressure
P_s	Model surface static pressure
P_{ss}	Wind-tunnel inlet settling section static pressure
P_{ts}	Wind-tunnel test section static pressure
q_∞	Dynamic pressure
R	Ideal gas constant for air
R	General result uncertainty
Re	Reynolds number based on chord length
RR_A	Axial force range ratio
RR_M	Pitching moment range ratio
RR_N	Normal force range ratio

S	Model area
S_f	Flap area
S_s	Control surface area (flap or tab)
S_t	Tab area
t	Model thickness
T_{amb}	Ambient air temperature
U	Uncertainty
U	Characteristic velocity
U_{ss}	Inlet settling section velocity
U_{ts}	Test section velocity
U_∞	Freestream velocity
V_A	Scaled axial force voltage
V_M	Scaled pitching moment voltage
V_N	Scaled normal force voltage
V_{0A}	Tared axial force voltage
V_{0M}	Tared pitching moment voltage
V_{0N}	Tared normal force voltage
W	Test-section width
x	Model coordinate in chordwise direction
x/c	Coordinate in chordwise direction non-dimensionalized by the chord
x_o	Chordwise offset of model from balance center
y	Model coordinate in normal direction
y_o	Normal offset of model from balance center

Greek Symbols

α	Model angle of attack
α_{stall}	Angle of attack of maximum lift
δ_f	Flap deflection angle
δ_s	Control surface deflection angle (flap or tab)
δ_t	Tab deflection angle

$\delta_{t,trim}$	Tab deflection angle for zero flap hinge moment (trim)
ΔP	$P_{ss} - P_{ts}$
ε	Total velocity increment
ε_{sb}	Solid-blockage velocity increment
ε_{wb}	Wake-blockage velocity increment
ρ	Air density
ρ_{amb}	Ambient air density
σ	Wall correction simplifying parameter
μ	Dynamic viscosity
ω	Angular velocity

Acronyms

A/D	Analog to Digital
ASTM	American Society for Testing and Materials
CFD	Computational fluid dynamics
DDES	Delayed detached-eddy simulation
ESP	Electronically Scanned Pressure
GPIB	General Purpose Interface Bus
NACA	National Advisory Committee on Aeronautics
PCU	Pressure Calibration Unit
PSI	Pressure Systems Incorporated
RMS	Root-Mean-Square
RSS	Root-Sum-Square
SLA	Stereolithography apparatus
TMA	Thermal-mechanical analysis
UIUC	University of Illinois at Urbana-Champaign

Chapter 1

Introduction

Aircraft are controlled in part through the use of control surfaces such as ailerons, elevators, rudders and flaps which, through their position, affect the airflow over the surface. The change in the airflow over the surface influences the lift on that surface and over a moment arm induces a moment. The moment then translates into aircraft roll, pitch or yaw. Flight control systems have progressed from simple manual systems, implementing cables, pulleys and pushrods, to complex fly-by-wire systems as the size and complexity of aircraft, as well as the availability of newer technology, have grown in the past century.

With conventional commercial aircraft designs being replaced by next generation air vehicles, implementation of new technologies will be required. Thinner wings will require installation of control systems in a much smaller volume. Supercritical airfoil shapes require higher holding loads resulting in thermal issues. These issues along with the migration towards more electric aircraft necessitate a flight control actuation system that reduces size, weight, and power/thermal requirements.[1]

Additionally, aircraft such as the blended-wing body will have control surfaces up to 15 feet in chordwise extent and thicknesses up to 6 feet at the hinge location. Actuating such a surface necessitates large amounts of power to supply the larger actuators. With the increase of power, supply power sources become larger and heat rejection needs increase dramatically. To reduce the thermal impact and power requirements for the flight controls, an alternate approach for flight control needs to be developed.[1]

One such approach is the use of tabs on the control surface which, through deflection, create aerodynamic forces that assist movement or reduce the control force/hinge moment of the larger control surface.

1.1 Previous Work on Airfoils with a Flap and Tab

The effects of tabs on other surfaces have been studied since the NACA research of Holtzclaw and Crane,[2] in 1944, where wind-tunnel tests were performed on a NACA (66)2-216 airfoil model with 20%-chord tabbed ailerons. This experiment was the last of three parts looking at the general effects on lift and hinge moments for two different airfoil profiles. The first two parts examined the aerodynamic effects of modifying the aileron profile and trailing-edge shape. The tests were performed in the Ames Aeronautical Laboratory 7 by 10 foot wind tunnel at Reynolds numbers of 5.5, 6.7 and 9 million. Data were taken to determine the incremental change in section lift coefficient due to tab and aileron deflection and the resulting hinge moment coefficient on both the tab and aileron. Significant effects were seen on the section lift and aileron hinge moment coefficient for each of the aileron and tab shapes run.

Another investigation by Wenzinger[3] measured the pressure distributions over a Clark Y airfoil with a flap and tab. The pressure measurements were then used to calculate the normal force and pitching moment coefficients as well as the hinge moments for both the flap and tab. The incremental tab normal-force and hinge-moment coefficients with tab deflection for a given flap deflection were found to vary independent of the flap deflection. Independence was also observed for the airfoil and flap incremental coefficients but with tab deflection. The measured values were also compared to theoretical calculations and showed good agreement.

While the experiments by Holtzclaw and Crane[2] and Wenzinger[3] studied the general effect of a flap and tab system, several studies focused on a given mode of operation. These modes of operation include ground-adjustable, balancing, anti-balancing, trimming and active control (servo tab). In 1936 Jones and Nerken[4] completed a study on the hinge moment reduction with ground-adjustable fixed tabs for ailerons. These tabs were installed and ground-adjusted to several different downward deflections which trimmed the ailerons upward. The resulting conclusion was that a small fixed tab was beneficial in reducing control forces when deflected downward.[4] Two years later, Soulé and Hootman[5] conducted the same experiment but with a flight test program. While the tabs were found to reduce stick forces, it was left to the discretion of the pilots themselves to determine the relative control forces. The research determined that fixed tabs were impractical for reduction of hinge moments.

A balancing tab differs from a ground-adjustable tab in that it remains active in flight but is not actively controlled in the manner of a servo tab. The purpose is to reduce control force/hinge moment similar to that of the servo tab. A pilot controls the main control surface and the balancing tab would be linked in a way that would cause the tab to deflect in the opposite direction reducing the control force. An anti-balancing tab, which acts in the opposite direction of a balancing tab, is utilized in a situation where larger control forces are necessary for stability in addition to increased surface effectiveness.

A study on the use of balancing tabs on ailerons was conducted by Sears[6] in 1942 in which section hinge moment data from previous wind-tunnel results were used to calculate the necessary tab chord lengths and deflection to produce a constant aileron hinge moment independent of aileron deflection and still maintain the same roll rate. It was concluded that a balancing tab was an effective method of reducing the aileron hinge moment to zero or to the prescribed aileron hinge moment. Additionally, a loss of lift effectiveness was noted that needed to be counteracted by a larger aileron deflection.[6]

The active control and trimming modes of operation were studied in a NACA study by Harris[7] wherein the effects of different geometries of tabs on each of the typical aircraft control surfaces (aileron, elevator and rudder) were surveyed. Trimming was also implemented by either direct control, as typically used today on elevators, or by ground fixing. Data were taken for hinge moment reductions as well as the effect on the normal force coefficient, from which the lift and drag penalties could be found. Results indicated a large potential savings for each control surface but were limited to smaller deflections. The savings were maximized at an angle of attack of zero degrees.[7]

Recently, Ansell[8] performed wind-tunnel experimentation with a NACA 3415 airfoil model to assess the feasibility of providing stall warning by utilizing flap and control surface hinge moments for models with and without contamination. A fixed tab was later added to find its effect on the unsteady hinge moment.[9] While this was a fixed tab, the tests provided valuable hinge moment data and an established experimental methodology for an airfoil with a flap and tab system. These methods would be adapted for the experiment documented in this paper.

1.2 Research Motivation

As shown, there have been many studies on the effect of tabs on control surfaces in a static deflection scenario. Active control methods, such as servo tabs, have already been implemented on aircraft such as the Boeing 707 and 727. For next generation air vehicles, an active-control tab-assisted control surface would be an effective method of reducing flight control power requirements and thermal impact, but would require a more complex method of application than that previously used or studied.

The proposed mode of operation for this experiment is simple - the tab is moved to a fully deflected position that results in air loads that provide actuation for the primary flap system. When the surface reaches its commanded position the surface is locked in place and the tab returns to its neutral position resulting in full surface aerodynamic authority while using a fraction of the power that direct flap actuation would have required. Based on the current desire to produce more electric aircraft this system was developed using electro-mechanical actuators (EMAs). Further details pertaining to this mode of operation are documented by Sheahan et al.[10] Using math models of the flight control system a simulation was performed of the flight surface motion and actuator. With this configuration the tab can be held stationery and used as part of the flight control surface, when full authority is required. Based on these simulations, the tab and primary surface working together in this way results in reducing the power required by as much as 90% during specific portions of the duty cycle and 50% over the flight duration.[1]

To date, no wind-tunnel experiments have attempted to simulate a dynamic scenario, such as the one detailed above. Therefore, the actual power savings and aerodynamic effects of such a system have not been verified. Thus, the long-term motivation of this experiment is to understand the power-savings capabilities of a tab-assisted flap operated as described above and by Sheahan et al.[10]

1.3 Objectives and Approach

Due to the complexity of a wind-tunnel experiment with dynamic movement of a flap and tab, the proposed testing plan was divided into two phases: an initial wind-tunnel test examining the static effects of a tab-assisted flap and a second wind-tunnel entry in which the mode of

operation would be simulated. The initial wind-tunnel experiment would also serve as a preliminary verification of the power-savings capability of a tab-assisted flap and of a computational fluid dynamic (CFD) analysis. Furthermore, methods of independent flap and tab movement would be analyzed and optimized for continued use in the realistic simulation or dynamic phase of the experiment.

An initial study of the actuation systems needed for such a simulation has presented challenges for matching the unsteady aerodynamics of the proposed full-scale system to the small-scale wind-tunnel model. The important variable to be matched is the reduced frequency, *K*, shown below in Eq. 1.1, which is a function of the chord lengths, freestream velocity and control surface angular velocity.

$$K = \frac{\omega c}{2U_\infty} \tag{1.1}$$

As a result, the scaled angular frequency becomes quite large to match the full-scale reduced frequency. A complex actuation system would then be required in order to handle the significant inertia and short actuation times of both the flap and tab.

Despite the inherent challenges, a dynamic simulation would provide validation of the math model simulations and lead the way to an in-flight application. The goal of the initial static experiment to be detailed in this paper will offer valuable information and methods in preparation for the dynamic experiment.

To summarize, the approach for this experiment was simplified to examine the effects of a tab deflection on the aerodynamic performance and hinge moment under a fixed flap deflection. This paper will present the data from both the experimental and computational investigations[1] in order to identify and understand the following:

- The aerodynamic performance of a NACA 3415 airfoil with different flap deflections and a fixed tab.
- The combined effect of a flap and tab on the aerodynamic performance of the NACA 3415 airfoil.
- Generalized tab performance with respect to the hinge moment reduction between the fixed tab and tab deflected cases as well as the tradeoffs in potential drag increase and loss of lift.

- Potential power-savings capability of a tab-assisted flap through a hypothetical study using the measured static data in this experiment.

Chapter 2

Experimental Methodology

This section describes the details pertaining to methods and facilities for the aerodynamic testing performed at the University of Illinois at Urbana-Champaign (UIUC). This includes test equipment, data acquisition and flow visualization techniques. Lastly, the test matrix for the wind-tunnel experimentation will be given.

2.1 Aerodynamic Testing

The experimental study was performed at the Aerodynamics Research Laboratory at the University of Illinois at Urbana-Champaign. The two subsonic wind tunnels in the lab are located in the test high bay while the data acquisition equipment is contained within the control room. A schematic layout of the laboratory is shown in Fig. 2.1.

2.1.1 Wind Tunnel

All of the aerodynamic testing was conducted in a subsonic, open-return, low-turbulence-type wind tunnel. The wind-tunnel test section measured 2.8-ft high by 4-ft wide and was 8-ft long and the inlet to test section area ratio was 7.5:1. To account for the growth in the wall boundary layer, the test section was 0.5 inches wider at the downstream end relative to the upstream end. Installed in the inlet were four anti-turbulence screens and a 4-in thick honeycomb flow straightener that effectively reduced the freestream turbulence intensity to less than 0.1% for all operating speeds. A drawing of the wind tunnel is shown in Fig. 2.2.

The tunnel was powered by a 125-hp AC motor which drives a five-bladed fan allowing for an approximate maximum setting of 1200 rpm, thus resulting in a maximum empty test-section flow speed of 165 mph. This flow speed produced a maximum Reynolds number (*Re*) of

1.5 million per foot and was computer-controlled within 2% during testing. The Reynolds number was calculated as shown below in Eq. 2.1.

$$Re = \frac{\rho U_\infty c}{\mu} \tag{2.1}$$

The test section speed was calculated using the pressure difference between the inlet settling section and the test section ($P_{ss} - P_{ts}$). The pressure difference was measured with a Setra 239 differential pressure transducer. The transducer was fed by two tubes, one leading to a set of four pressure taps located just downstream of the anti-turbulence screens and one leading to another set of four pressure taps located just upstream of the test section. Each set of four pressure taps provided an average pressure for each location, P_{ss} and P_{ts}, which, using the law of conservation of mass (Eq. 2.2) and Bernoulli's equation (Eq. 2.3), could be used to calculate the test section airspeed as seen in Eq. 2.4. For this calculation, it was assumed the flow was steady and inviscid.

$$A_{ss}U_{ss} = A_{ts}U_{ts} \tag{2.2}$$

$$\frac{1}{2}\rho U_{ts}^2 + P_{ts} = \frac{1}{2}\rho U_{ss}^2 + P_{ss} \tag{2.3}$$

$$U_{ts} = \sqrt{\frac{2(P_{ss} - P_{ts})}{\rho_{amb}\left(1 - \left(\frac{A_{ts}}{A_{ss}}\right)^2\right)}} \tag{2.4}$$

In Eq. 2.4 above, ρ_{amb} is the ambient density calculated using the ideal gas law, Eq. 2.5 below, where, P_{amb}, and, T_{amb}, were measured using a Setra 270 pressure transducer and Omega thermocouple, respectively and R was the ideal gas constant for air. Both the transducer and the thermocouple were located in the high bay.

$$\rho_{amb} = \frac{P_{amb}}{RT_{amb}} \tag{2.5}$$

2.1.2 Airfoil Model

The airfoil model used for the experimental investigation was a NACA 3415 which had an 18-in chord and a 33.563-in span. The model was originally fit with a 25%-chord flap but was replaced for this experiment by a 25%-chord flap incorporating a tab which was 25% of the flap chord. The model was installed vertically in the test section which was accomplished by a removable ceiling and overhead crane to lower the model into position. The model was then held in place by brackets, mounted to the force balance, clamped around the two internal spars protruding from the base of the model. These spars were fed through a cover plate that was machined specifically for the 3415 model to allow for tight tolerances with the spars which minimize air leakage into the test section. This cover plate was further modified for this experiment to allow for the movement of the tab spar through the range of flap deflections. A gap of around 0.02 inches between the model and tunnel floor was also maintained through the use of spacers during installation to ensure all of the loads and moments were transferred to the force balance without interference from model-floor contact.

Once installed, the ceiling was replaced and an adjustable stiffener was bolted to it to create a gap of .125 inches between the model and the ceiling. This gap prevented contact between the ceiling and model during testing since the pressure drop within the test section caused the ceiling to deflect inward reducing the gap by more than half. Scotch book tape was used to cover all gaps and cracks within and outside of the tunnel to minimize leakage. A schematic of the wind-tunnel model setup is shown in Fig. 2.3.

The NACA 3415 model was equipped with a series of surface pressure taps to measure the pressures on the airfoil surface. The locations of the pressure taps are shown in Fig. 2.4. A total of 77 chord-wise taps were distributed between the main element, flap and tab surfaces. The majority of the pressure taps were installed in the main element with 40 taps on the upper surface and 23 on the lower surface. The flap had 7 upper surface taps and 5 lower surface taps while the tab had one on each surface and one on the trailing-edge surface. The taps between the leading edge and mid-chord were aligned and offset to the flow direction by approximately 15° to prevent flow interference from flow transition.

2.1.3 Data Acquisition System

The data for this experiment were taken with software programmed using LabView™. A graphical user interface within the software allowed for actions to be performed by clicking

buttons and entering numbers on the main display. The commands from the computer would then be relayed to the tunnel variable-frequency drive controller, three-component balance, IDC and Velmex stepper-motor drives via RS-232 communication. The data acquisition computer was a Dell Precision T3400 with an Intel® Core™ 2 Duo processor clocked at 2.83 GHz with 4 GB of memory and run using a Windows XP 32-bit operating system.

The model and wake survey pressure measurements were taken through a National Instruments General Purpose Interface Bus (GPIB) IEEE-488 board. A National Instruments analog to digital (A/D) conversion board was used to convert the data from both the three-component balance and hinge moment balance.

2.1.4 Force and Moment Balance

In addition to using the measured airfoil surface pressures to obtain the lift, drag and pitching moment data, a three-component force and moment balance, manufactured by Aerotech ATE Limited, was also used to acquire the data. The balance can be seen in Fig. 2.5. With the model clamped between the brackets bolted into the force plate on the balance, the loads were measured with three load cells which provided an axial and normal force along with a moment about the center of the balance. The load cells produced a full-scale output voltage of ±20 mV and, using a signal conditioning system, was low-passed filtered at 1 Hz and amplified to a full-scale voltage of ±5 V. The measurements could be obtained in three different load ranges, shown below in Table 2.1. The high range was used for all measurements in this experiment.

Table 2.1 Balance load ranges.

	High Range	*Medium Range*	*Low Range*
Normal Force	±450 lbs.	±225 lbs.	±90 lbs.
Axial Force	±90 lbs.	±55 lbs.	±18 lbs.
Pitching Moment	±45 ft-lbs.	±30 ft-lbs.	±15 ft-lbs.

Each voltage recorded was the average of 200 samples taken at a rate of 100 Hz. The force balance also controlled the angle of attack of the model to within 0.1°. Tare voltages were taken for each angle of attack in the entire range before each run. These final voltages were first multiplied by the appropriate range ratio, shown below in Table 2.2, then placed in the calibration matrix for the force balance (Eq. 2.6) to find the normal and axial forces as well as

the moment about the center of the balance. Since the high range was the only range used in this experiment, the range ratio was simply 1.

Table 2.2 Force balance range ratios.

	High Range	*Medium Range*	*Low Range*
Normal, RR_N	1	0.4944	0.2046
Axial, RR_A	1	0.6278	0.2173
Moment, RR_M	1	0.6755	0.3413

$$\begin{Bmatrix} F_N \\ F_A \\ M \end{Bmatrix} = \begin{bmatrix} 37.7 & 0.01359 & -0.2095 & 0.01094 & 0 & -0.000865 \\ -0.1607 & 8.3125 & -0.01638 & 0.007084 & 0 & 0.007660 \\ -0.01299 & -0.005521 & 1.247 & -0.002122 & 0 & 0.0001497 \end{bmatrix} \begin{Bmatrix} V_N \\ V_A \\ V_M \\ V_N^2 \\ V_A^2 \\ V_M^2 \end{Bmatrix} \tag{2.6}$$

The resulting normal and axial forces were used to calculate the lift and drag coefficients with Eqs. 2.7 and 2.8 below. Since the moment was measured relative to the center of the balance, a translation to the quarter-chord of the model was needed due to the slight offset in the *x* and *y* directions. In Eq. 2.9 for the quarter-chord moment coefficient, these are denoted by x_o and y_o, which were -0.25 in. and 0.51 in., respectively.

$$C_l = \frac{1}{q_\infty S}(F_N \cos\alpha - F_A \sin\alpha) \tag{2.7}$$

$$C_d = \frac{1}{q_\infty S}(F_N \sin\alpha + F_A \cos\alpha) \tag{2.8}$$

$$C_m = \frac{1}{q_\infty S c}(M + F_N x_o + F_A y_o) \tag{2.9}$$

The drag calculation was used only for comparison purposes due to the presence of an induced drag component. The induced drag results from the small gap between the model and

test section ceiling and floor and causes the drag data at non-zero lift to be slightly higher than that measured by the wake survey system.

2.1.5 Flap and Tab Hinge Balance

Two linear traverse systems were used to control the flap and tab in order to deflect the two surfaces independently of each other. The flap was controlled by a Velmex UniSlide™ A40-08 single-axis linear traverse which connected to the flap spar by a two-arm linkage and was regulated by a Velmex VP9000 Controller. The linkage system consisted of a clamp arm fixed to the flap spar and a connecting arm that integrates an Omegadyne LCFD-50 load cell which was fixed to the linear traverse through an upright support attached to the traverse plate. The load cell measured the hinge moments to the flap through the measurement of the forces in the flap linkage. The traverse assembly was attached to an L-shaped plate which mounted to the force plate.

An additional and similar traverse and linkage system was designed to measure the tab hinge moment. The traverse was a Zaber T-LSM100 and included an integrated controller. It was mounted to the flap clamp arm which was modified by adding a platform for mounting the tab traverse. The tab-linkage system consisted of another clamp arm which attached to the tab spar and a connecting arm, similar to that of the flap linkage system, which incorporated an Omegadyne LCMFD-100N and attached to the tab traverse by an identical upright support. A schematic of the system along with computer-aided design images are shown below in Figs. 2.6, 2.7 and 2.8, respectively.

Both control surfaces were calibrated over a range of flap/tab deflections using the same method by applying a prescribed hinge moment and measuring the voltage induced in the load cell. To accomplish this, weights were applied to a known, fixed moment arm for each of the tested flap and tab deflections. The system included a clamp with padded casters, which attaches to the trailing edge of the flap, with a cable fixed to the end which runs over a pulley to the applied weights. This same system concept was also implemented to calibrate the tab utilizing another clamp designed to fit the smaller control surface. The clamp was simply two pieces of .25 in thick aluminum that were fixed at one end and bent outward on the other to fit over the tab and was affixed to the tab. A cable was attached to the end extended out from the tab so that the same pulley and weight system could again be used.

The flap was calibrated for deflections (δ_f) of 0, ±5, ±10, ±20, and ±30 deg. while the tab was calibrated for deflections (δ_t) of 0, ±10, ±20, ±30, ±45 and ±60 deg. The moment arms for the flap and tab were 6.25 and 3.50 in., respectively. The signal conditioner gain was set to ensure the maximum load on either the flap or tab would not exceed the maximum voltage of 5V. This maximum load was determined from estimated aerodynamic loads on both surfaces. The calibration hinge moment (H) for both surfaces was calculated using the equation,

$$H = Fd_s(cos\delta_s) \tag{2.10}$$

where F is the load applied at a moment arm, d_s, and δ_s is the deflection angle for either the flap or the tab. The calibration hinge moment values were then plotted with voltage for each deflection angle and for both surfaces, from which the calibration constants could be found with a linear curve fit.

The frequency of the signal conditioner was set to 3000 measurements per second (3 kHz) for a period of 10 seconds. The hinge moment would then be calculated using Eq. 2.11 below,

$$C_h = \frac{H}{q_\infty S_s c_s} \tag{2.11}$$

where S_s is the reference area of the surface and c_s is the surface chord.

The time-averaged hinge moment coefficient was then calculated as follows for N number of samples:

$$\bar{C_h} = \frac{1}{N}\sum_{i=1}^{N} C_{h_i} \tag{2.12}$$

To account for the unsteady nature of the hinge moment measurements, the standard deviation of the measurements was calculated, $C_{h,StDev}$. The standard deviation gave the amount and magnitude of variation between the measurements and mean hinge moment coefficient. The calculation of $C_{h,StDev}$ is presented below as Eq. 2.13.

$$C_{h,StDev} = \sqrt{\frac{1}{N}\sum_{i=1}^{N}\left(C_{h_i} - \bar{C}_h\right)^2} \tag{2.13}$$

2.1.6 Pressure Measurement System

The pressures were obtained through static pressure taps on the airfoil surface, documented in Section 2.1.2. Stainless steel tubing of 0.042 in. outer diameter was connected to the taps and either polyurethane or vinyl tubing was run from stainless steel tubing to the pressure transducers. Each of the transducers, Miniature Electronically Scanned Pressure (ESP) units, took pressure measurements at 50 Hz for two seconds and had 32 pressure ports.

Five transducers were necessary to complete the measurements for the entire model and wake pressure rake, to be discussed in Section 2.1.7. A ±5 psid unit was used to measure the pressure from the taps in the leading-edge region while two ±1 psid units measured the pressures on the rest of the model. This was due to the larger pressure differentials at the leading edge necessitating the ±5 psid ESP unit. Additionally, two ±0.35 psid units measured the pressures from the wake survey system.

To calculate the pressure coefficient distribution on the airfoil, the dynamic pressure, q_∞, was needed and was calculated as follows:

$$q_\infty = \frac{1}{2}\rho_\infty U_\infty^2 \tag{2.14}$$

From Bernoulli's equation (Eq. 2.3) and conservation of mass (Eq. 2.2) for an incompressible fluid, we obtain from Eq. 2.15:

$$q_\infty = \frac{1}{2}\rho_\infty U_{ts}^2 = \frac{P_{ss} - P_{ts}}{1 - \left(\frac{A_{ts}}{A_{ss}}\right)^2} \tag{2.15}$$

The surface pressure coefficients (C_p) were then found using the standard equation:

$$C_p = \frac{P_s - P_\infty}{q_\infty} = \frac{P_s - P_{ts}}{P_{ss} - P_{ts}}\left[1 - \left(\frac{A_{ts}}{A_{ss}}\right)^2\right] \tag{2.16}$$

with P_s representing the static pressure on the airfoil surface. The quantity ($P_s - P_{ts}$) was the actual measurement taken by the ESP units which are referenced to the test section static pressure. The quantity ($P_{ss} - P_{ts}$) was also directly measured by a single port in one of the ESP units which was connected to the settling section.

The pressure measurements were also used to calculate the lift and moment of the airfoil from a method detailed by Anderson.[11] This was done by dividing the airfoil surface into panels and assuming the panels were located between two adjacent pressure taps in the chordwise direction. The pressure measured by the taps was then broken into axial and normal components which are shown below in Eqs. 2.17 and 2.18.

$$\Delta F_{N_i'} = \frac{P_i + P_{i+1}}{2}(x_{i+1} - x_i) \tag{2.17}$$

$$\Delta F_{A_i'} = -\frac{P_i + P_{i+1}}{2}(y_{i+1} - y_i) \tag{2.18}$$

The components for each panel could then be summed for each of the panels over the airfoil surface to find the total normal and axial forces, F_N and F_A. The lift could then be calculated using Eq. 2.19 with these total forces.

$$L' = F_{N'}\cos\alpha + F_{A'}\sin\alpha \tag{2.19}$$

The quarter-chord pitching moment was calculated with the force components at each panel and the moment arm between the panel and airfoil quarter-chord location. The equation to calculate the increment of $M_{c/4}$ for each panel is as follows in Eq. 2.20. Summing up each panel increment produces the net airfoil $M_{c/4}$ (Eq. 2.21).

$$\Delta M'_{c/4_i} = \Delta F_{N'_i}\left(x_{c/4} - \frac{x_i + x_{i+1}}{2}\right) + \Delta F_{A'_i}\left(\frac{y_i + y_{i+1}}{2}\right) \tag{2.20}$$

$$M'_{c/4} = \sum_{i=1}^{n-1} \Delta M'_{c/4_i} \tag{2.21}$$

This method was also used to calculate the hinge moment for both the flap and tab, the only differences being that the moment was taken about the hinge location and not the quarter-chord, and the pressure taps located on the particular surface were the only taps used in the calculation. The equation for the increment in hinge moment for either surface is given as the following, with x_h and y_h representing the hinge location for the surface:

$$\Delta H'_i = \Delta F_{N'_i}\left(x_h - \frac{x_i + x_{i+1}}{2}\right) + \Delta F_{A'_i}\left(\frac{y_i + y_{i+1}}{2} - y_h\right) \tag{2.22}$$

This increment could then be summed over the surface for each of the panels to obtain the net hinge moment.

$$H' = \sum_{i=1}^{n_s-1} \Delta H'_i \tag{2.23}$$

where n_s denotes the number of taps for the given surface, flap or tab. The calculated forces and moments per unit span (Eqs. 2.19, 2.21 and 2.23) were then converted to the respective coefficients with Eqs. 2.24 - 2.26.

$$C_l = \frac{L'}{q_\infty c} \tag{2.24}$$

$$C_m = \frac{M'}{q_\infty c^2} \tag{2.25}$$

$$C_h = \frac{H'}{q_\infty c_s^2} \tag{2.26}$$

It is important to note that since these are calculated from pressure taps that are located in the center of the airfoil in the spanwise direction, the lift and quarter-chord pitching moments only represent the center section of the airfoil. The lift and pitching moment calculated using the force and moment balance in Section 2.1.4 differ in that they represent the entire span of the model. Thus, differences between the two calculations can occur.

2.1.7 Wake Survey System

A traversable wake rake was used for the primary drag measurement. The rake was 9.75 in. wide and contained 59 total pressure probes, of 0.04 in. outer diameter, and 3 static pressure probes oriented parallel to the freestream flow. The outer probes were spaced at 0.27 in. while the middle probes had 0.135 in. spacing. The rake was controlled by two Lintech traverse axes and an IDC S6962 Stepper Motor Drive allowing it to move vertically across the span of the model as well as horizontally. This control system was located in a pressure box which was sealed to limit the leakage into the test section. The main LabVIEW program controlled the wake rake to ensure the entire wake was captured by starting at the point of minimum pressure and traversing horizontally in both directions until an area of constant pressure was encountered, thus signaling the edge of the wake. A visual of the wake rake installed in the wind tunnel is shown in Fig. 2.9.

The program implemented a standard momentum deficit method given by Jones[12] to calculate the drag based on the wake measurements. It assumes wake pressures are measured in a plane perpendicular to the freestream and far enough downstream of the airfoil so that the static pressure in the wake, P_w, was equal to that of the freestream, P_∞. This allows the drag per unit span to be expressed as:

$$D' = \rho \int u_1 (U_\infty - u_1) dy_1 \tag{2.27}$$

Another plane closer to the airfoil where the actual measurements were taken is assumed and conservation of mass is applied to the streamtube between the two planes, represented in Eq. 2.28 below, which is then placed back into Eq. 2.27 producing Eq. 2.29.

$$u_1 dy_1 = u_w dy \tag{2.28}$$

$$D' = \rho \int u_w (U_\infty - u_1) dy \tag{2.29}$$

The total pressure of the freestream, plane 1 and wake plane can be broken into the static and dynamic components as shown in Eqs. 2.30, 2.31, and 2.32, respectively.

$$P_\infty + \frac{1}{2}\rho U_\infty^2 = P_{0,\infty} \tag{2.30}$$

$$P_\infty + \frac{1}{2}\rho u_1^2 = P_{0,1} \tag{2.31}$$

$$P_\infty + \frac{1}{2}\rho u_w^2 = P_{0,w} \tag{2.32}$$

Solving for U_∞, u_1 and u_w and assuming total pressure is constant between the wake-rake plane and plane 1, $P_{0,1} = P_{0,w}$, substitution into Eq. 2.29 provides the following:

$$D' = 2 \int \sqrt{P_{0,w} - P_w}\left(\sqrt{P_{0,\infty} - P_\infty} - \sqrt{P_{0,w} - P_\infty}\right) dy \tag{2.33}$$

By assuming $P_w = P_\infty$, Eqs. 2.30 and 2.32 can be combined to form:

$$q_w = q_\infty - \left(P_{0,\infty} - P_{0,w}\right) \tag{2.34}$$

Equation 2.33 can be rearranged, as suggested by Lee,[13] by writing in terms of dynamic pressure and substituting in Eq. 2.34 for q_w. This results in the following:

$$D' = 2 \int \sqrt{q_\infty - \left(P_{0,\infty} - P_{0,w}\right)}\left(\sqrt{q_\infty} - \sqrt{q_\infty - \left(P_{0,\infty} - P_{0,w}\right)}\right) dy \tag{2.35}$$

The pressure difference, $P_{0,\infty}$ - $P_{0,w}$, can be calculated directly through the wake measurements since $P_{0,w} - P_{atm}$ is the measured quantity in the wake and $P_{0,\infty} - P_{atm}$ is equal to $P_{0,w} - P_{atm}$ at the edge of the wake. If the latter two expressions are subtracted, an equation for $P_{0,\infty} - P_{0,w}$ can be

obtained (Eq. 2.36). Substituting this expression into Eq. 2.35 allows for the calculation of drag directly from measured pressures.

$$P_{0,\infty} - P_{0,w} = \left(P_{0,\infty} - P_{atm}\right) - \left(P_{0,w} - P_{atm}\right) \tag{2.36}$$

The value of the integral for drag was calculated numerically using the trapezoid rule. The incremental drag was then given as:

$$\Delta D' = \left[\sqrt{q_\infty - \left(P_{0,\infty} - P_{0,w_i}\right)}\left(\sqrt{q_\infty} - \sqrt{q_\infty - \left(P_{0,\infty} - P_{0,w_i}\right)}\right) + \sqrt{q_\infty - \left(P_{0,\infty} - P_{0,w_{i-1}}\right)}\left(\sqrt{q_\infty} - \sqrt{q_\infty - \left(P_{0,\infty} - P_{0,w_{i-1}}\right)}\right)\right]\left(y_i - y_{i-1}\right) \tag{2.37}$$

where the subscript, i, refers to the specific pressure probe at location, y_i. With K probes in the wake, the incremental drag can be summed across the wake to find the total drag (Eq. 2.38) and finally the drag coefficient using Eq. 2.39 below.

$$D' = \sum_{i=1}^{K} \Delta D' \tag{2.38}$$

$$C_d = \frac{D'}{q_\infty c} \tag{2.39}$$

2.1.8 Wind Tunnel Corrections

Due to the presence of the wind-tunnel walls, the flowfield is different than what is seen in atmospheric flight (free air). Therefore, corrections are made to the data to produce free-air results. Barlow, Rae and Pope[14] document methods to correct for the most significant effects due to solid blockage, wake blockage and reduced streamline curvature and these were implemented in this experiment.

Solid blockage is the reduction in effective area in the wind-tunnel test section due to the presence of the model. The blockage becomes significant when the model is at high angles of attack and maintaining conservation of mass through the test section forces the velocity to increase. This incremental increase in velocity is given as $\varepsilon_{sb,}$ below in Eq. 2.40, from Barlow,

Rae and Pope[14] and is a function of the airfoil thickness, *t*; thickness distribution, model angle of attack and model size.

$$\varepsilon_{sb} = \frac{K_1(model\ volume)}{C^{3/2}} \tag{2.40}$$

The coefficient K_1 was found to be 0.52 for a model completely spanning the test section height from Barlow, Rae and Pope.[14] The test section area is given as *C*.

The second factor, wake blockage, is another effect due to the conservation of mass in the wind tunnel. Since the velocity inside of the wake is less than that of freestream, the flow velocity around the wake must increase to conserve the mass flow rate. To correct for wake blockage, the velocity increment can be obtained from the following equation:

$$\varepsilon_{wb} = \frac{1}{2}\frac{c}{h}C_{d,u} \tag{2.41}$$

where *c* is the airfoil chord, *t* is the test-section height and $C_{d,u}$ is the uncorrected drag coefficient. Adding the two velocity increments due to solid and wake blockage provides the total velocity increment, ε.

The last effect, reduced streamline curvature, is the alteration of the natural streamlines by the wind-tunnel walls. This leads to increased lift and pitching moment about the quarter-chord because of an effective increase of camber. The correction factor is obtained as follows:

$$\sigma = \frac{\pi^2}{48}\frac{c}{h^2} \tag{2.42}$$

The correction factors acquired through Eqs. 2.40 – 2.42 were used to correct the aerodynamic coefficients: lift, drag and pitching moment; as well as the airfoil angle of attack. Additionally, both the pressure and moment data was corrected using these factors. The equations for applying the corrections to the aerodynamic coefficients are given in Eqs. 2.43 – 2.46.

$$\propto_{cor} = \propto_u + \frac{57.3\sigma}{2\pi}\left(C_{l,u} + 4C_{m,u}\right) \tag{2.43}$$

$$C_{l,cor} = C_{l,u}(1 - \sigma - 2\varepsilon) \tag{2.44}$$

$$C_{d,cor} = C_{d,u}(1 - 3\varepsilon_{sb} - 2\varepsilon_{wb}) \tag{2.45}$$

$$C_{m,cor} = C_{m,u}(1 - 2\varepsilon) + \frac{1}{4}\sigma C_{l,u} \tag{2.46}$$

2.2 Flow Visualization

To better understand the flowfield and how it is affected by the presence of two control surfaces, surface fluorescent-oil flow visualization was utilized. The objective was first to examine the flowfield on the NACA 3415 with several small flap and tab deflections and several angles of attack for comparison purposes followed by diagnosis of unexpected behavior seen in measured data. This type of flow visualization produces a time-averaged image of the surface flowfield and can reveal laminar, turbulent or transition regions in addition to separation or attached flow.

The technique of using surface oil visualization was taken from Ansell[9] and Busch[15] and begins with the application of black contact paper to protect the model and prevent clogging the pressure taps. The application of the contact paper was done with care to avoid creating air bubbles which would affect the flow. Once applied, two strips of yellow electrical tape were placed chordwise on the model, one approximately 6 inches from the ceiling and one 6 inches from the floor, and marked every 5% *x/c* for identification of flowfield feature location.

A layer of 10W-30 motor oil was applied to the contact paper surface. This was to smooth out any gaps or flaws in the paper and to allow consistent movement of the fluorescent oil. The fluorescent oil was a two-part composition of mineral oil and Kent-Moore 28431-1 fluorescent dye. An airbrush supplied with nitrogen at 30 psi was used to spray the model with the fluorescent oil. This method of application provided for a consistent layer of finer oil particles instead of larger particles that would be susceptible to movement due to gravity. A black light was used to ensure sufficient application of the oil.

The wind tunnel would then be run at the desired speed for approximately 2 minutes, after which the tunnel and lab lights would be shut off for the capturing of the flow-visualization images. The setup for the photography included two black lights that were placed ahead and behind the model within the test section. The locations were determined to be optimum for the least glare. The black lights caused the oil to fluoresce green which could then be captured by a Nikon D3100 digital SLR camera. Photographs were taken at two different locations: one for the overall flowfield on the entire model and one to detail the flowfield on the control surfaces as well as several different exposure times. These photographs were then loaded into the computer to guarantee the images captured the flowfield appropriately. The model would then be cleaned with rubbing alcohol and paper towels and the process of application and capturing would repeat for the next case in the flow visualization test matrix. The model setup with black light placement is shown in Fig. 2.10 below.

2.3 Test Matrix

As mentioned, the experiment was comprised of two sets of tests: the baseline case and tabbed case. The baseline cases included flap deflections of 0, ±5, ±10, ±20 and ±30 deg. The tabbed cases incorporated each of the flap deflections for the baseline case and tab deflections of 0, ±15, ±30, ±45 and ±60 deg. as well as additional deflections for each flap deflection in the region of zero flap hinge moment. All of the data for both cases were taken at a chord Reynolds number of 1.8 million and Mach number of 0.18. Additional runs were taken for model validation, hysteresis analysis and with the boundary-layer tripped. Some additional runs were taken at a lower *Re* of 1 million.

2.4 Figures

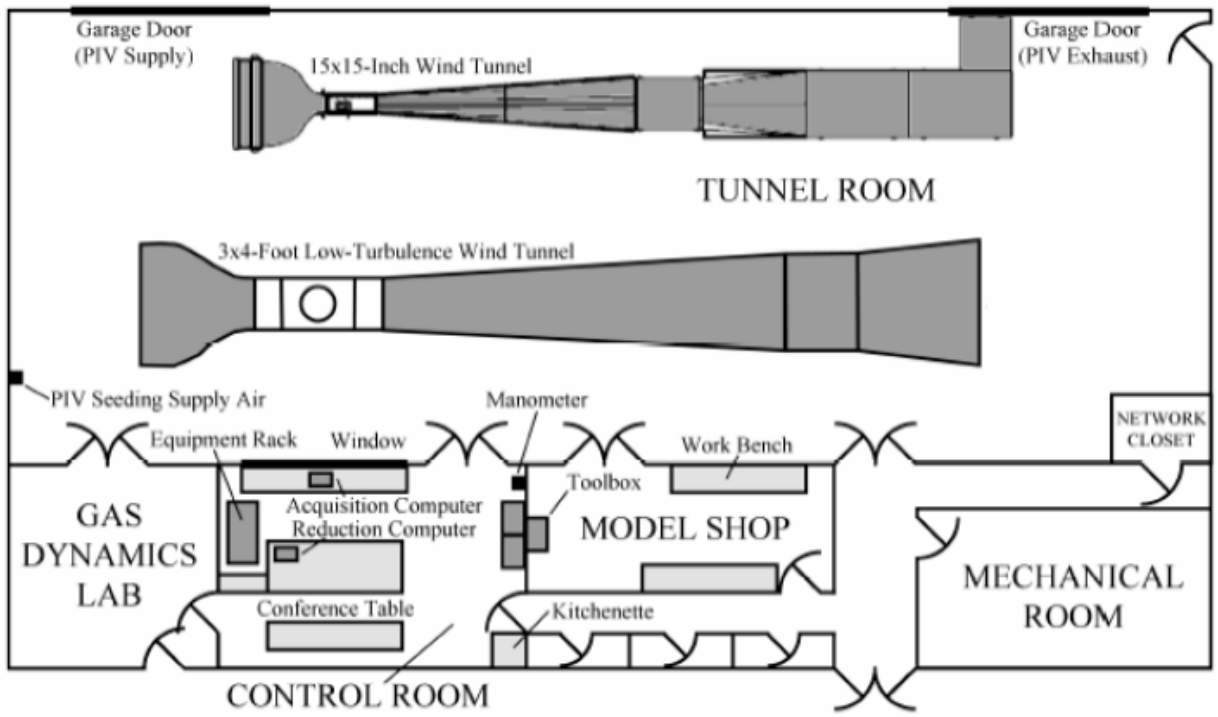

Fig. 2.1 Layout of Aerodynamics Research Laboratory at the University of Illinois (not to scale), after Jacobs.[16]

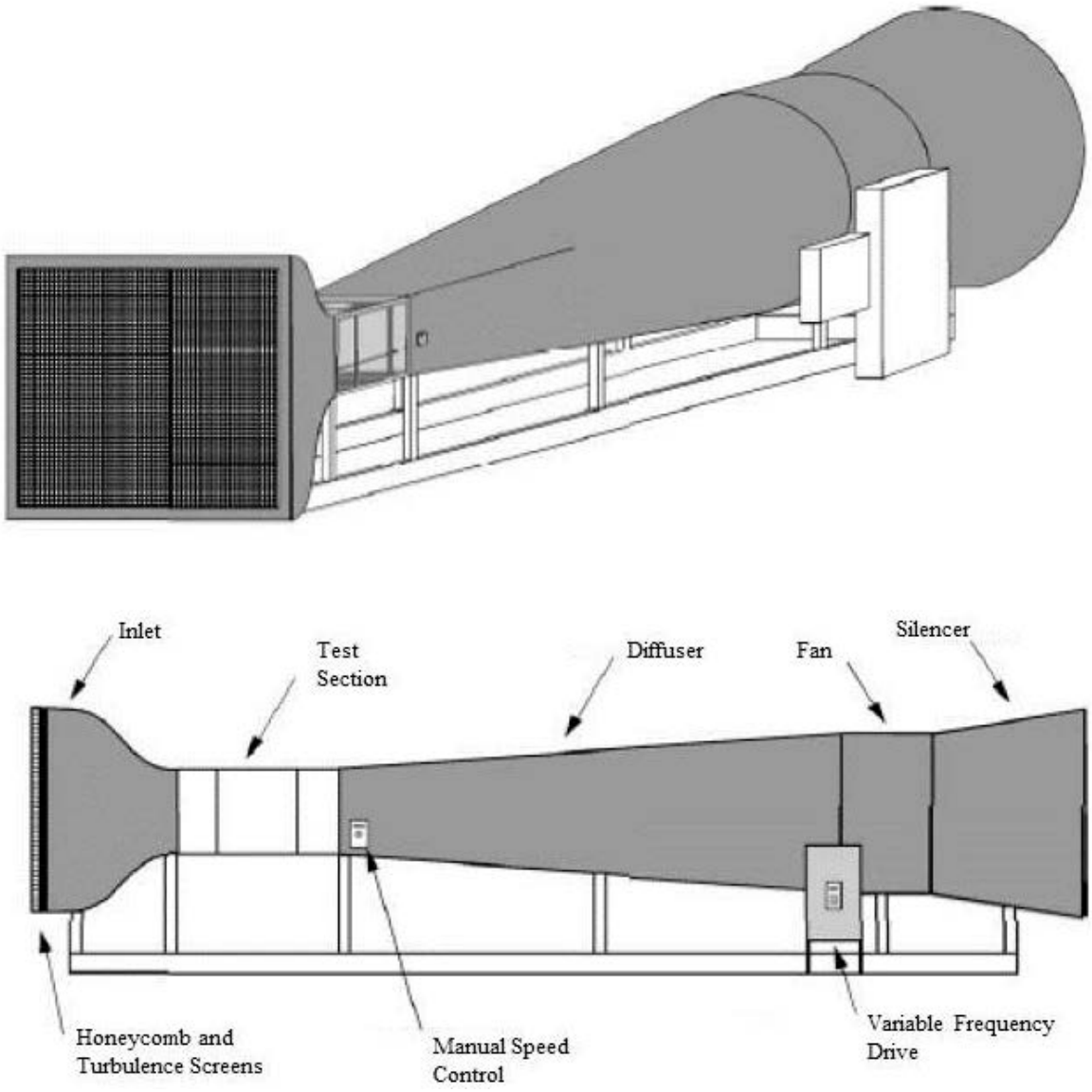

Fig. 2.2 Subsonic, Low-Turbulence 3 x 4 ft. wind tunnel, after Lee.[13]

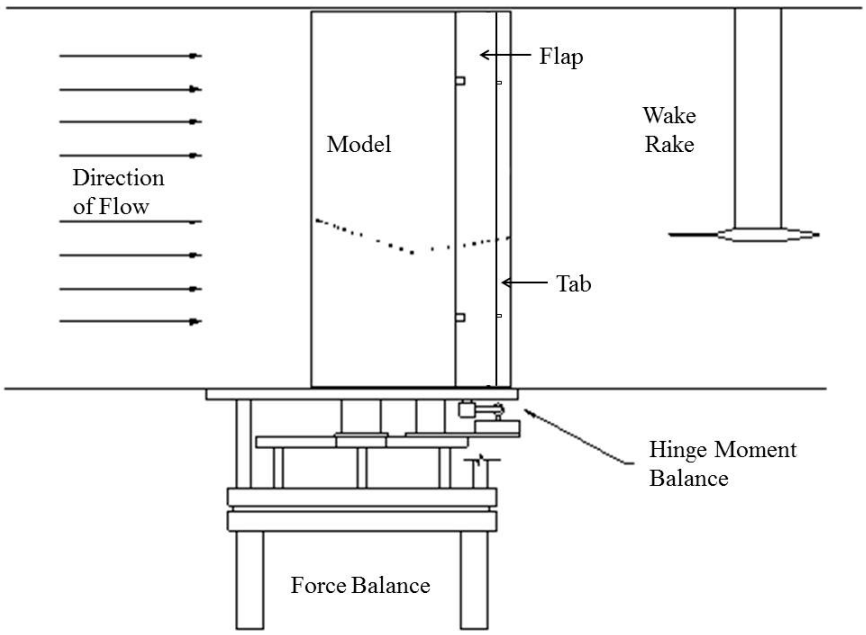

Fig. 2.3 Schematic of experimental setup, adapted from Lee.[13]

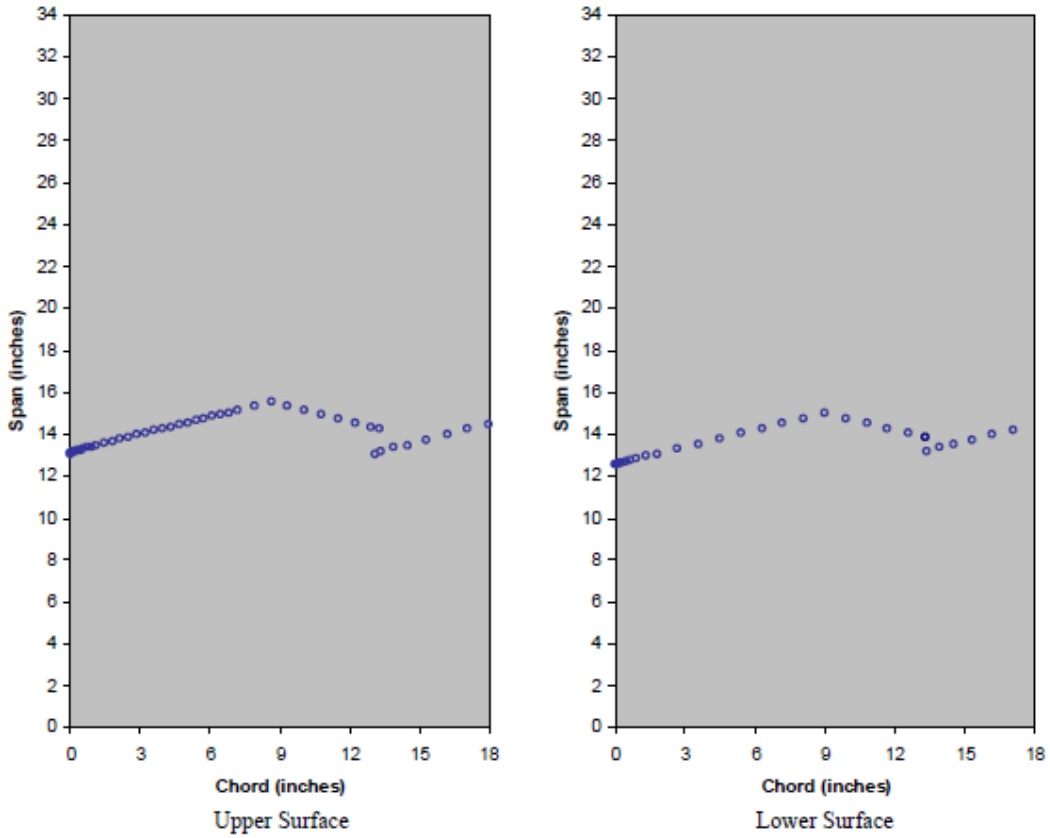

Fig. 2.4 Locations of pressure taps on both surfaces, adapted from Ansell.[9]

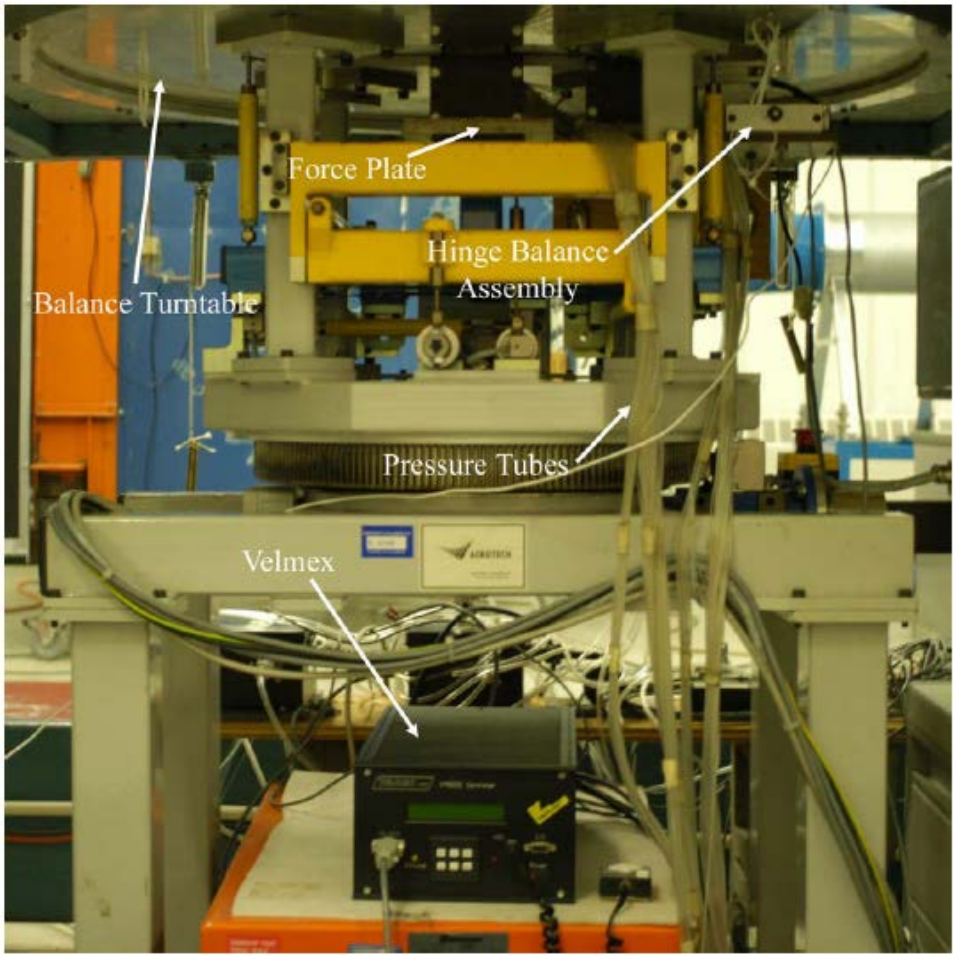

Fig. 2.5 Three-component force and moment balance, from Ansell.[9]

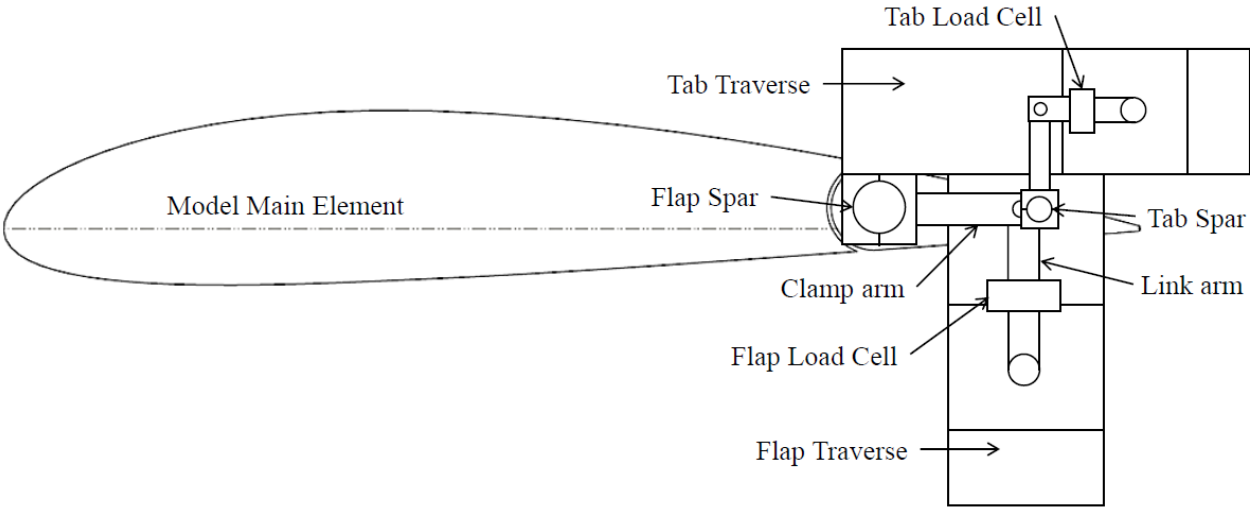

Fig. 2.6 Schematic of flap and tab hinge balance assembly.

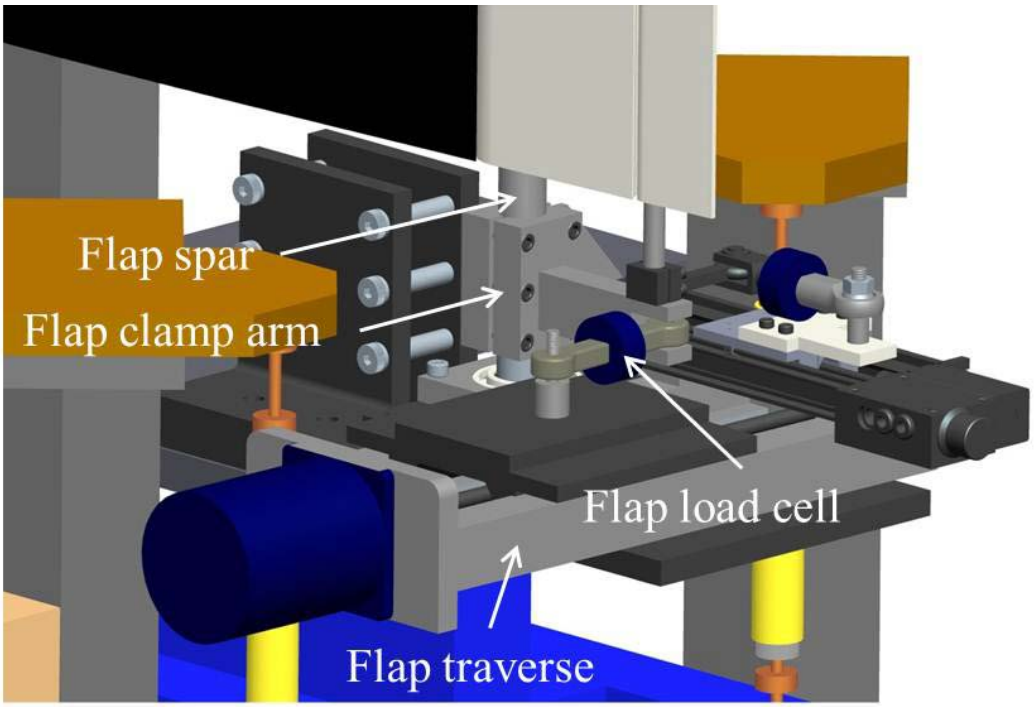

Fig. 2.7 3D model view of flap hinge balance assembly below wind-tunnel test section.

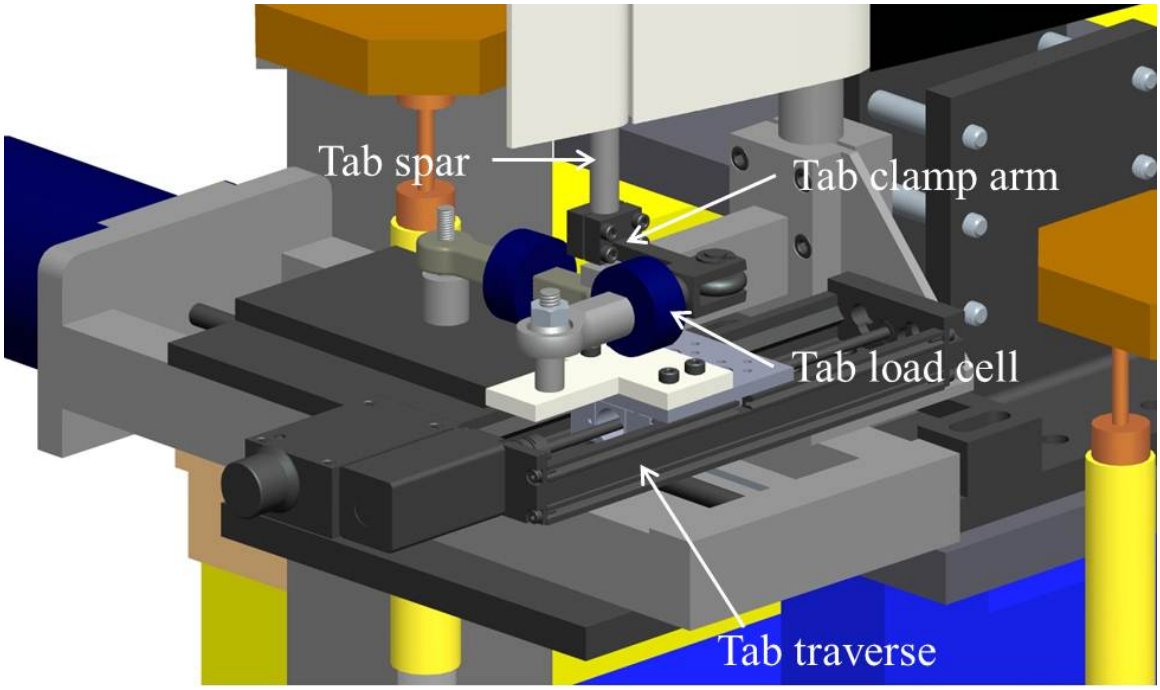

Fig. 2.8 Three-dimensional model view of tab hinge balance assembly.

Fig. 2.9 Wake rake and NACA 3415 model installed in test section.

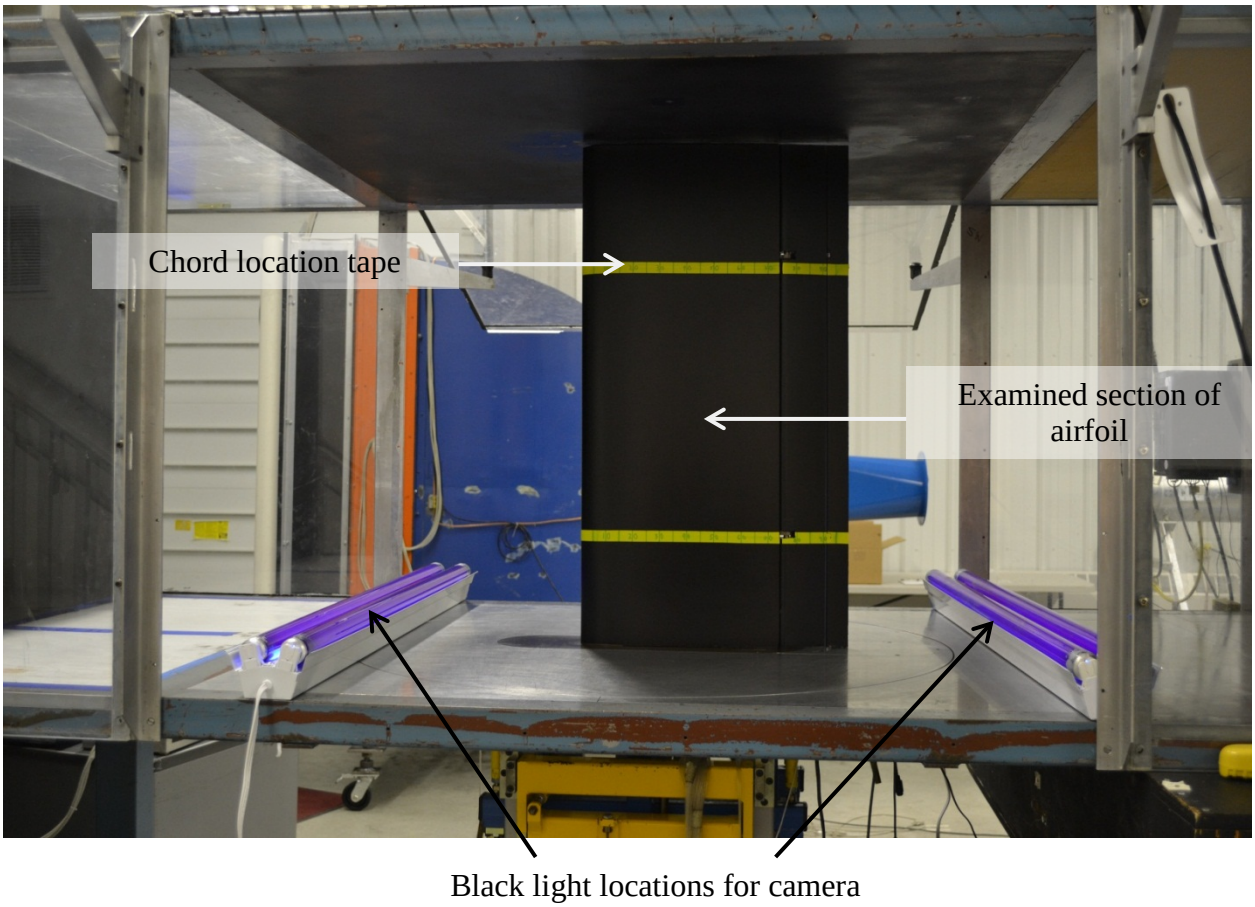

Fig. 2.10 Flow visualization setup in test section.

Chapter 3

Results and Discussion

This section will present the results from the experimental study and an analysis of the tab effectiveness in reducing hinge moments and the penalties of such a system. First, the data from the model with the new flap system were validated against previous experiments and issues with hysteresis in angle of attack and flap deflection was analyzed. Data will then be presented for the baseline and tabbed cases to provide insight into the general effect of the tab on the NACA 3415 and simple comparison of the hinge moments for both cases.

A more in depth study into the performance tradeoffs, with respect to drag and loss of flap effectiveness, was completed and is followed by a dynamic analysis to examine the potential work savings in a simulated deflection scenario. Lastly, flap and tab deflection cases that produced unexpected results were further studied with the assistance of pressure distributions and flow visualization.

3.1 NACA 3415 Model Validation

It was especially important in this experiment to validate the model setup with previous NACA 3415 experiments due to the redesigned flap and tab system. None of the previous experiments were done with a distinct tab so the data were expected to vary slightly. Additionally, the slot between the flap and tab allows air to flow as a result of the pressure gradient between the upper and lower surfaces which results in a slight difference in the data. To alleviate this problem, the tab gap was sealed with tape to simulate one control surface. Therefore, an experiment by Ansell[9] could be used for comparison. Data were taken at flap deflections of -10, 0 and 10 deg. and compared to the data from Ansell.[9] These data are shown in Fig. 3.1.

When analyzing the data, an offset was apparent in the linear range of the lift, pitching moment and hinge moment data. In addition, $C_{l,max}$ for this experiment was low and occurred at a lower angle of attack than the previous experiment. The flap of the previous experiment by Ansell[9] was reinstalled to help diagnose the issue and confirmed there was an issue with the new system as it produced the same results as Ansell.[9] After further examination of the data and the flap and tab structure, it was determined that the deflection angle of the new flap was being reduced as a result of the aerodynamic load. Therefore, the flap was being unloaded slightly thus reducing the lift and hinge moment. To fix this, a stiffener structural element was designed to stiffen the flap spar to prevent lateral movement of the spar which limited the overall movement of the flap system. Data were again taken for the same flap deflections and is also shown in Fig. 3.1. The offset in the lift and pitching moment data became much smaller with the addition of the stiffener and there was a significant improvement in $C_{l,max}$ and in the hinge moment data. Therefore, the slight difference in the lift and pitching moment data was accepted as inherent to the new setup.

3.2 Hysteresis Analysis

An additional study was completed to examine potential hysteresis effects with the NACA 3415 airfoil with varying angle of attack and flap deflection. It was important to discover the presence of hysteresis, if it existed, so measures could be taken to prevent its influence on the data especially in the case of flap deflection hysteresis which would be difficult to notice during the experiment.

3.2.1 Angle of Attack

To analyze hysteresis in angle of attack, the angle of attack was increased until approximately two degrees past stall and then decreased until the lift again matched that in the linear range. This was done for flap deflections of 0, ±10, ±20 and ±30 deg. The results are shown in Fig. 3.2 for lift, pitching moment and flap hinge moment. No hysteresis was seen in the lift data while the pitching and hinge moment data only differed slightly.

3.2.2 Flap Deflection

The hysteresis in flap deflection was completed by starting the wind-tunnel run at 0 deg. flap deflection then increasing δ_f to the maximum positive deflection of 30 deg. followed by decreasing δ_f to the maximum negative deflection of -30 deg. and then back to 0 deg. Three different angles of attack were chosen for this study. It was necessary to look at a large enough positive and negative angle of attack where at the lower flap deflections the flow would be attached and would proceed to separate for larger δ_f. Therefore, the angles of attack selected were -11, 0 and 13 deg. The lift and hinge moment were the focus and are shown below in Fig. 3.3. The data show a slight discrepancy in the hinge moment data while the lift data were almost identical for both flap deflection directions. It was thought that the small amount of friction in the system was to blame for the differences. Since the experiment only used static deflections where the flap would be set at a single deflection for the entire run, there was no need to attempt to fix the problem, but measures were taken to properly zero the load cell. Simply moving the flap back and forth once the deflection was reached eliminated the residual friction in the system.

3.3 Baseline Case

In order to understand the benefit of the addition of a tab, data were taken for a baseline case where the effect of a flap alone was analyzed. The tab was left at 0 deg. deflection and only the flap hinge moment was evaluated. The entire flap deflection in the test matrix was included. The results for lift, drag, pitching moment and flap hinge moment are shown in Fig. 3.4.

In Fig. 3.4, typical flapped-airfoil behavior was seen where the lift curves for all flap deflections remain relatively constant while the angle of attack for maximum lift coefficient decreases for increasing flap angle. The stall becomes sharper for positive deflections while becoming flatter for larger negative deflections suggesting changes in stalling process.

The hinge moment coefficient data for the flap also exhibits classic behavior but with a slight non-linearity in the slope for 0 and ± 5 deg. flap angles. The non-linearity in the slope for the -5 deg. flap deflection was studied further to diagnose the cause and is presented later in Section 3.5. Positive flap deflections had larger hinge moments than negative deflections but the change in hinge moment seems to be consistent with angle of attack for both negative and

positive deflections. In addition, the smaller deflections experienced a sharper drop in hinge moment due to stall.

The drag coefficient data illustrate the large increase in drag with large flap deflections as well as the difference in drag between positive and negative flap angles of the same magnitude. Positive deflections produced significantly more drag for a given angle of attack which was expected for an airfoil with positive camber. Each flap deflection produces approximately constant drag throughout the entire angle of attack range up until approaching stall with the exception of slight decreases in the data for ±30 deg. deflection. These decreases occur at angles of attack right before stall and will be examined further later in the results and discussion section.

The data for pitching moment was consistent with expected trends, the exception being the decreased slope for larger negative deflections, especially the -30 deg. case. For the -30 deg. flap deflection, non-linear behavior with almost constant C_m near and after stall was observed and is similar to the behavior in the hinge moment data for larger deflections.

3.4 Baseline Case with Boundary-Layer Trip

Before the tabbed cases were investigated, the baseline cases were run again with a boundary-layer trip strip. This would provide a dataset for a more accurate comparison with computational fluid dynamic results that are limited in predicting the location of transition. The trip strip used was a section of double-sided tape extended on the model from floor to ceiling covered with a low concentration of 40-grit roughness elements. The front edge of the strip was located at x/c = 0.02 on the upper surface and x/c = 0.05 on the lower surface. This was run for flap deflections of 0, ±10, ±20 and ±30 deg. The lift, drag, pitching moment and flap hinge moment data for 0, ±10 and ±30 deg. flap deflections are given along with the clean data for comparison in Fig. 3.5.

The most obvious effect was the reduction of $C_{l,max}$ and stall angle of attack as is expected with forced transition and is evident for all of the data shown in Fig. 3.5. There was a slight offset in the linear region of the lift curve for the 0 deg. flap deflection and entire range of angle of attack. An offset between the clean and tripped data was evident in the hinge moment and pitching moment data as well, especially for the 30 deg. flap deflection. While it is partially

due to the boundary-layer trip, it was most likely a result of the stiffener piece being added after the tripped case data were taken.

The drag data shows trends expected for boundary-layer trips. The tripped data had slightly higher drag for the entire angle of attack range and the behavior of the drag curves was similar between the two cases.

3.5 Tabbed Case

Following the fixed-tab cases, the tab was actuated for each of the flap deflections and surface pressure, lift, drag, hinge moment and pitching moment data were taken. The consequences of using a tab to hold or move a flap could then be determined. In this section data are for select cases of 0 and ±10 degrees flap deflection. The data for the other flap deflections of ±5 and ±20 deg. are shown in Appendix C. The 0 deg. case demonstrates the general effect of a tab on the NACA 3415 airfoil while the ±10 deg. cases show these effects as well as the capabilities of the tab in assistance of the flap under a non-zero flap setting. The data for lift and drag as well as flap and tab hinge moment for a flap deflection of 0 deg. are shown in Fig. 3.6.

From the data presented in Fig. 3.6, it can be seen that a 25%-flap chord simple tab has a large effect on the performance of the NACA 3415 airfoil. A 60 deg. tab deflection increased $C_{l,max}$ by 51% while only a -15 deg. tab deflection reduced it by 16%. The larger negative tab deflections show a loss of effectiveness and fail to further reduce $C_{l,max}$. The drag data also indicate a large effect with both the positive and negative 30 deg. deflections producing four times the drag over the linear range of angle of attack. There is a slight decrease in drag for higher angles of attack for the -30 deg. tab deflection.

This case also displayed different trends for the hinge moment data of both control surfaces compared to the other tab deflections. This occurs during the same range of angle of attack as the decrease in drag. Over this range, the slope of the tab hinge moment curve is more negative than the previous -15 deg. deflection and actually becomes positive post-stall. The other cases exhibit a drop in post-stall hinge moment. As for hinge moment coefficient magnitudes, both the positive and negative 60 deg. tab deflection produced a ΔC_h, change in hinge moment referenced from 0 deg. control surface deflection, of 0.29 and 0.31, respectively, in the flap hinge moment coefficient at zero angle of attack. This magnitude is significantly

reduced for larger angles of attack for the large negative tab deflections but is maintained for each of the positive tab deflections. The tab hinge moment coefficients resemble the flap data with the exception of the larger positive tab deflections, which resulted in higher ΔC_h than for the flap. For both the flap and tab, ΔC_h decreased for tab deflections larger than 30 deg. This is due to the separation that occurs over the tab for the entire range of angle of attack.

With the data presented for 0 degree flap deflection to show the effect of the tab on the NACA 3415 performance, data will now be shown for ±10 deg. flap deflections to demonstrate the tab effect under non-zero flap deflections. An additional tab deflection of 5 deg. was included for δ_f = -10 deg. to provide another tab deflection that produced a flap hinge moment around zero. Displayed in Fig. 3.7 are the results for δ_f = -10 deg.

As shown in the data for a -10 deg. flap deflection, the tab continues to have a significant effect on the airfoil performance but several differences can be seen compared to the 0 deg. flap deflection case. Starting with the lift data, there is even less symmetry about the fixed (δ_t = 0 deg.) tab data. Even though this is expected since the airfoil has positive camber, the lift curve slope behavior changes when the tab is deflected in either direction. Additionally, each of the negative tab deflections, while offsetting the lift curve as expected, does not significantly influence the magnitude of $C_{l,max}$.

Changes in behavior can also be seen in the hinge moment data for both the tab and the flap, especially for the tab hinge moment coefficient data. For the negative tab deflections as well as δ_t = 0 and 5 deg., the slope and post-stall behavior are similar while the tab deflections larger than 5 deg. exhibit a drastic change in slope at around 2 deg. angle of attack then flatten out at 10 deg. angle of attack. This change in behavior will be studied further through flow visualization later in the results and discussion section.

The flap hinge moment data show the same behavior for the same two positive tab deflections but is not as pronounced as in the tab data. The tab is less effective for lower angles of attack when positively deflected, while the negative deflections are the most effective in this range. This result is reversed for the larger angles of attack near stall as well as post stall. It is also interesting to note that little tab deflection is required to hold the flap at -10 deg. since the flap hinge moment remains near zero for the entire range of angle of attack before stall. Furthermore, the hinge moment required to hold this deflection is also near zero since the tab

hinge moment is almost zero. A 5 deg. tab deflection was tested to produce this effect but actually induces a slight negative flap hinge moment for all angles of attack.

Lastly, the drag data results were as expected with the larger deflections having similar effect as seen for 0 deg. flap deflection. A quick rise and fall in the drag data or the 30 and 45 deg. tab deflections for angles of attack in the 2 to 6 deg. range was seen while the other tab deflections show the expected behavior.

To demonstrate the effect of a tab for a positive flap deflection, data are shown below in Fig. 3.8 for 10 deg. For this flap deflection, an additional tab deflection of -10 deg. was run to provide additional data in the region of flap $C_h = 0$.

Beginning with the lift data, negative tab deflections larger than -15 deg. produce no significant change in $C_{l,max}$ with the -45 deg. deflection with only a small $\Delta C_{l,max}$. Also, there was a loss of effectiveness for these tab deflections at lower angles of attack. In contrast, a 45 deg. tab deflection increases $C_{l,max}$ by 25% over the $\delta_t = 0$ deg. case while the 60 deg. tab deflection did not further increase $C_{l,max}$. The stall angle of attack remains constant for all tab deflections tested. The drag data, while non-linear, shows the same trend for each negative tab deflection. This trend of decreasing drag with increasing angle of attack begins at roughly the same α (roughly 2 deg.) for each of the deflections with the magnitude of reduction varying. The positive deflections, with exception to the 60 deg. tab deflection, show increased drag with increasing angle of attack until a very rapid rise at stall.

As was seen with the -10 deg. flap deflection case, the tab hinge moment data for the 10 deg. deflection reveals a sharp change in behavior between different tab deflections. Here the larger negative tab deflections (-30, -45 and -60 deg.) display non-linear performance with increasing angle of attack as well as a positive increase in hinge moment post-stall for $\delta_t = -30$ deg. which was not seen for the other tab deflections. This same behavior was seen on both the flap and the tab while the other tab deflections all show expected trends. Again, the separated flowfield seen on flap and tab deflections of the opposite sign is the cause of the non-linear behavior. Additional analysis of this phenomenon is given later.

Analyzing the flap hinge moment data, the -15 deg. tab deflection is the most effective at producing a zero flap hinge moment for most angles of attack. Interpolating between the curves for -15 deg. and -10 deg., assuming linear behavior between curves, the exact deflection for holding the flap deflection could be found. The penalty in tab hinge moment for flap assistance

is actually small since a small positive hinge moment is seen for lower angles of attack until around α = 6 deg. then is near zero until stall. Further analysis will be provided later in the results and discussion section and will also account for lift and drag.

3.6 Computational Data Comparison

The results of the computational investigation performed by Winkler, and reported in Bottalla et al.,[1] will be compared to the experimental data using the tripped boundary-layer data when available. The primary metrics of concern are the lift and drag coefficients, as well as the flap hinge moment. The flap hinge moment will be related to the power required to actuate the control surface, and this will be used as an initial screening of the powered tab concept.

In Fig. 3.9, the lift, drag, and hinge moments are compared to the tripped experimental data, respectively, for the δ_f = 0, ±10, and ±30 deg. and δ_t = 0 deg. configuration. For δ_f = 0 deg. and δt = 0 deg. there is excellent agreement up until stall (~14 deg.), where the CFD is seen to break much more gradually than the experiment. This is typical for steady-state CFD at high angle of attack. In particular, the lift is seen to be over-predicted after stall and the drag under-predicted. However, CFD is capturing both the magnitude and trends of the forces and moments as the angle of attack is varied, giving confidence in the ability of CFD to predict increments when the powered tab is simulated later in this work.

The same comments can be made at higher flap deflections, such as the δ_f = 10 and δ_t = 0 deg. configuration shown in Fig. 3.9. Agreement between CFD and experiment is seen to be excellent up until 13 deg. It can be argued that the steady-state assumption is no longer valid at high angle of attack when the flow is massively separated. Regardless, the trends are predicted and there is generally good agreement between the CFD and experiment.

At δ_f = 30 deg., δ_t = 0 deg., the flow is becoming highly unsteady as can be seen in the CFD data.[1] There is large scale separation in these greater flap deflections which is not properly modeled in a steady-state simulation, and not surprisingly, the comparison between CFD and experiment degrades at higher flap deflections.

Negative flap deflections are also of interest, and were simulated in both CFD and experiment. The comparison for δ_f = -10 and δ_t = 0 deg. is also shown in Fig. 3.9. Excellent overall agreement is seen. As in the positive flap deflections, we see the CFD break more gently

at stall than experiment. As the negative flap deflection increases to -30 deg. with δ_t = 0 deg. we see the CFD data begin to deviate from the test data. In fact, the CFD is not showing any break in the lift at high angle of attack for this configuration, whereas the experiment indicates a stall around 15 deg.

Tab deflections are of primary importance to this study. Up to this point, we have only compared zero tab deflections to experimental data, and have seen good agreement between CFD and test except where the flow is known to be separated. Note the experimental data are not tripped in these configurations. Therefore, it is expected that there will be laminar to turbulent transition effects which will not be captured in the fully-turbulent CFD. The flap and tab combinations examined were (δ_f = -10 deg., δ_t = 30 deg.), (δ_f = 0 deg., δ_t = -5 deg.), and (δ_f = 10 deg., δ_t = -30 deg.) and are shown below in Fig. 3.10. The δ_f = -30 deg. and δ_t = -30 deg. case will also be shown later.

In Fig. 3.10, the CFD and experimental data are compared for the δ_f = 0 and δ_t = -5 deg. case. Excellent agreement is seen, as has been typical for small deflections. The CFD is seen to break more gently at stall than experimental data, but the stall seems to occur at the same angle of attack in both CFD and test. Continued good agreement in lift with larger deviations in C_d and C_h are seen for the more challenging configuration of δ_f = 10 and δ_t = -30 deg. The same statements can be made about this configuration as the prior configuration. The δ_f = -10, δ_t = 30 deg. configuration was examined next. The agreement is good, with the CFD slightly over-predicting the lift. Note the inflection point in the hinge moment near α = 15 deg. is correctly captured in the CFD.

The next case considered is probably the most challenging with the δ_f = -30 and δ_t = -30 deg. configuration. The lift, drag, and hinge moments can be seen below in Fig. 3.11. The steady-state CFD is seen to over-predict the lift as well as miss the “drag bucket” phenomena seen in the experimental data between 5 and 15 deg. angle of attack. The hinge moment is seen to have the correct trends, but a lesser moment is seen in the CFD than test. At this condition, the CFD does not capture the stall seen in the experiment. With the understanding that some of these differences can probably be attributed to transition, as seen with flow visualization, the other differences are due to the unsteady nature of the flow.

Knowing that the steady-state CFD would likely not compare well on configurations which have large flap/tab deflections and therefore, separated flow, unsteady CFD was planned

as part of this work for select cases. DDES with a low dissipation scheme was chosen by Winkler[1] to run the δ_f = -30 deg., δ_t = -30 deg. case at α = 0 and 10 deg.

The unsteady results for lift are also shown in Fig. 3.11 for lift and drag. Note the improvement in lift when the simulation is run in a time-accurate fashion. The lift predicted by the unsteady CFD closely matches the test data. It is therefore reasonable to assume many of the other configurations where the CFD was slightly high in lift could have been improved by running time-accurate.

The drag behavior of this configuration is most interesting. A drag bucket is seen between α = 5 and 15 deg. in the experimental data. The steady-state CFD did not predict this trend. However, the unsteady CFD did show a decrease in drag from 0 to 10 deg. angle of attack. Without more unsteady CFD data, it is not possible to discern a "bucket" profile. Flow visualization was required to fully understand this phenomenon, and the results show that it appears to be due to laminarization of the lower surface, which the CFD is unable to model due to the fully-turbulent assumption.

3.7 Further Analysis

The data from the tabbed cases were compared to the data from the baseline case to assess the power savings of a tab-assisted flap. To begin, since the tests were solely static in nature, measuring data for a fixed tab and flap deflection for an angle of attack range, only changes in lift, drag and hinge moment could be calculated directly. The results of these calculations will be tabulated in Section 3.7.1. The effect on lift will then be analyzed further using flow visualization in addition to the force, moment and pressure data. Also, a dynamic analysis looking at the work savings for a simulated flap and tab deflection scenario will be presented. Lastly, additional studies were done into the cause of unexpected trends seen in the data for both the baseline and tabbed cases. Flow visualization and pressure distributions are presented as part of this analysis.

3.7.1 Tab Performance

As stated, the data from both the baseline and tabbed cases were compared to find the effect on hinge moment, drag and lift in a simple static scenario. For the hinge moment calculations, the hinge moment coefficient was used along with geometry to calculate the

dimensional hinge moment in order to make a direct comparison between the flap and tab. To calculate the tab deflection for trim, linear interpolation was used between tab deflection curves, which was deemed reasonable for tab deflections between ±30 degrees. The results of these calculations for flap deflections of -10 and 10 deg. and the respective tab deflection for "trim" are presented below in Table 3.1. The calculated reductions/increases in hinge moment, lift and drag are relative to the "untrimmed" case. The results for all of the remaining flap deflections are shown in Appendix D.

Table 3.1 Effect of using tab on flap hinge moment, drag and lift.

δ_f *(deg.)*	α *(deg.)*	$\delta_{t,trim}$ *(deg.)*	*% Reduction in Hinge Moment*	*% Drag Change*	*% Lift Change*
-10	-4	4.24	97.15	3.31	1.66
	-2	3.40	96.61	3.8	5.56
	0	2.49	96.14	2.17	13.76
	2	1.49	94.17	1.59	15.57
	4	0.84	81.4	1.85	3.96
	6	0.73	76.77	1.8	3.23
10	-4	-12.33	97.88	-3.33	-62.82
	-2	-12.73	98.48	9.81	-39.44
	0	-12.93	99.06	13.06	-29.50
	2	-13.44	99.42	7.86	-25.35
	4	-13.74	99.61	11.76	-22.39
	6	-14.23	99.74	15.3	-18.17

The results for the ± 10 deg. cases show the significant effect the tab has in reducing the hinge moment for holding a flap deflection. For all but two cases above, the hinge moment reduction is above 95% of the untrimmed value even though the tab deflections are ranging from -10 to -15 degrees for the 10 deg. flap deflection. The tab deflections required for trim for the -10 deg. flap deflection are quite low ranging from 1 to 4 deg. but holding these smaller tab deflections requires a larger hinge moment than that for the 10 deg. flap deflection. From the data shown in Fig. 3.8 above, it was seen that the tab deflection for trim reduced the hinge moment coefficient from -0.1 to zero and required very little hinge moment to hold this tab deflection. Thus, the hinge moment reduction was almost 100% for 10 deg. flap deflection. For

the -10 deg. flap deflection, the same was true for the tab hinge moment but the flap hinge moment was already near zero and therefore required only a few degrees with the tab. This resulted in slightly lower hinge moment reductions.

The consequence of these very high hinge moment reductions is the increase in drag and loss/increase in lift. Starting with the -10 deg. flap deflection, only a few degrees of tab deflection increase lift up to 16%, which is a loss of effectiveness for a negative deflection. As expected, the drag is only slightly increased by the tab deflection. The effects are magnified for the 10 deg. flap deflection since it requires larger tab deflections for trim. For the angles of attack above zero, the lift is reduced from 18 to 30%. The reasoning for the larger reductions for angles of attack below zero is the fact that the lift is near zero resulting in a high relative change in lift. The drag increase is larger in this case as well even though one case (α = -4 deg.) resulted in decreased drag.

While only a small sampling of data was presented in Table 3.1, the trends seen for the other flap deflections remain the same. For the positive flap deflections, the hinge moment reductions remain above 99% for most tab deflections. The complex flowfield existing for coupled positive/negative flap and tab deflections is most likely the cause of this large reduction. Separation occurred for flap deflections above 10 deg.; and, with each increase in flap deflection, was seen for larger angle of attack ranges. The same is observed with higher tab deflections and, when combined with large flap deflections, yields a completely separated flowfield over the tab. This flowfield induces a minimal hinge moment on the tab while effecting a large change in the flap hinge moment.

While this is effective for power savings, the consequences are again seen in the lift and drag. With increasing flap deflection and increasing required tab deflections, the drag increases greatly approaching 40% for the 30 deg. flap deflection case. In addition, the lift loss is consistently above 30% approaching 40%, ignoring angles of attack where C_l is small, for 30 deg. flap deflection. While the hinge moment reductions are slightly lower for the negative deflections, the lift and drag penalties are almost equivalent to that of the positive deflections. Since the change in the lift is substantial, a study was done using flow visualization as well as the C_p distributions to examine the cause. This study is discussed next.

3.7.2 Loss of Flap Effectiveness Study

In the previous section, the benefits of adding a tab to reduce hinge moments were summarized. In this case, there are two main disadvantages: an increase in drag and a large loss in flap effectiveness seen as a change in airfoil lift. The former being expected for a tabbed system and was documented in Table 3.1 while the latter seems to be dependent on the airfoil. During the time when the flap is being deflected with the assistance of the tab, a decrease in flap effectiveness would have to be accounted for by increasing the angle of attack. This leads to further increased drag and is undesirable.

Previous data revealed a trend of large tab influence on the flap effectiveness necessitating additional analysis. This influence was seen as large changes in lift when using the tab for "trim" and, in some cases, reversal of effectiveness apparent in both lift and hinge moment data. To look at the latter effect, data from the ±30 deg. flap deflection cases were examined further since this effect is intensified with increasing flap deflection. For the 30 deg. flap deflection case, flow visualization was performed on two different tab deflections to diagnose the cause the reversal in flap effectiveness and large loss of lift. Then looking solely at the influence on lift, the lift change was tabulated for each flap deflection and corresponding tab for "trim." The C_p distributions for the 10 deg. flap deflection are also shown in support.

The aerodynamic performance data for the -30 deg. flap deflection is shown in Fig. 3.12. The change in lift at higher angles of attack and $C_{l,max}$ for decreasing (more negative) tab angle decreases almost to the point where additional tab deflection produces no additional effect. This was more evident for increasing (more positive) tab angle where by a tab deflection of 45 deg. there was a reversal of effectiveness and actually begins to produce less lift than a tab deflection of 30 deg. Increasing to a deflection of 60 deg. continues the effect with additional lift loss even though $C_{l,max}$ increases. This loss of flap effectiveness was also evident in both the flap and tab hinge moments for both the larger tab deflections which implied the separation on the tab decreases the hinge moment on the tab and erases its effectiveness on the flap.

The 30 deg. flap deflection case displays a more apparent reversal of flap effectiveness. Figure 3.13 shows the lift and drag coefficient data along with the flap and tab hinge moment coefficients. The lift data shows evidence of this reversal where there is a reduction in lift for a tab deflection of -30 deg. The lift curves for δ_t = -45 and -60 deg. are almost equivalent to that of the -15 deg. tab deflection.

The data for flap hinge moment was as expected showing the same result as in the lift plot. The flap hinge moment data for the -45 and -60 deg. tab deflections almost replicate that of the -15 deg. tab deflection but have different behavior post-stall. That outcome in the tab hinge moment data is not as pronounced but occurs again past the same tab deflection of -30 deg. A slight reversal in flap effectiveness is not seen until δ_t = -60 deg.

Looking again at the tab effect on flap hinge moment, a zero flap hinge moment was accomplished by a tab deflection of approximately -30 deg. As shown, tab deflections of 45 and 60 deg. produce an adverse effect, thus making these deflections ineffective. The penalty in using this tab deflection for flap trim was seen in the lift reduction which was on the order of 30%.

To explain the adverse effect of tab deflection to larger negative values from δ_t = -30 deg., flow visualization was employed. This technique provided insight into the flowfield around the airfoil and was performed at zero angle of attack for the tab at -30 and -45 deg. The results are shown below in Figs. 3.14 and 3.15. In each flow visualization image, flow is from the left to the right and the flowfield features are labeled in Fig. 3.14 and the flap and tab gaps are located at 75% and 92% respectively.

The features are characterized by the shear stress, which is responsible for the oil movement, produced by the flowfield on the surface. High shear regions, such as stagnation points and boundary-layer reattachment, cause the oil to be scrubbed off in the direction of the flow. Attached laminar and turbulent flow create streaks of oil oriented in the direction of the boundary-layer flow while separated flow, having low shear, causes the oil to remain in the initial sprayed pattern. Before a separated flow region the shear level goes to zero at the separation point creating a region of oil where there is no longer enough force to move the oil downstream.

These flow visualization images show that while the flow remains unchanged on the lower surface, separation begins to occur on the upper surface of the tab when deflected from -30 deg. to -45 deg. The separation is nonuniform on the surface with larger regions of attached flow, but is expected for such a large tab deflection. What is unexpected is the large effect this separation has on the lift and hinge moments for both surfaces, as seen in Fig. 3.13, as it cancels much of the effect of the tab deflection producing a lift curve and hinge moment equivalent to that of a 15 deg. tab deflection.

This loss of flap effectiveness, with respect to the lift, was not limited to the ±30 deg. flap deflections since each flap deflection exhibited this effect. For each flap deflection tested, the change in lift from the untrimmed to trimmed case was calculated at zero angle of attack. A tab deflection for trim for the 30 deg. flap deflection case could not be determined due to the reversal of flap effectiveness and lack of tab deflections run between 30 and 45 deg. Therefore, the closest tab deflection for trim was -30 deg. which produced a flap C_h of -0.026. Table 3.2 below contains the results of this study.

Table 3.2 Loss of flap effectiveness with use of tab for trim (at α = 0 deg.).

δ_f (deg.)	$\delta_{t,trim}$ (deg.)	C_l		% Reduction in $\lvert C_l \rvert$
		untrimmed	*trimmed*	
-30	27.92	-0.671	-0.405	39.6
-20	16.71	-0.429	-0.254	40.8
-10	2.49	-0.100	-0.086	13.7
-5	-1.22	0.012	-.00020	102.0
0	-4.06	0.186	0.133	28.5
5	-7.71	0.346	0.320	7.5
10	-12.93	0.542	0.382	29.5
20	-24.23	0.810	0.550	32.1
30	-30	0.977	0.663	32.1

For each flap deflection except for 5 deg., the effect on lift was substantial (14% to 102%) even though the 102% change for the -5 deg. flap deflection is due to the small amount of lift generated for this case. The larger flap deflections see the largest effect since large tab deflections are required for trim. Even smaller flap deflections with smaller tab deflections required for trim displayed a significant effect, such as the δ_f = 10 and δ_f = 0 cases. For the 10 deg. flap deflection, the C_p distribution for both the trimmed and untrimmed cases is shown below in Fig. 3.16. With the C_p distribution, the tab effect on the entire airfoil can be understood.

The C_p distribution shows that, when the tab was deflected, the surface pressures reflect the roughly 15% reduction in lift over the entire main element. Though the tab is small, it's effect on the airfoil is global creating a significantly lower suction peak and a consistent offset in

C_p across both the lower and upper surface. This is a significant effect for a tab deflection of only 12.5 deg.

3.7.3 Dynamic Analysis

Next, a simulated dynamic study was done since the static data and hinge moment reductions do not sufficiently represent the eventual application. As stated earlier, since dynamic movements of the tab and flap system were not implemented in this phase of testing, accurate dynamic hinge moments as well as a time schedule for the deflections are not available for power savings calculations. As an estimate of potential work savings, several hypothetical cases of flap deflection schedules could be analyzed using the static data and assuming linear behavior between flap and tab deflections. Again, this is a reasonable assumption for all but the larger ±45 and ±60 degree deflections. This analysis ignores the unsteady flowfield effects due to flap and tab motion.

One hypothetical case includes deflecting the flap from 0 deg. to 30 deg. and back to 0 deg. The opposite case in going to -30 deg. and back was also included. Three angles of attack (α = 0, 4 and 8 deg.) were analyzed and the tab was limited to ±30 deg. deflections. Once the desired deflection was reached, the tab would straighten out and additional work required to hold the deflection was ignored.

The baseline calculation was made with the flap hinge moment coefficient data for each of the deflections tested. From an integration of flap C_h vs. flap deflection for each angle of attack over the range of the desired deflection, a value could be obtained which, along with geometry and flow conditions, leads to the work done to complete the deflection. The data used for these calculations are shown below in Fig. 3.17. Flap hinge moments that aided flap movement were ignored and work was assumed to be zero for that segment.

For the tabbed case, since only 0 and ±30 tab deflections were allowed, a tab schedule was first determined for each desired flap movement. For example, a desired flap movement from 0 to 30 deg. would require a -30 deg. tab deflection until reaching 30 deg. in which the tab would be retracted to 0 deg. In order to find the work required for this movement, an integration of tab C_h vs. flap deflection under a tab deflection of -30 deg. would be calculated and, as before with the flap calculations, would be converted to work with the flow conditions and tab geometry. To effect movement of the flap back to 0 deg. a tab deflection of 30 deg. would then be required and the same process would be used to calculate work. Additionally, the work

required to deflect the tab from 0 to -30 deg. at δ_f = 0 deg. and then from -30 to 0 deg. at δ_f = 30 deg. as well as the required movements for returning the flap to 0 deg. is added. Again, assisting hinge moments would be ignored. The data used for the calculation of work for constant tab deflection vs. flap deflection is presented below in Fig. 3.18.

For both deflection scenarios, it was found that no work was required to return the flap to its original position at 0 deg. since the hinge moments were assisting. So the work savings calculations for obtaining the desired deflection represent the work savings for the entire scenario. The results of these calculations for the three angles of attack are listed below in Table 3.3, where the scenarios are denoted by the desired deflection in the table.

Table 3.3 Work savings for tab-assisted flap in percent.

	α (deg.)		
δ_f (deg.)	0	4	8
0 to 30	92.9	93.7	95.0
0 to -30	80.7	80.5	78.6

The resulting work savings, shown in Table 3.3 above, are quite large but were expected due to the large hinge moment reductions observed in the static investigation. The drag effects were ignored for this study as well as the work required to hold the desired deflection with a tab deflection. In order to maintain the desired lift coefficient, which would be greatly affected by tab movement, either the angle of attack of the aircraft or flap angle would need to be adjusted. In any case, this simplified dynamic analysis proves the merit of using tab deflections to actuate the flap even if the exact amount of power savings would be reduced with a more complete analysis.

3.7.4 Non-linear Behavior Cases

The data presented in Section 3.3, 3.5 and Appendix C displayed several instances of unexpected behavior. While the cause of this behavior is not critical with respect to the experimental objectives of this study, it was deemed important to understand the sources of the behavior. This would contribute to the understanding of the aerodynamics of a NACA 3415 with a 25%-chord flap and tab.

The cases selected showed behavior that differed from expected trends in either the lift, drag or hinge moment for both surfaces and consist of a given flap and tab deflection. To begin, the flow-visualization results for δ_f and δ_t = 0 deg. will be presented for comparison purposes. The tab hinge moment data for δ_f = -5 deg. and δ_t = 0 deg., shown below, exhibited different behavior from that seen for the 0 deg. flap deflection and will be studied in Section 3.7.4.2. Additionally, unexpected behavior in the flap and tab hinge moment data was common when the flap and tab deflections were of opposite sign. Two cases best represent this phenomena: flap deflection of -10 deg. with a tab deflection of 30 deg. and the opposite situation with δ_f = 10 deg. and δ_t = -30 deg. and are examined further in Sections 3.7.4.3 and 3.7.4.4, respectively. Lastly, a large decrease in the drag was seen in the angle of attack range just before stall for δ_f = -30 deg. and δ_t = -30 deg. creating a "bucket" in the drag curve. The results of the study into the cause of the drag "bucket" will be given in Section 3.7.4.5.

Surface oil flow visualization was carried out for each of the above cases given that the most likely cause of the behavior mentioned was tied to a boundary-layer issue. In addition to flow visualization, surface and wake pressure data was also used in support of the analysis.

3.7.4.1 Reference case: δf and δt = 0 deg.

As mentioned above, flow visualization was performed on the NACA 3415 with undeflected surfaces for an understanding of the basic flowfield features of the airfoil. Thus the results will provide for a comparison between all of the cases below in Sections 3.7.4.2 – 3.7.4.5. Three angles of attack were chosen: 0, 7 and 14 deg. to sample the linear range of lift as well as an angle of attack around stall. The resulting images are shown in Figs. 3.19 – 3.21.

The regions of flow are labeled in Fig. 3.19 for the upper surface. A transition region can be seen on both surfaces and roughly spans 10% of the chord while the location is further aft at this angle of attack on the upper surface. An additional region of low shear is apparent on the upper surface of the tab. Increasing angle of attack to 7 deg., seen in Fig. 3.20, resulted in the transition region moving forward to around x/c = 0.27 on the upper surface and sliding back to the leading edge of the flap on the lower surface. The low-shear region became larger as well. Further increase in angle of attack to 14 deg., seen in Fig. 3.21, led to the appearance of a separation region for the last 40% of the airfoil on the upper surface. The transition region moved further forward to the first 5% of the airfoil. Looking back at lift data in Fig. 3.4, an

angle of attack of 14 deg. corresponds to a point just past stall. The flowfield on the lower surface remained relatively unchanged.

3.7.4.2 Non-linearity in tab hinge moments: δ_f = -5 and δ_t = 0 deg.

Observing the tab hinge moment for zero and -5 deg. flap deflections with δ_t = 0 deg., Fig. 3.22, the behavior of the data differed from that of the other flap deflections, with exception to the -10 deg. flap deflection. The constant negative slope with increasing angle of attack occurred only for a small α range for δ_f = 0 deg. and only after stall for δ_f = -5 deg. To diagnose this change in slope, flow visualization was performed at α = -2 and 8 deg. which provides a point at which the slope changes from negative to positive as well as a point during the linear range where the slope is positive. The images for these angles of attack and both surfaces are presented in Figs. 3.23 and 3.24, respectively.

The flow visualization results show that at an angle of attack of -2 deg. there is completely attached flow on the upper surface with transition occurring between *x/c* = 0.50 – 0.55. Transition occurred earlier at *x/c* = 0.15 on the lower surface with a low-shear region on the flap and separation on the tab. Comparing to the reference case of δ_f and δ_t = 0 deg., the opposite was true of the tab flowfield in which a low-shear region was observed on the upper surface. The lower-surface separation off of the tab produces a larger negative tab hinge moment and was unexpected for only -5 deg. of deflection of the flap. At an angle of attack of 8 deg., the flow was attached on the lower surface of the tan with a low-shear region present on the upper surface causing the hinge moment to decrease in magnitude and approach zero.

From analysis of the pressure distributions of the flap deflections that exhibited normal linear behavior until stall, the non-linearity in the -5 deg. flap deflection tab hinge moment is likely a result of the large changes in the flowfield on the tab with increasing angle of attack. The reattaching of flow on the lower surface coupled with the onset of separation on the upper surface generated a consistent increase in tab hinge moment with angle of attack until stall while the other cases saw a consistent decrease with angle of attack.

3.7.4.3 δ_f = -10 and δ_t = 30 deg.

A consistent trend of non-linear behavior was observed with flap and tab deflections of opposite sign. The δ_f = -10 deg. and δ_t = 30 case is one of two that best exemplified the trend. In Fig. 3.8, the behavior of the flap and tab hinge moments undergoes a gradual change between δ_t

= 15 deg. and the largest tab deflection of 60 deg. The hinge moments begin to drop significantly becoming more negative in the angle of attack range of 0 to 10 deg. Past α = 10 deg., the slope of the flap hinge moment data became less negative while the tab hinge moment data levels out. Post-stall behavior was as expected. An angle of attack in the 0 to 10 deg. range was chosen, along with one on either side of the range, for inspection of the flowfield through flow visualization. The results are shown in Figs. 3.25 – 3.27.

At an angle of attack of 0 deg., seen in Fig. 3.25, the flow separated off of the tab on the upper surface and off of the flap on the lower surface. In addition, the large positive tab deflection created a separation bubble which would have extended off of the airfoil with a smaller tab deflection and is evident through the presence of an impingement line on the lower surface of the tab around mid-tab in the chordwise direction . The impinging of the flow on the tab created a larger negative tab hinge moment than what would have been measured otherwise. Since this angle of attack corresponds to the onset of the drop in flap and tab hinge moment, this was most likely the cause. Additionally, increasing angle of attack to 7 deg., shown in Fig. 3.26, led to the flow reattaching completely on the tab lower surface while the flow remained separated on the tab upper surface. The suction on the upper surface due to separation further increased the magnitude of the hinge moment. Since the upper and lower surface flowfield on the flap and tab remained relatively unchanged between α = 7 and 13 deg., seen in Fig. 3.27, the tab hinge moment became almost constant as well.

The flap hinge moment continued to decrease during the range in which the tab hinge moment was constant. In Fig. 3.27, the flow visualization revealed separation occurring beginning at an *x/c* location of 0.70 on the upper surface resulting in a more negative flap hinge moment. The growth of the separation region would then cause the flap hinge moment to continue to increase in magnitude.

3.7.4.4 δ_f = 10 and δ_t = -30 deg.

Another example of the trend observed with flap and tab deflections of opposite sign was the δ_f = 10 and δ_t = -30 deg. case, the hinge moment data for which can be seen in Fig. 3.8. Similar to the δ_f = -10 and δ_t = 30 deg. case, a change in behavior was seen beginning with a tab deflection of -30 deg. However, further deflection of the tab produced another change in behavior that matches that of the -30 deg. tab deflection from -6 to 5 deg. angle of attack; then, above α = 5 deg., the curves tend to follow the behavior of the remaining tab deflections. Again

the flap and tab hinge moment behavior was almost identical with exception to the tab hinge moment which slope was more negative than the flap hinge moment.

Flow visualization was performed at two angles of attack: 0 and 14 deg. The results for α = 0 deg. are shown below in Fig. 3.28. Comparison of these images to that for the δ_f = -10 deg. and δ_t = 30 case reveals a similar flowfield between the two cases. An impingement line is apparent on the upper surface of the tab while separation can be seen on the tab lower surface. This situation leads to a larger positive flap and tab hinge moment. While there were no flow visualization runs performed at intermediate angles of attack, the same flowfield progression seen for the δ_f = -10 deg. and δ_t = 30 case is expected.

Increasing angle of attack to 14 deg., shown in Fig. 3.29, caused flow to separate at an *x/c* location of 70% on the upper surface. The flow remains mostly separated on the tab lower surface with pockets of attached flow. The data show the hinge moment for the tab increasing post stall which indicates the flowfield on the lower surface of the tab with the pockets of reattached flow is the cause. The same is true for the flap since the flow is completely attached on the lower surface of the flap. Increasing the negative tab deflection would create a completely separated flowfield on the lower surface resulting in a drop in hinge moment leading to the change in post-stall behavior observed for tab deflections of -45 and -60 deg.

3.7.4.5 δ_f = -30 and δ_t = -30 deg.

The last case that was further studied was the drag "bucket" evident in the data for a -30 deg. flap and tab deflection, below in Fig. 3.12. For each of the other tab deflections for a flap deflection of -30 deg., the drag remained relatively constant until in the angle of attack range before stall. The -30 deg. tab deflection case stands out as the drag before stall drops significantly below that of each of the other tab deflections. Five angles of attack were selected for flow visualization runs to best capture the flowfield progression from the linear drag range at lower angles of attack to onset of the drag decrease followed by the angle of attack for minimum drag and onset of stall. Thus the most appropriate angles of attack were deemed to be 0, 4, 7, 10 and 14 deg. The results for each are shown in Figs. 3.30 – 3.34, respectively.

Beginning with 0 deg. angle of attack, transition occurred at an *x/c* location of 50% on the upper surface and 7.5% on the lower surface. Separation and recirculation was also present on the lower surface of the flap and tab. Increasing angle of attack to 4 deg. (Fig. 3.31), which corresponds to the onset of drag decrease, the transition moved forward on the upper surface to

x/c = 0.425 and aft on the lower surface to x/c = 0.25. Additionally, the amount of recirculation on the flap was decreased.

At an angle of attack of 7 deg., the drag further decreased and the flow visualization shown in Fig. 3.32 indicates a complete laminarization of the flow on the lower surface of the main element. The areas of recirculation on the flap became larger as well which was mostly a three-dimensional effect due to the hinge slots and slots between each surface. Therefore, this laminarization was presumably the cause of the decrease in drag and explains the difference between the CFD and experimental data discussed in Section 3.6. The computational data were dependent upon the transition location which was fixed for both the upper and lower surface, thus not accounting for the laminarization phenomenon.

Figure 3.33 shows the results for α = 10 deg. which represents the minimum drag location. The flow remained unchanged on the lower surface with transition moving slightly forward on the upper surface. The drag increase in subsequent angles of attack suggests the beginning of separation on the upper surface and starts as a small separation bubble at the intersection of the main element and flap at α = 10 deg. The separation bubble extended to an x/c location of 55% for an angle of attack of 14 deg. (Fig. 3.34).

To understand how the laminarization of the lower surface contributes to the decrease in drag, the wake profiles were analyzed and compared to that of airfoil with zero flap and tab deflection. Figure 3.35 displays the wake profiles for a NACA 3415 with δ_f and δ_t = 0 deg. which moved downward with increasing angle of attack following the trailing edge and gradually increased in size. Separation on the upper surface causes the wake to increase further in size and retreat upward which was seen for α = 15 deg.

However, the wake profiles for a flap and tab deflection of -30 deg. tend to follow a different trend with increasing angle of attack. Shown in Fig. 3.36, the wakes moved downward following the trailing edge as expected but actually decreased in size. Examining the angles of attack associated with the onset of the decrease in drag, the lower edge of the wake remained relatively stationary. Since the lower edge of the wake was expected to follow the trailing edge downward with increasing angle of attack, the fact the lower edge remained fixed in the y direction indicates the wake due to the lower surface was shrinking causing the entire wake to shrink. Therefore, this effect resulted in less drag. In addition, the separated wake moved

downward as well which was opposite of the zeroed flap and tab case but is irrelevant to the drag “bucket” effect.

3.8 Figures

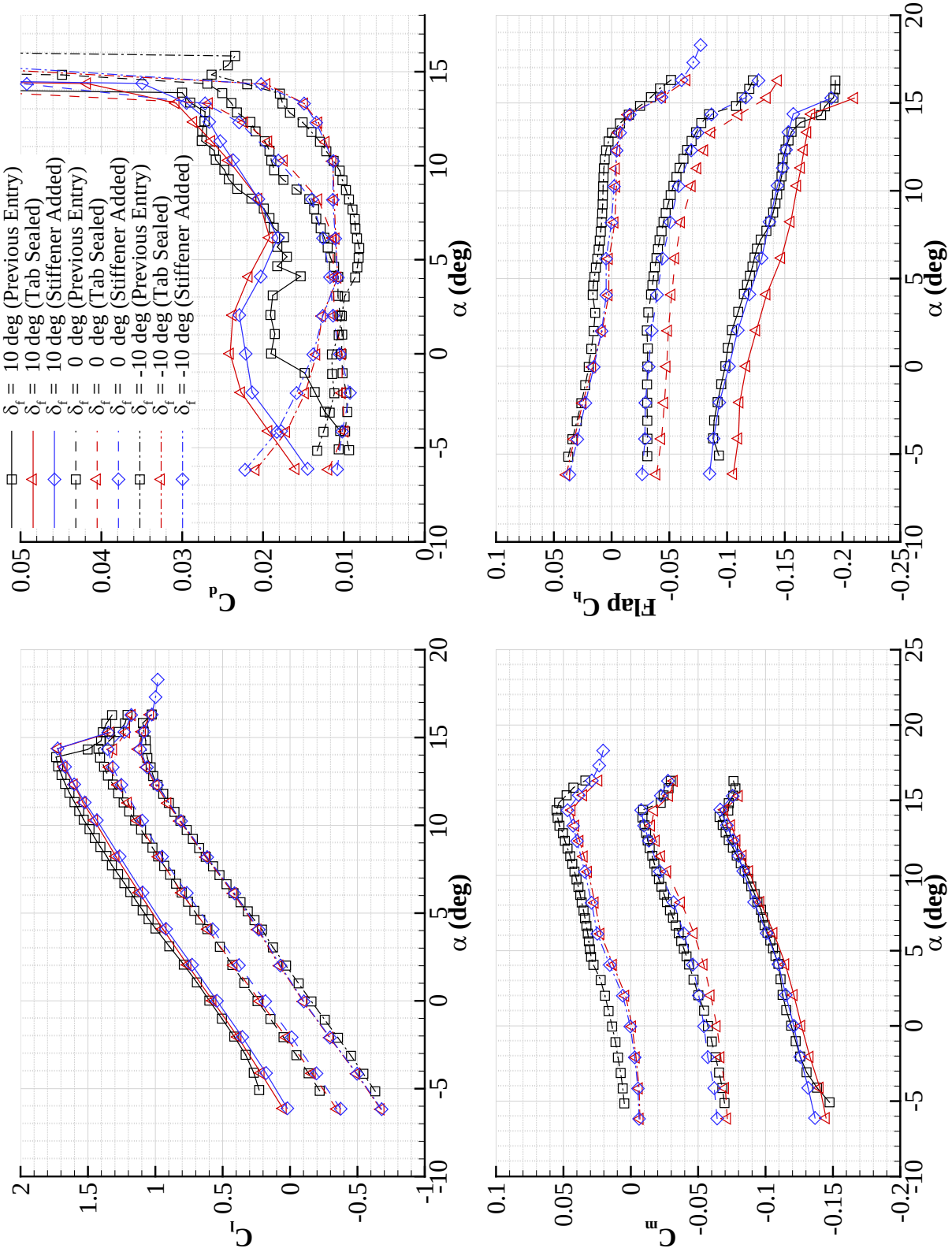

Fig. 3.1 Data comparison between previous and current NACA 3415 experiment.

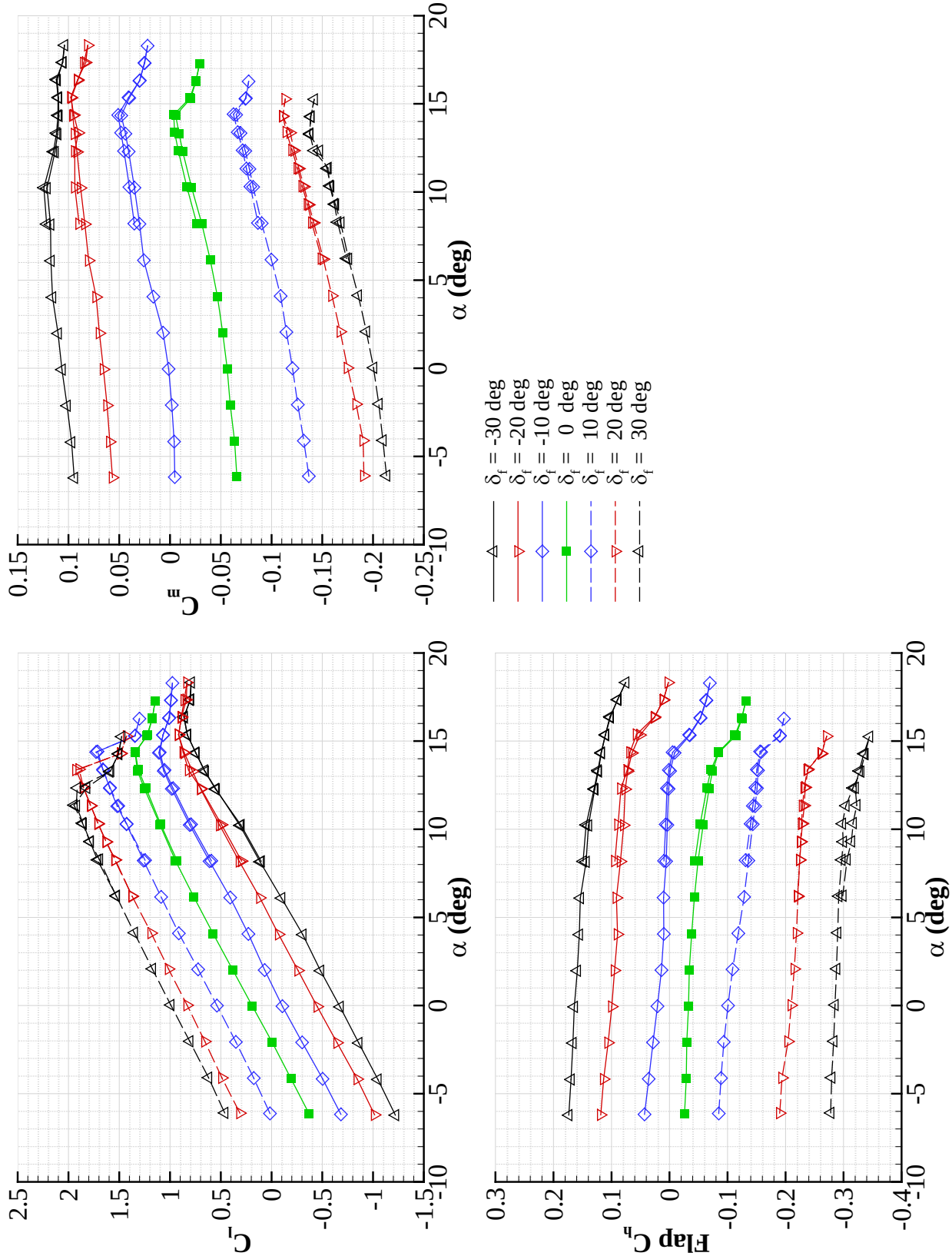

Fig. 3.2 Hysteresis in angle of attack analysis for NACA 3415.

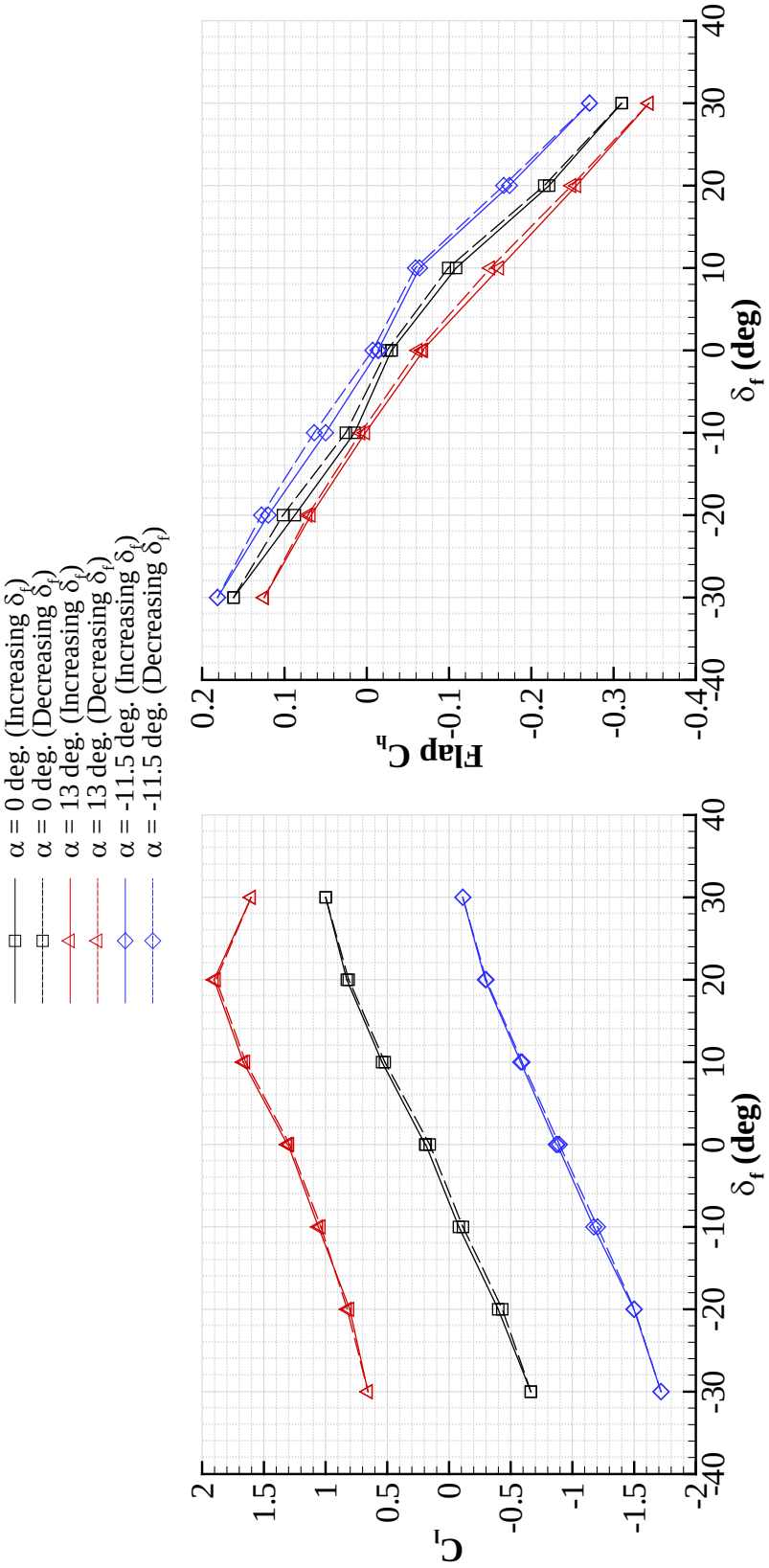

Fig. 3.3 Hysteresis in flap deflection analysis for flapped NACA 3415.

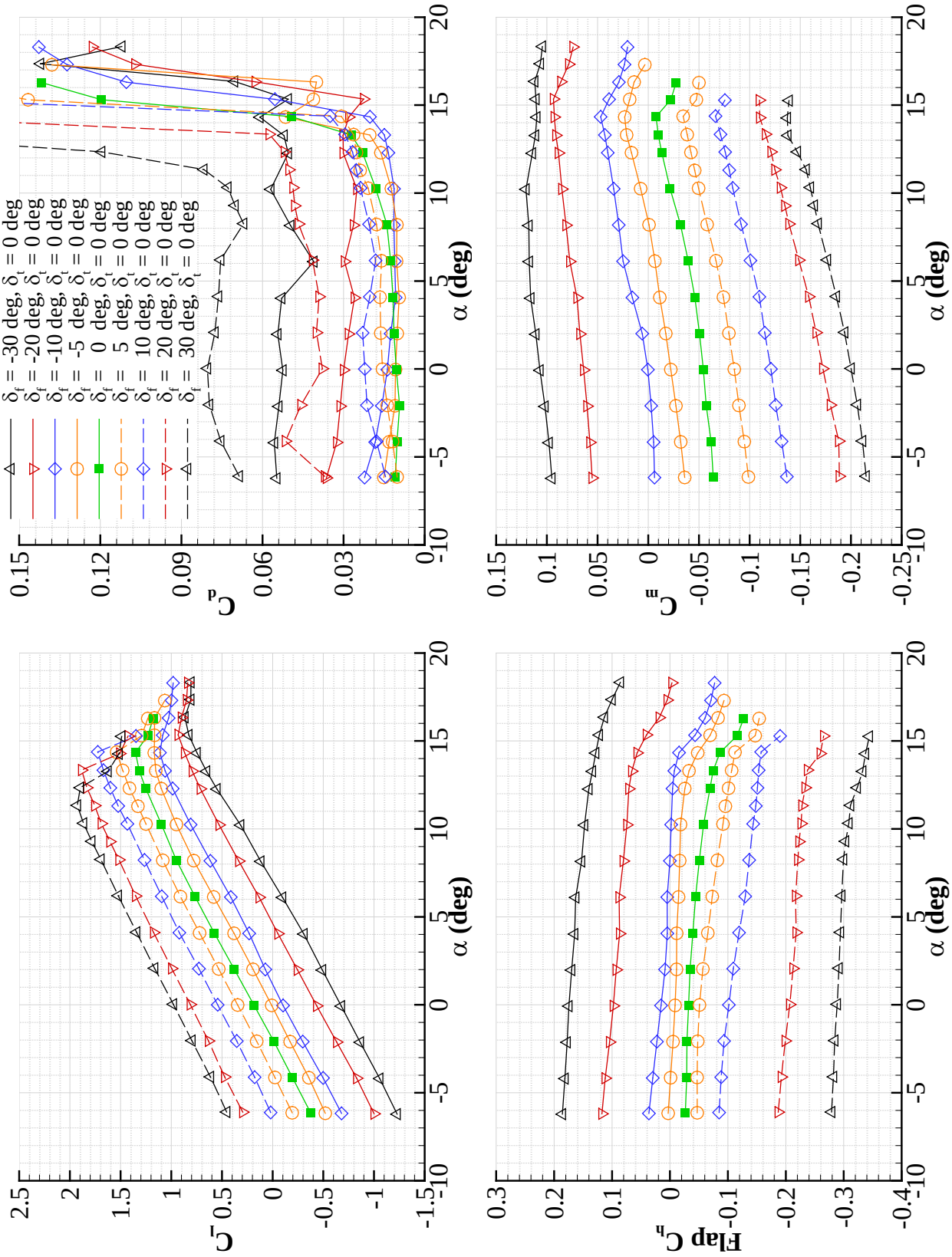

Fig. 3.4 NACA 3415 performance over range of flap deflections with δ_t = 0 deg.

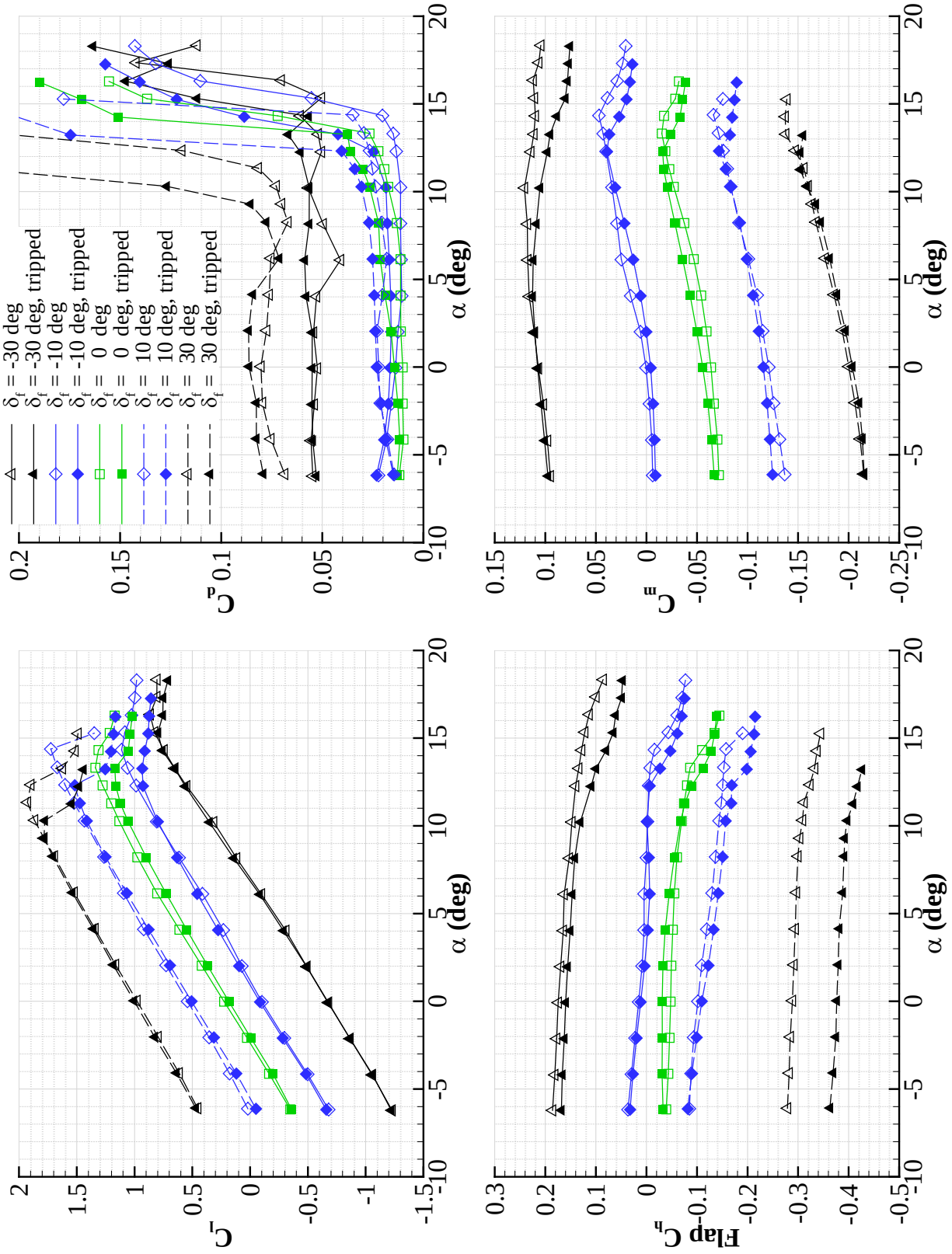

Fig. 3.5 NACA 3415 performance over range of flap deflections with δ_t = 0 deg. with boundary-layer trip.

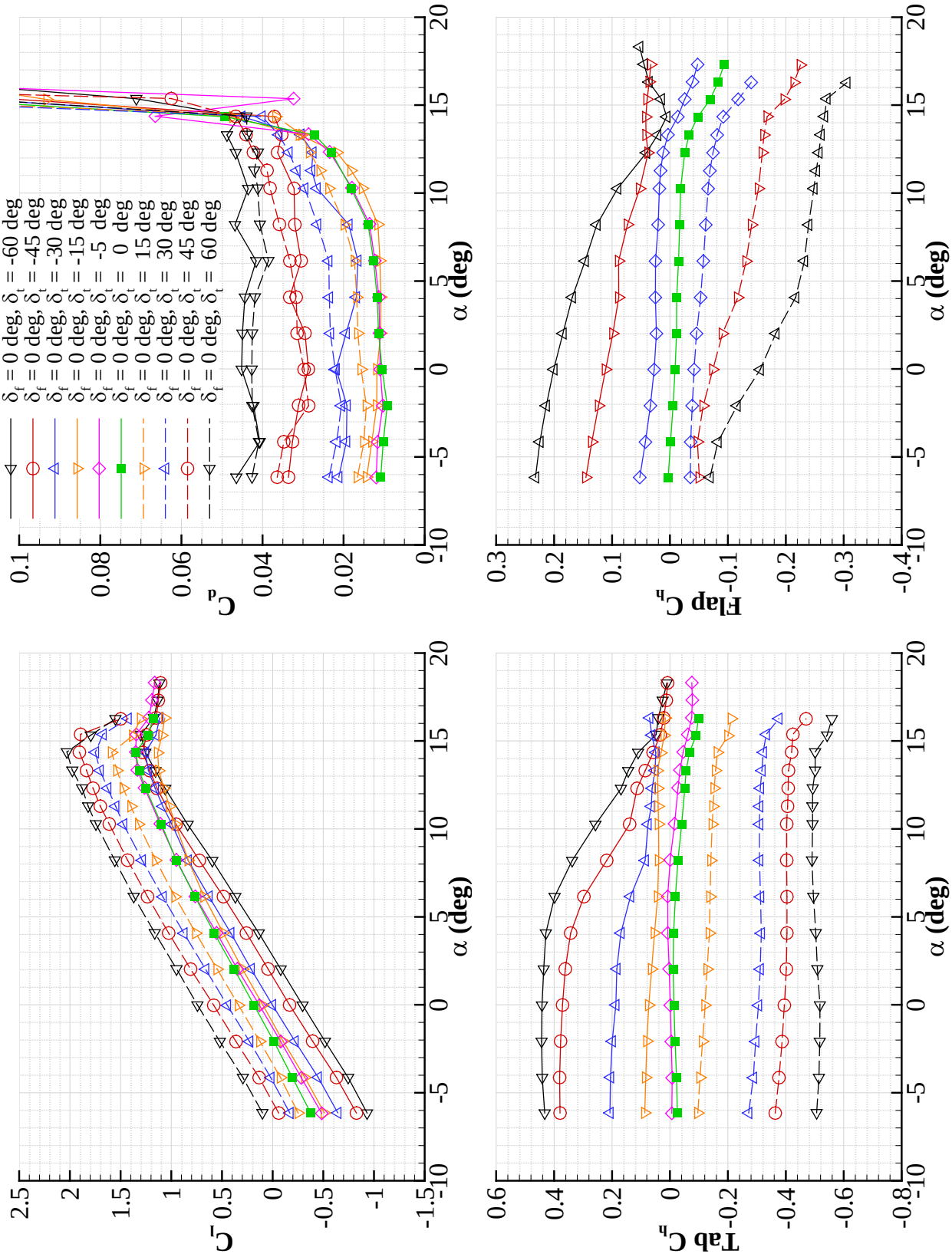

Fig. 3.6 NACA 3415 performance with δ_f = 0 deg. and range of tab deflections.

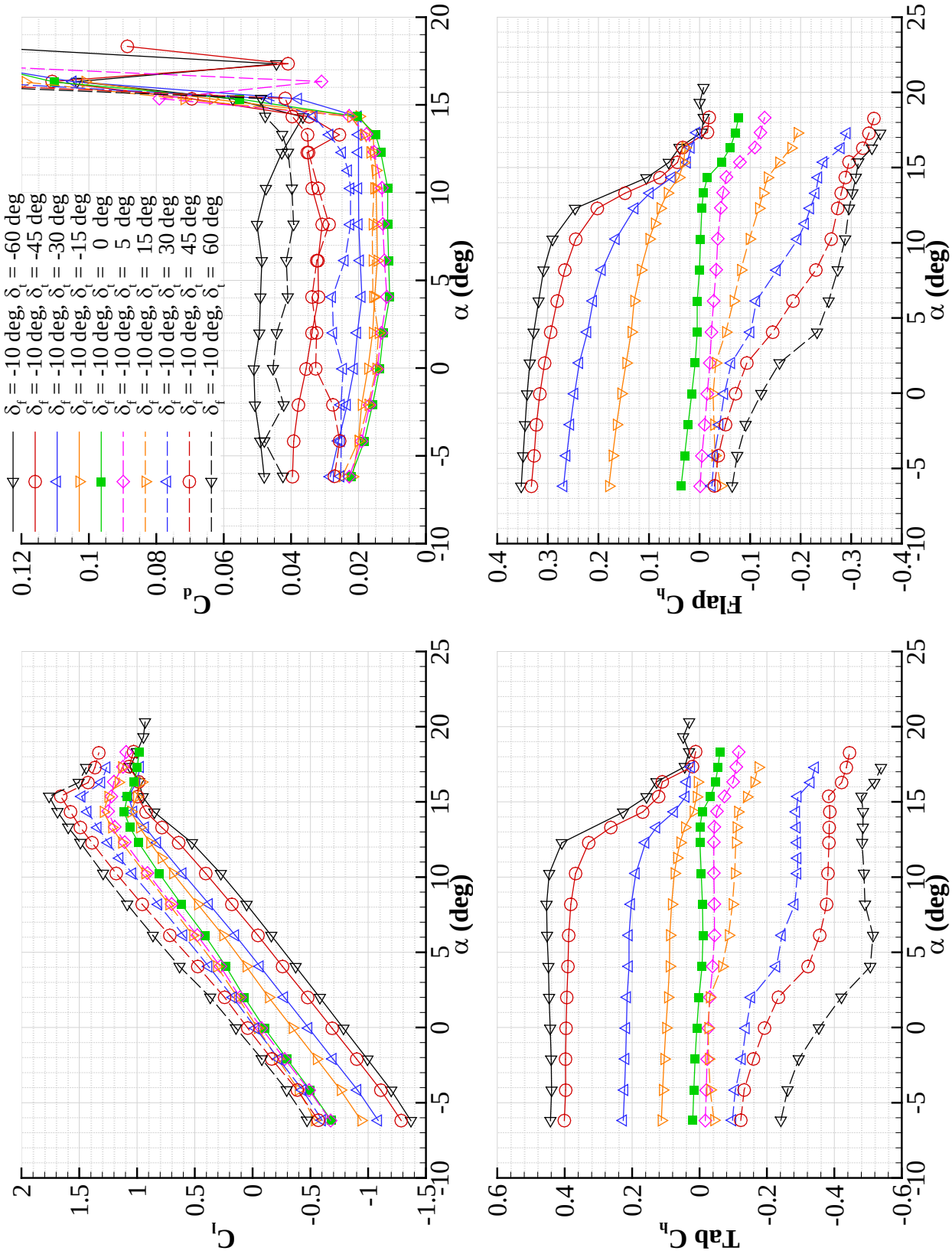

Fig. 3.7 NACA 3415 performance with δ_f = -10 deg. and range of tab deflections.

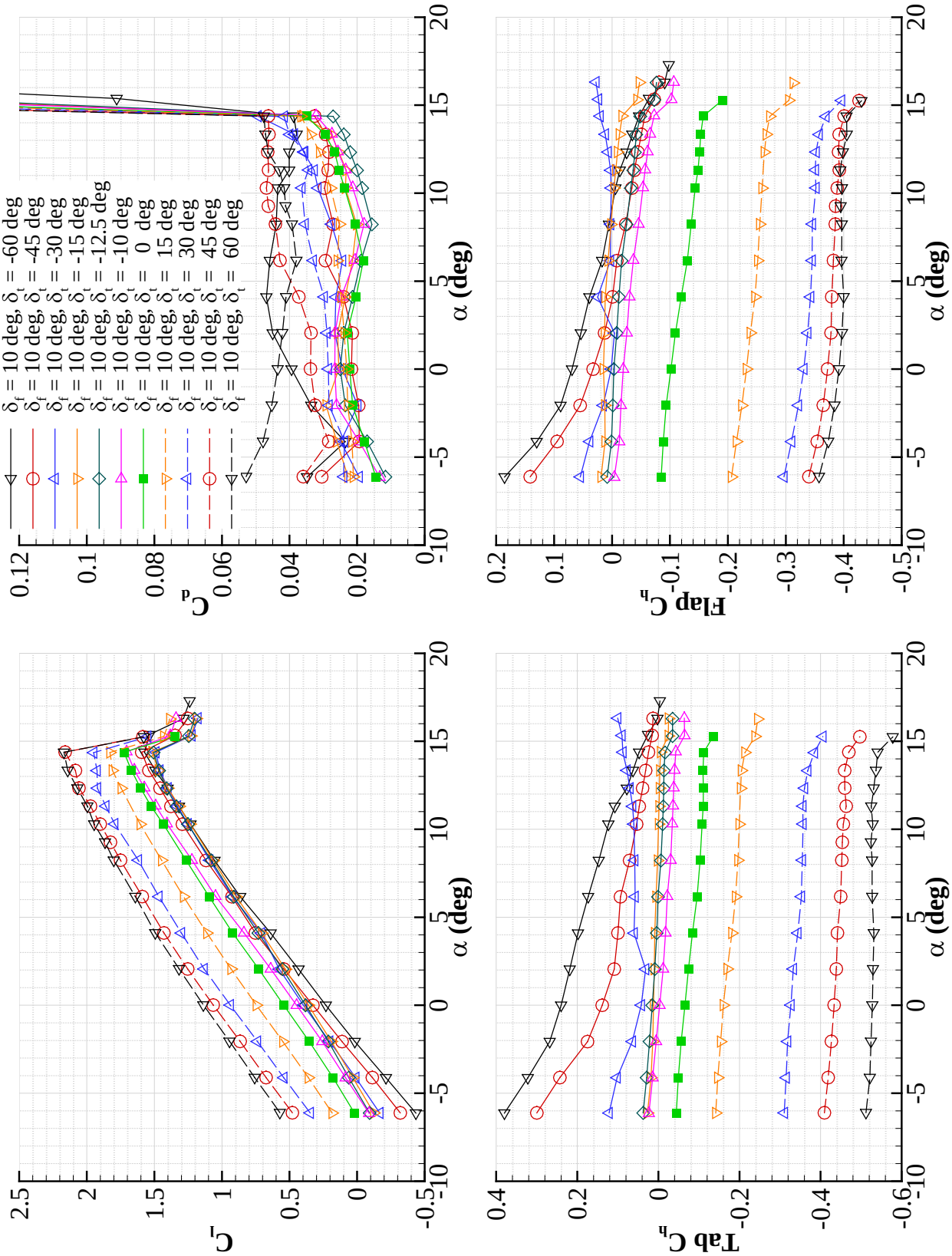

Fig. 3.8 NACA 3415 performance with δ_f = 10 deg. and range of tab deflections.

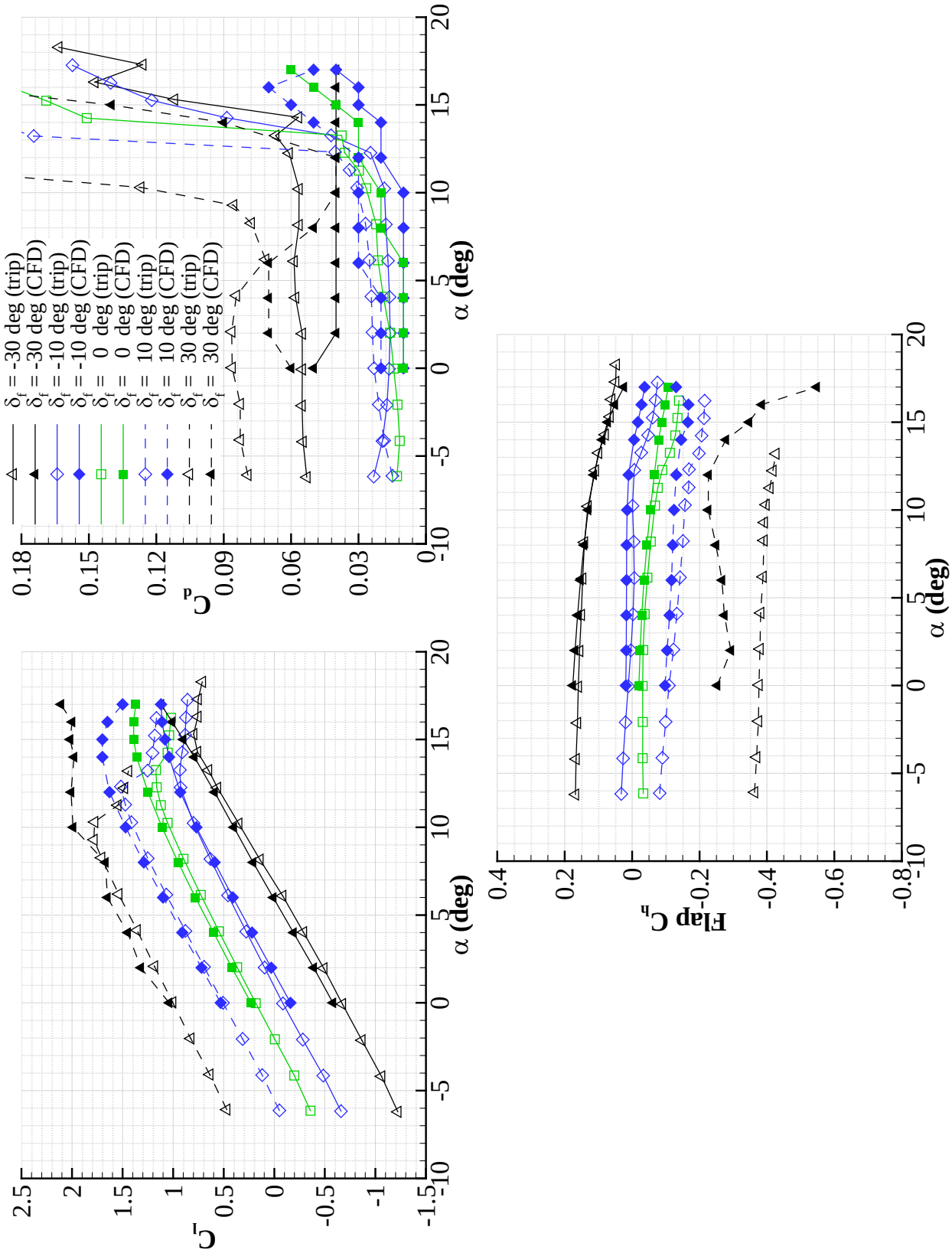

Fig. 3.9 CFD vs. exp. tripped data comparison for select flap deflections and δ_t = 0 deg.

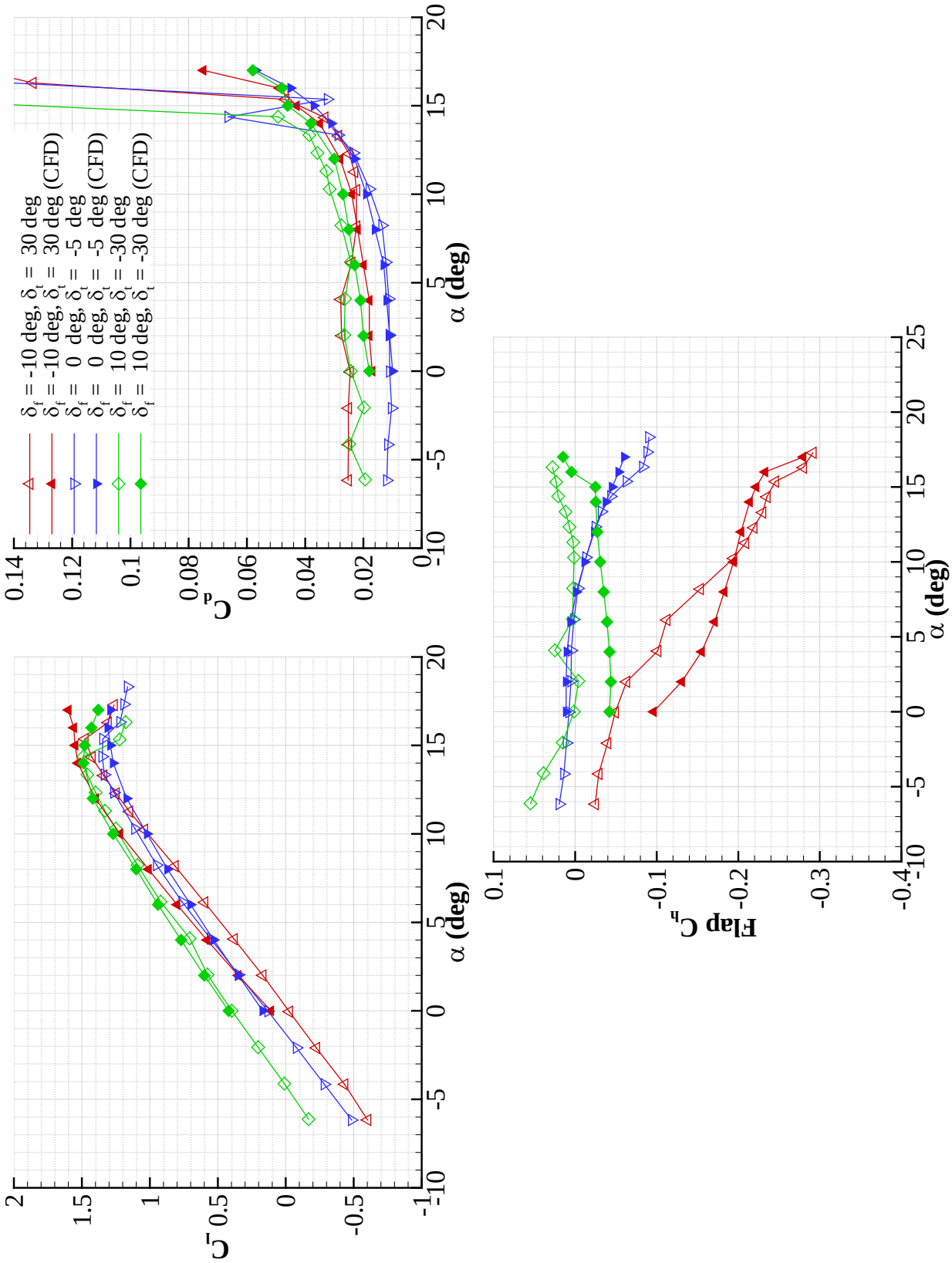

Fig. 3.10 CFD vs. exp. data comparison for select flap and tab deflections.

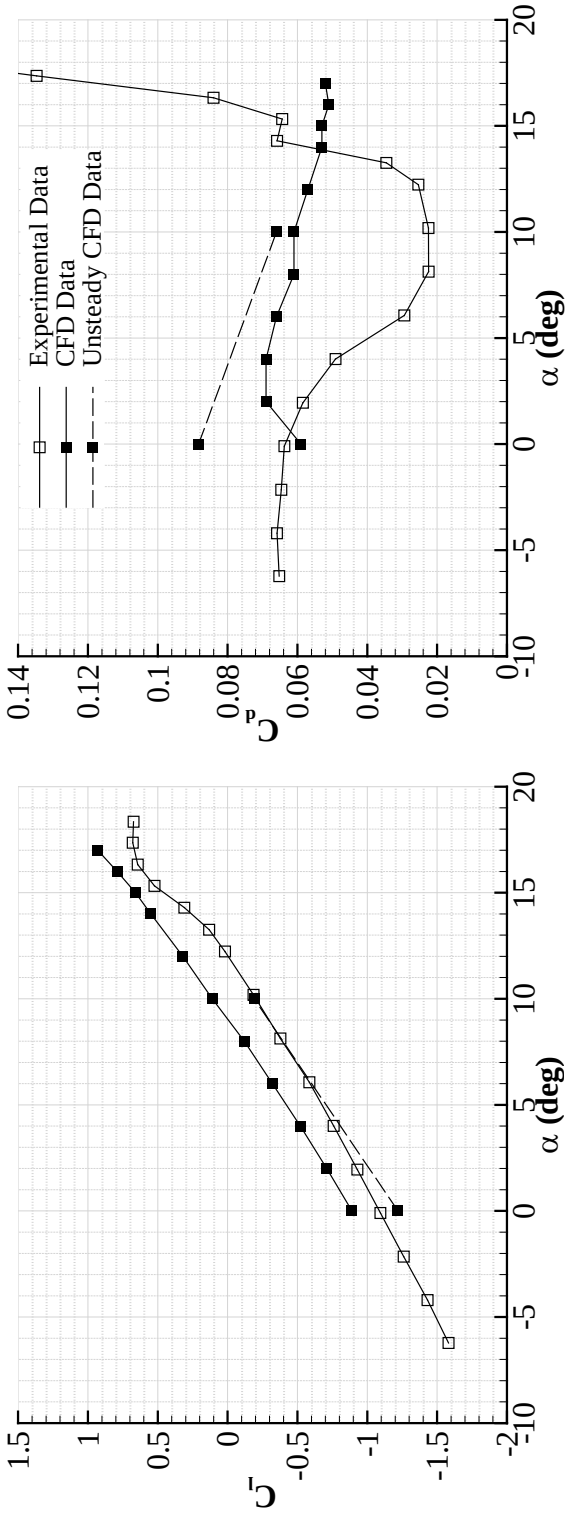

Fig. 3.11 CFD vs. experimental data comparison for δ_f = -30 deg. and δ_t = -30 deg. with additional unsteady CFD data.

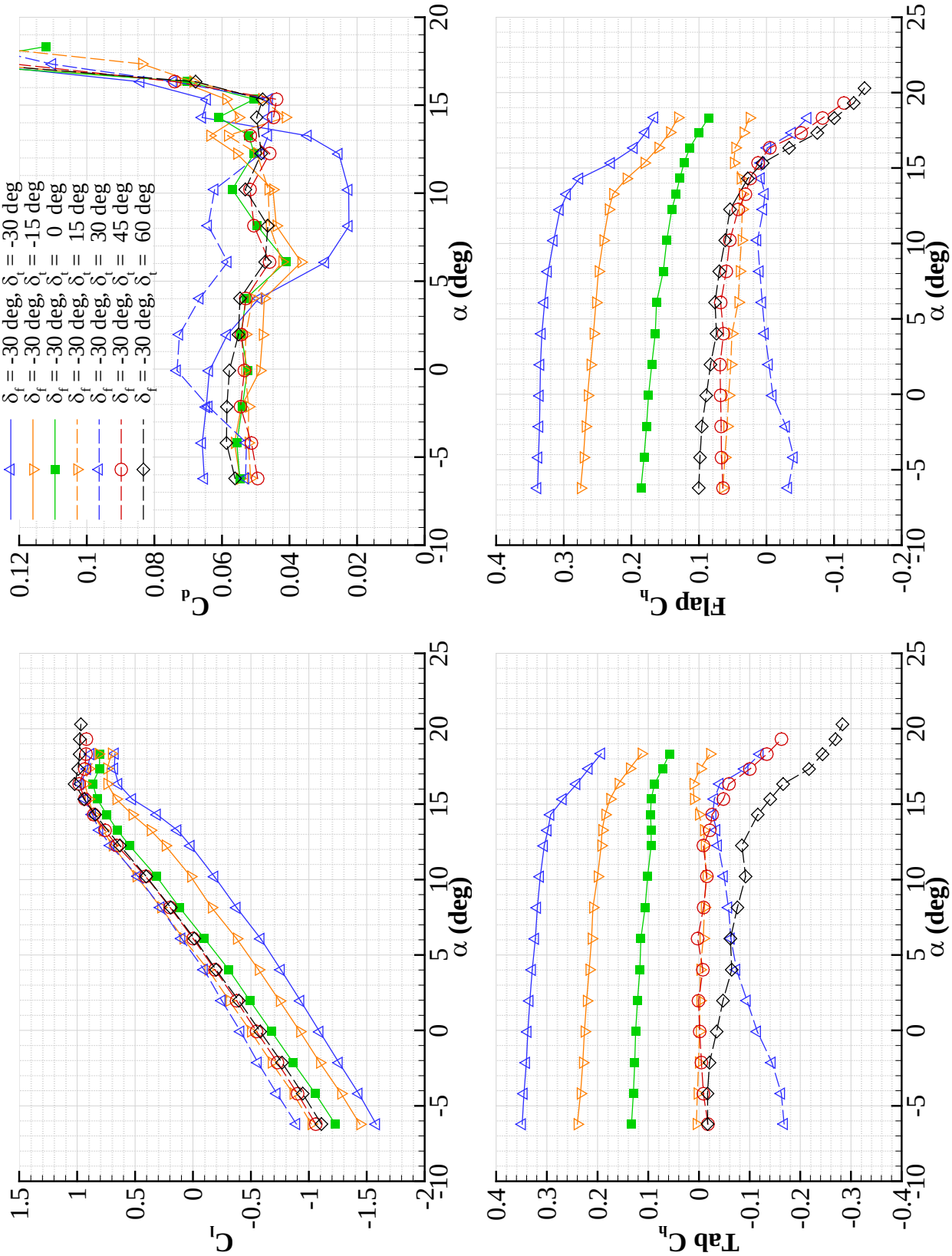

Fig. 3.12 NACA 3415 performance with δ_f = -30 deg. and range of tab deflections.

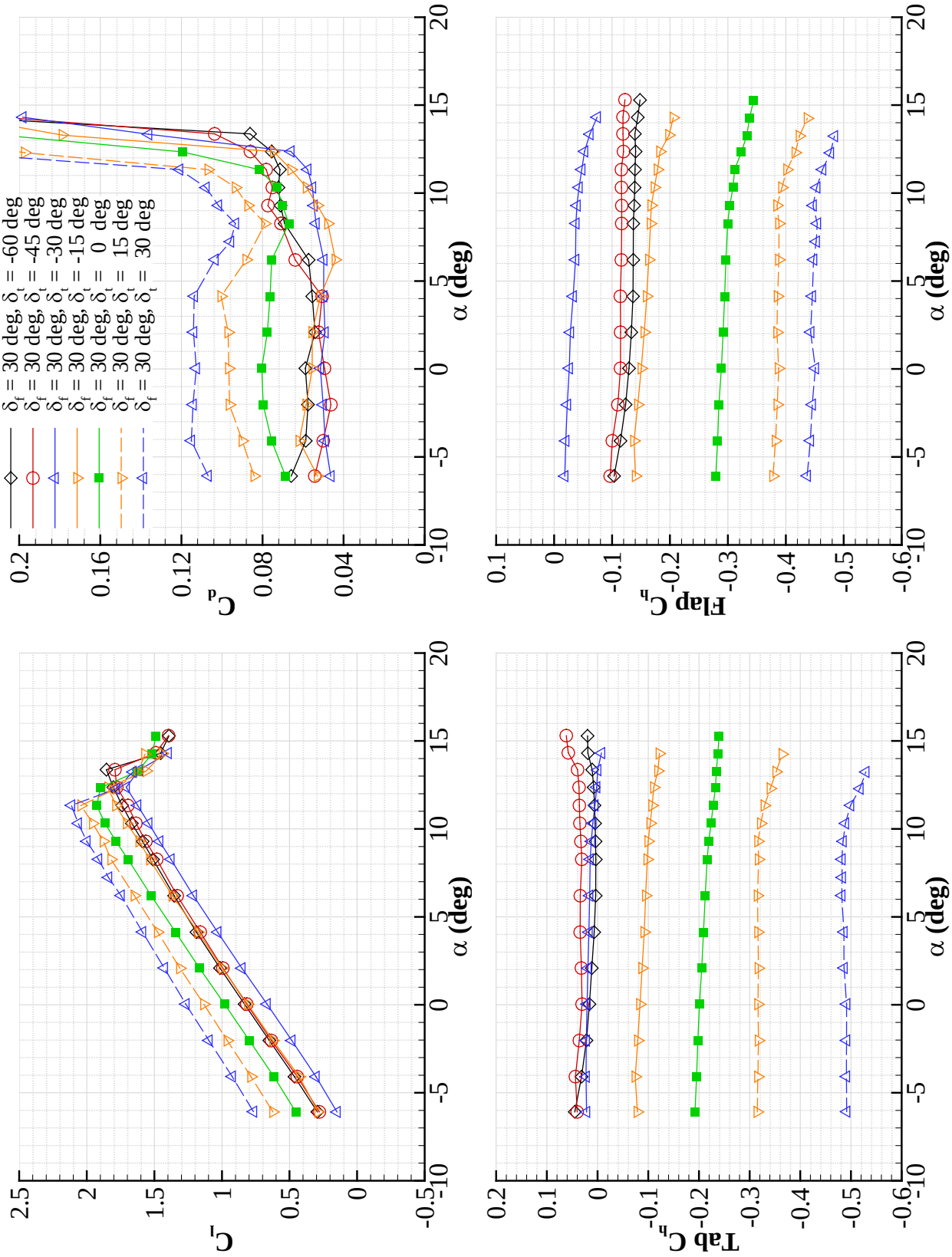

Fig. 3.13 NACA 3415 performance with δ_f = 30 deg. and range of tab deflections.

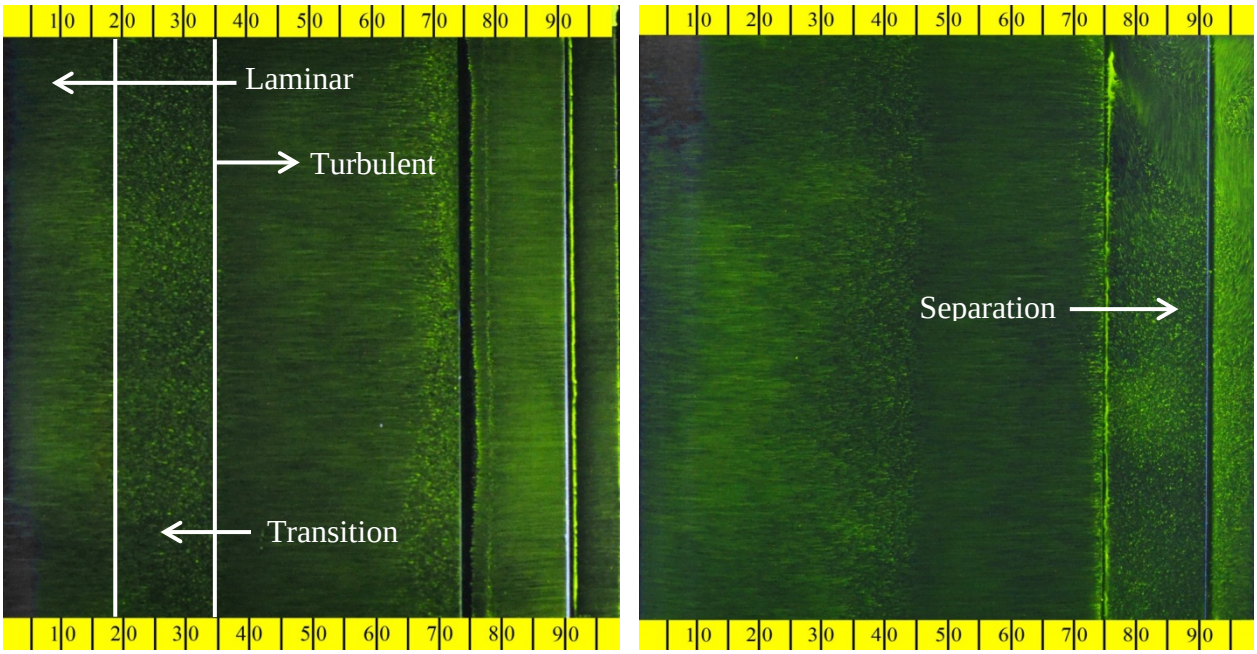

a) **b)**

Fig. 3.14 Surface-oil flow visualization for δ_f = 30 deg. and δ_t = -30 deg. on a) upper surface and b) lower surface.

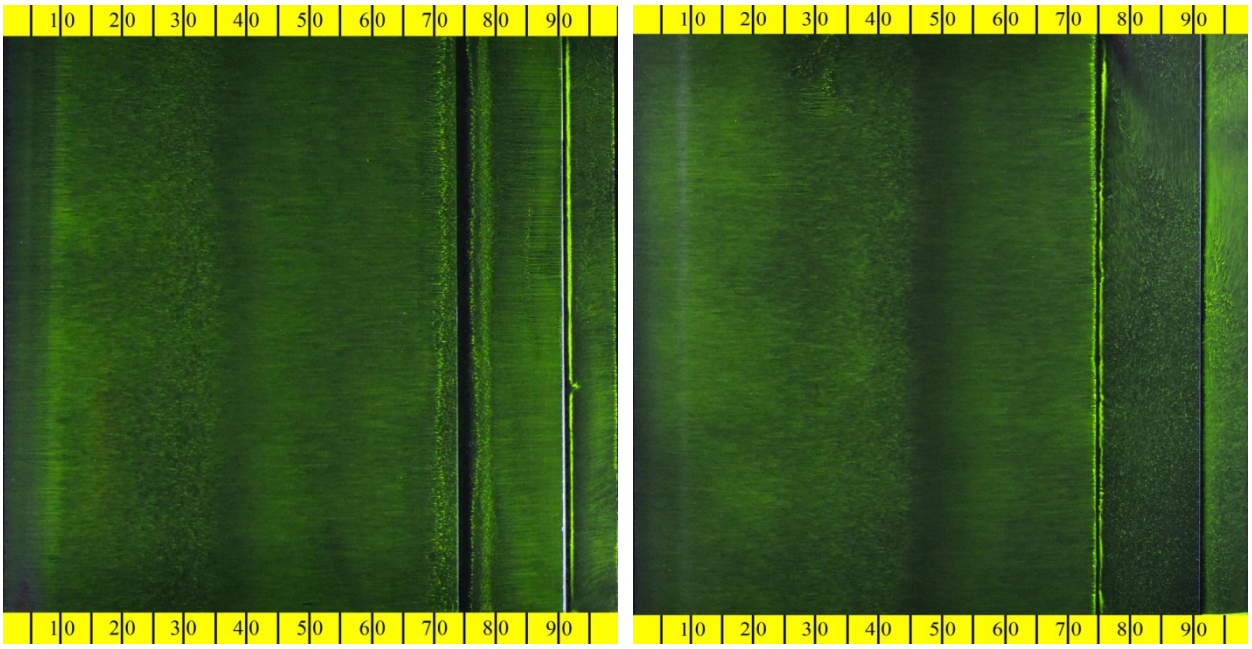

a) **b)**

Fig. 3.15 Surface-oil flow visualization for δ_f = 30 deg. and δ_t = -45 deg. on a) upper surface and b) lower surface.

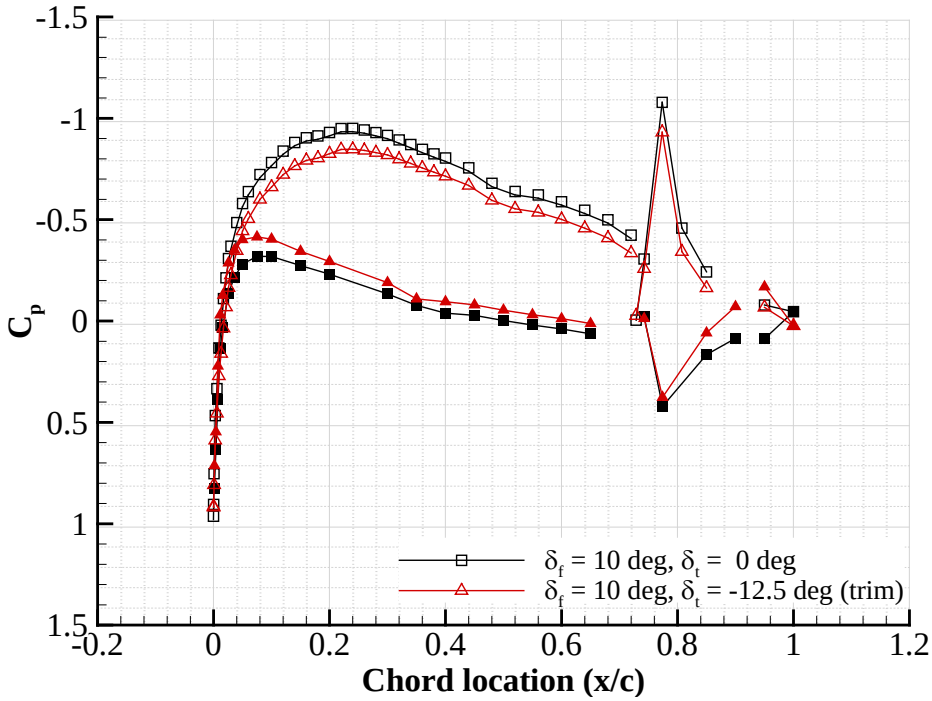

Fig. 3.16 C_p distribution of δ_f = 10 deg. for baseline and tab trimmed cases.

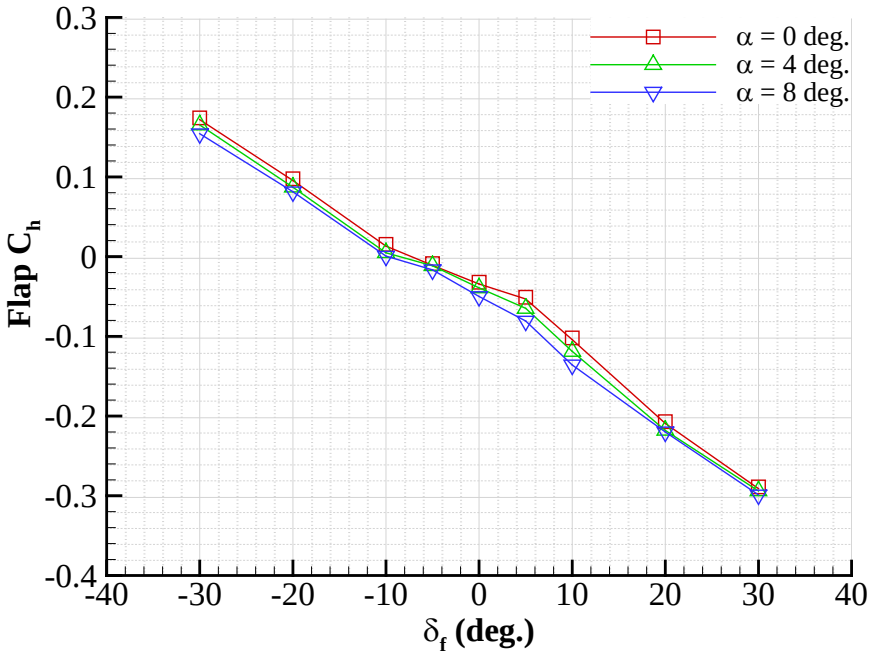

Fig. 3.17 Flap C_h vs. flap deflection for α = 0, 4 and 8 deg.

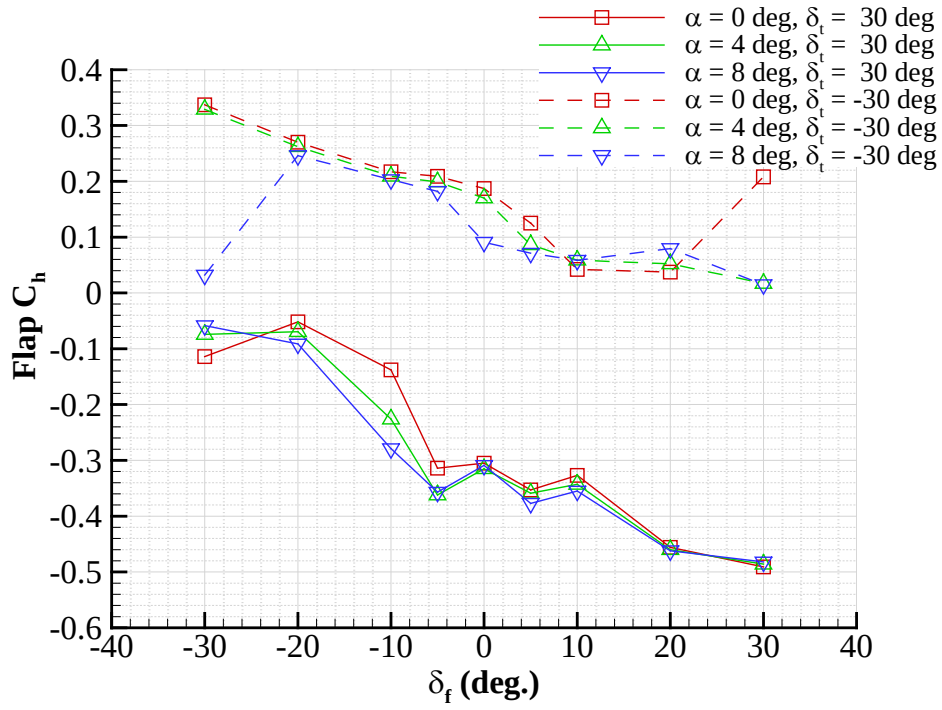

Fig. 3.18 Tab C_h vs. flap deflection for α = 0, 4 and 8 deg. and δ_t = ±30 deg.

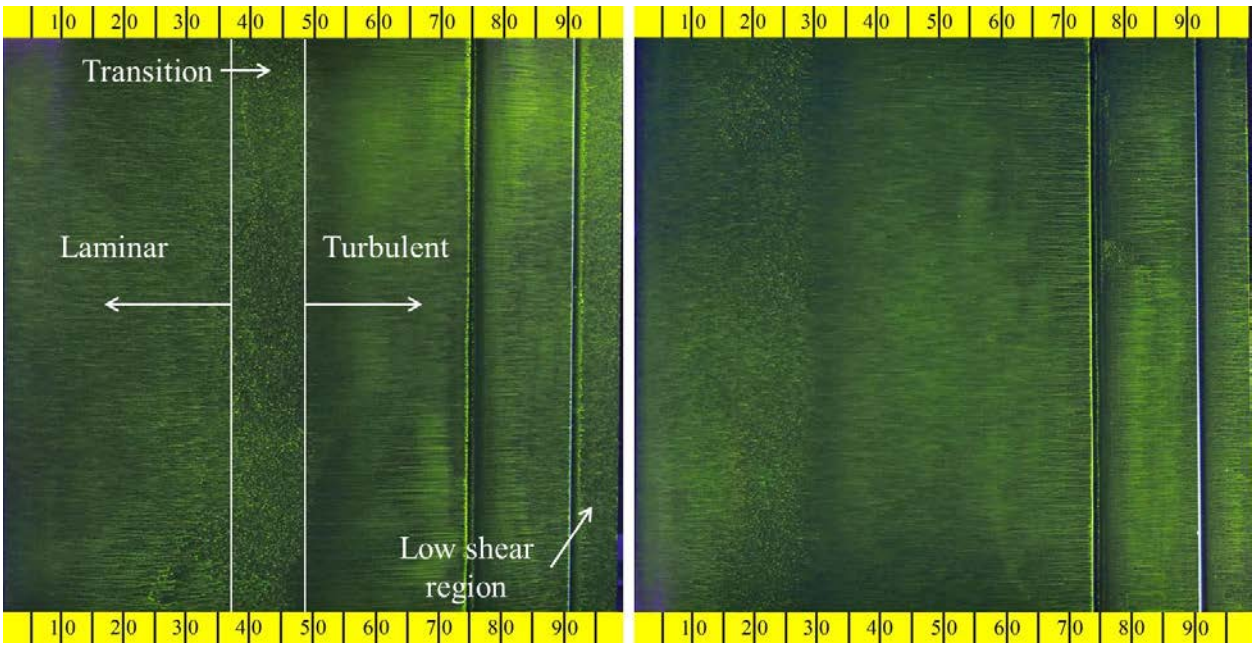

a) **b)**

Fig. 3.19 Flow visualization for δ_f and δ_t = 0 deg. at α = 0 deg. on a) upper surface and b) lower surface.

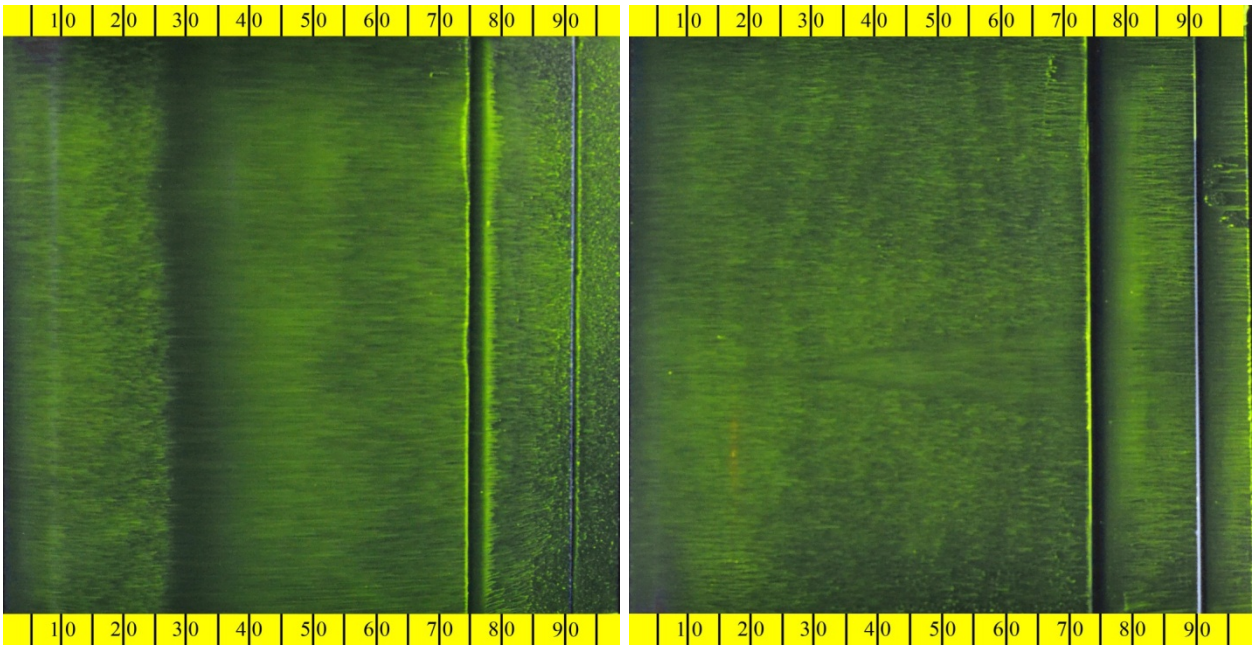

a) **b)**

Fig. 3.20 Flow visualization for δ_f and δ_t = 0 deg. at α = 7 deg. on a) upper surface and b) lower surface.

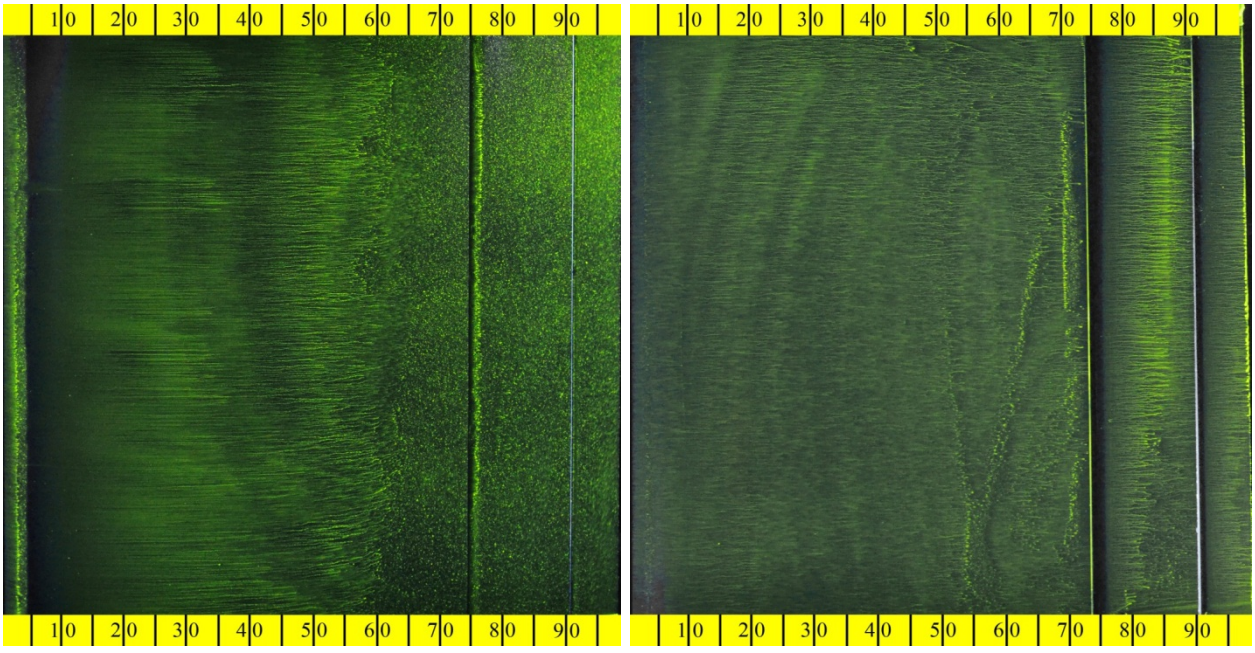

a) **b)**

Fig. 3.21 Flow visualization for δ_f and δ_t = 0 deg. at α = 14 deg. on a) upper surface and b) lower surface.

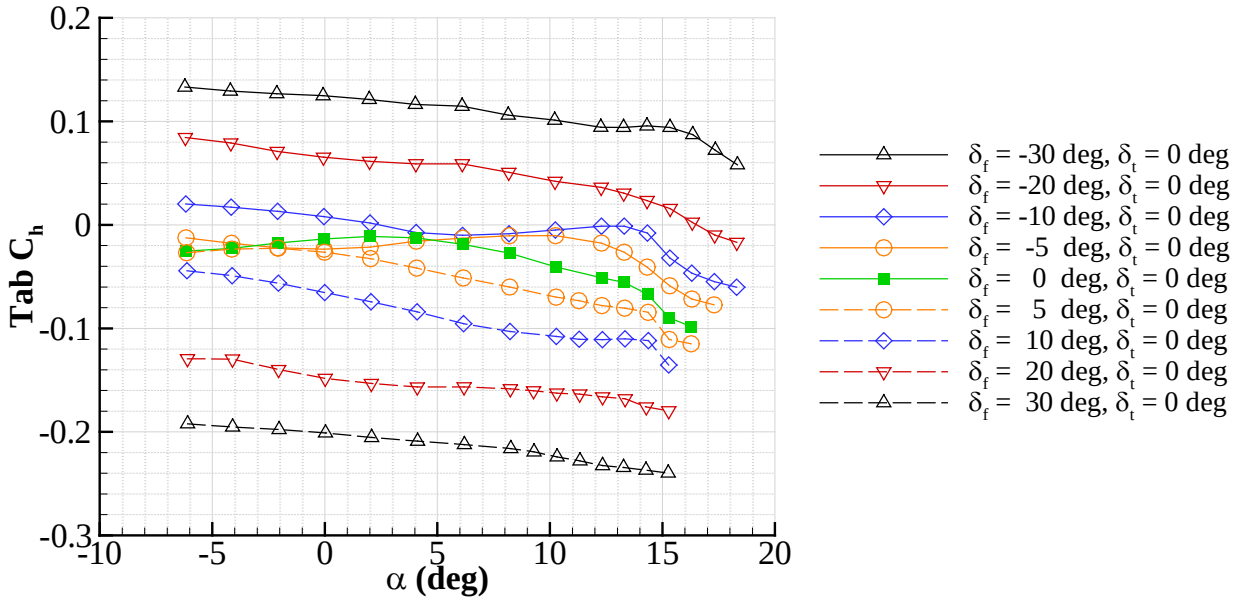

Fig. 3.22 Tab C_h for δ_t = 0 deg. and range of flap deflections.

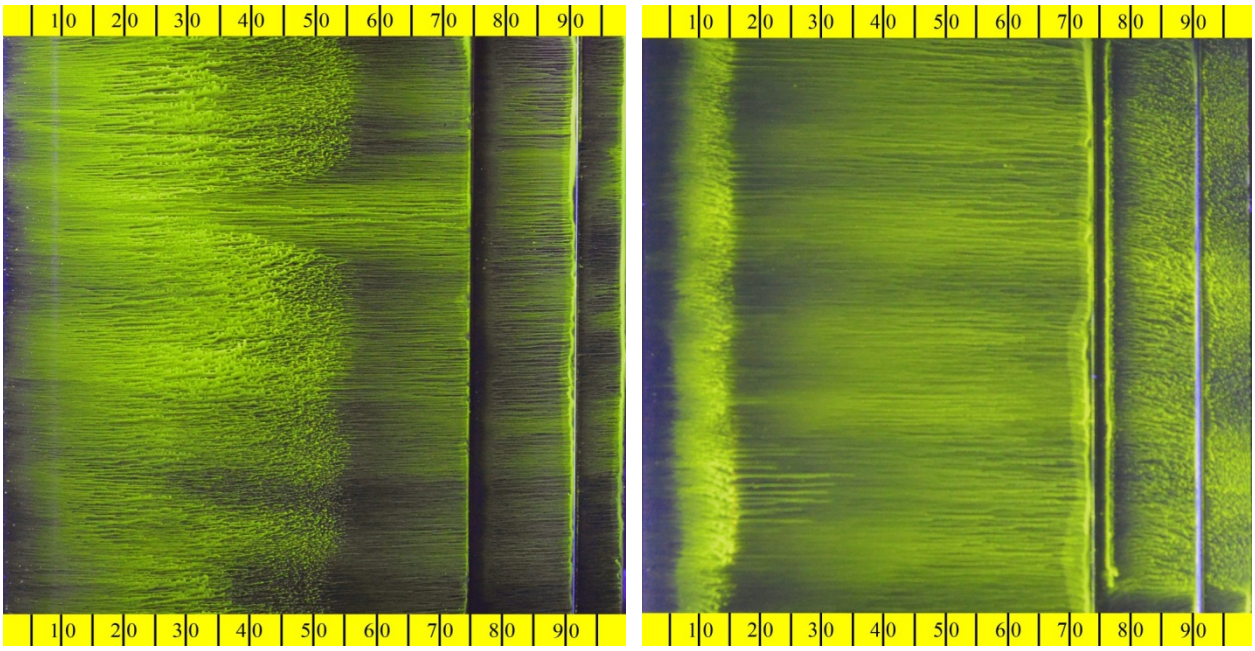

a) **b)**

Fig. 3.23 Flow visualization for δ_f = -5 deg. and δ_t = 0 deg. at α = -2 deg. on a) upper surface and b) lower surface.

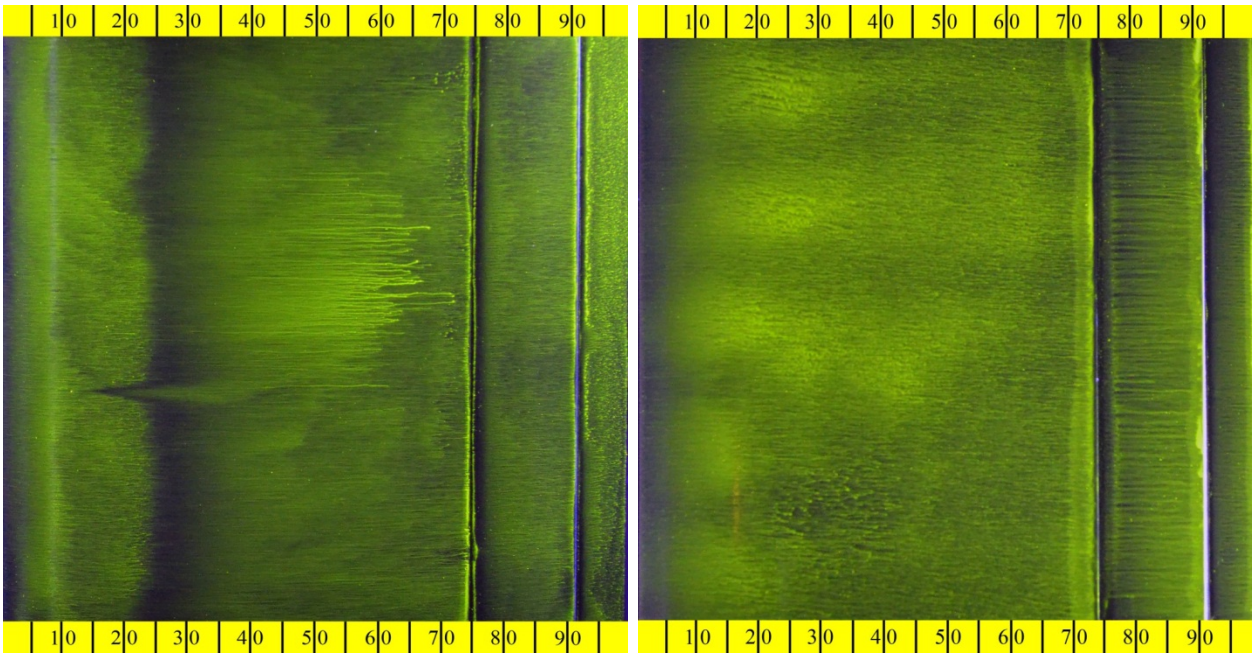

a) **b)**

Fig. 3.24 Flow visualization for δ_f = -5 deg. and δ_t = 0 deg. at α = 8 deg. on a) upper surface and b) lower surface.

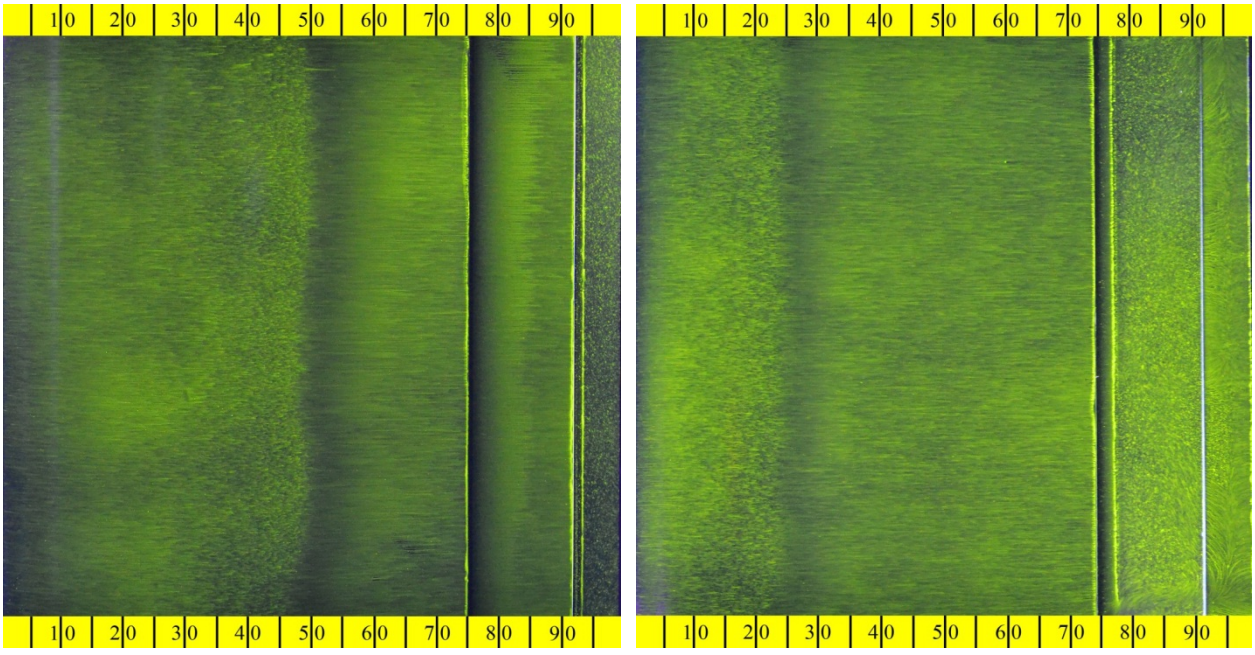

a) **b)**

Fig. 3.25 Flow visualization for δ_f = -10 deg. and δ_t = 30 deg. at α = 0 deg. on a) upper surface and b) lower surface.

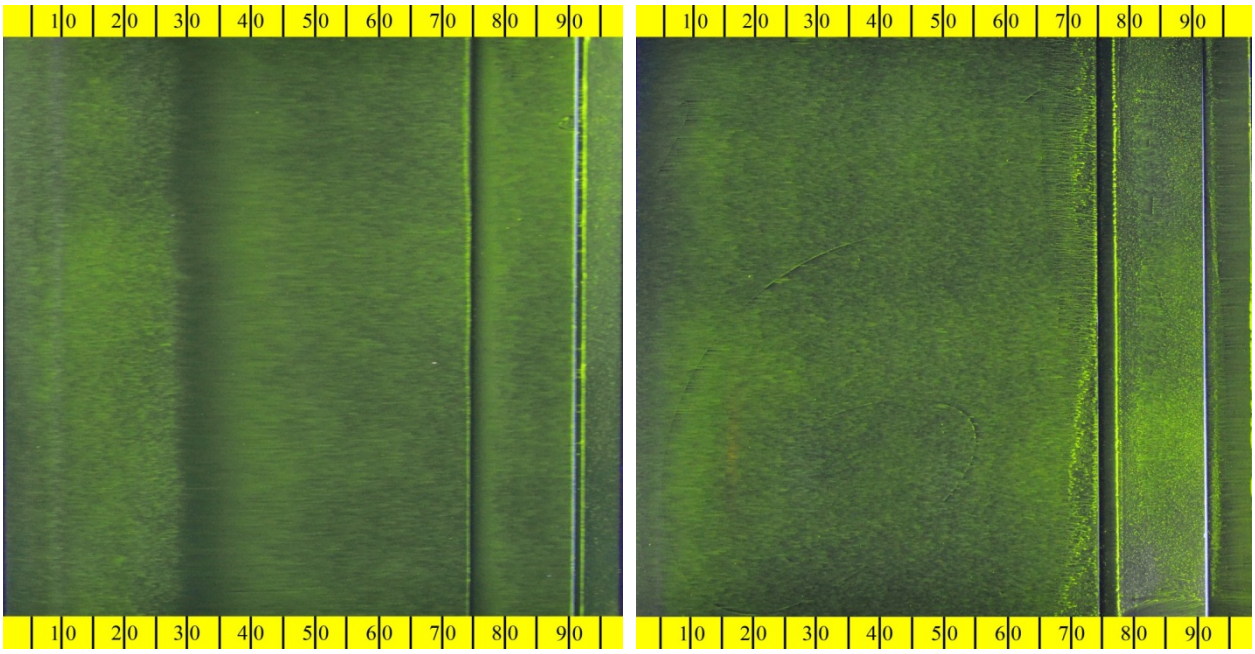

a) **b)**

Fig. 3.26 Flow visualization for δ_f = -10 deg. and δ_t = 30 deg. at α = 7 deg. on a) upper surface and b) lower surface.

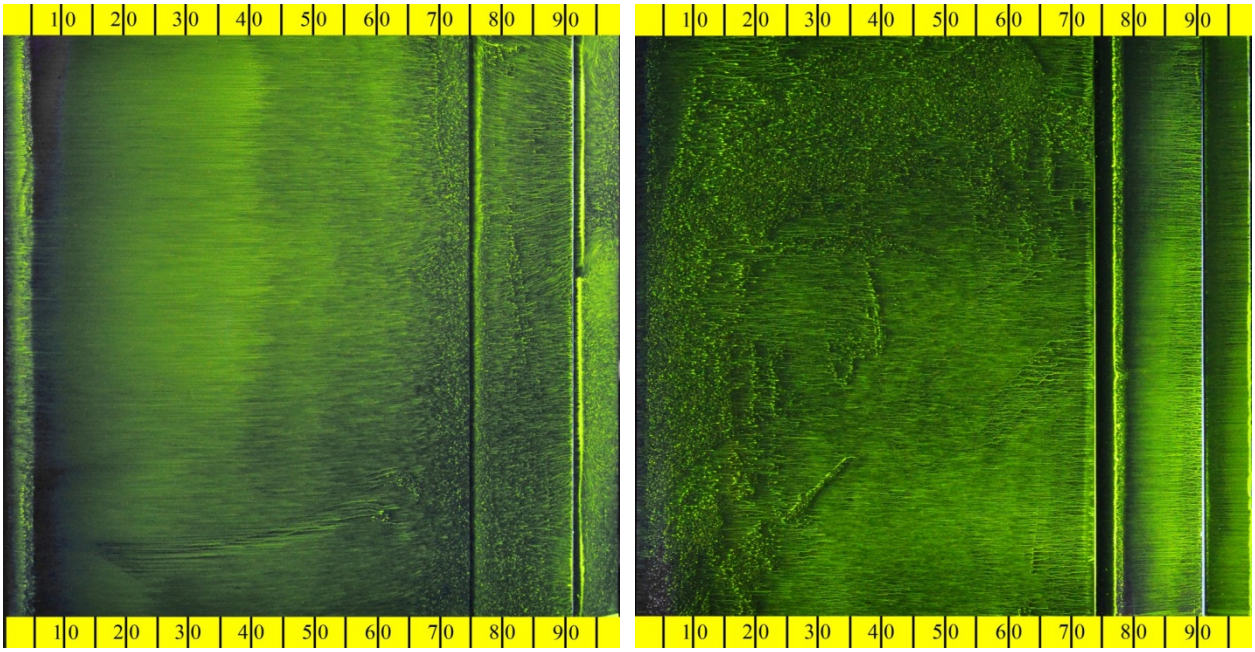

a) **b)**

Fig. 3.27 Flow visualization for δ_f = -10 deg. and δ_t = 30 deg. at α = 13 deg. on a) upper surface and b) lower surface.

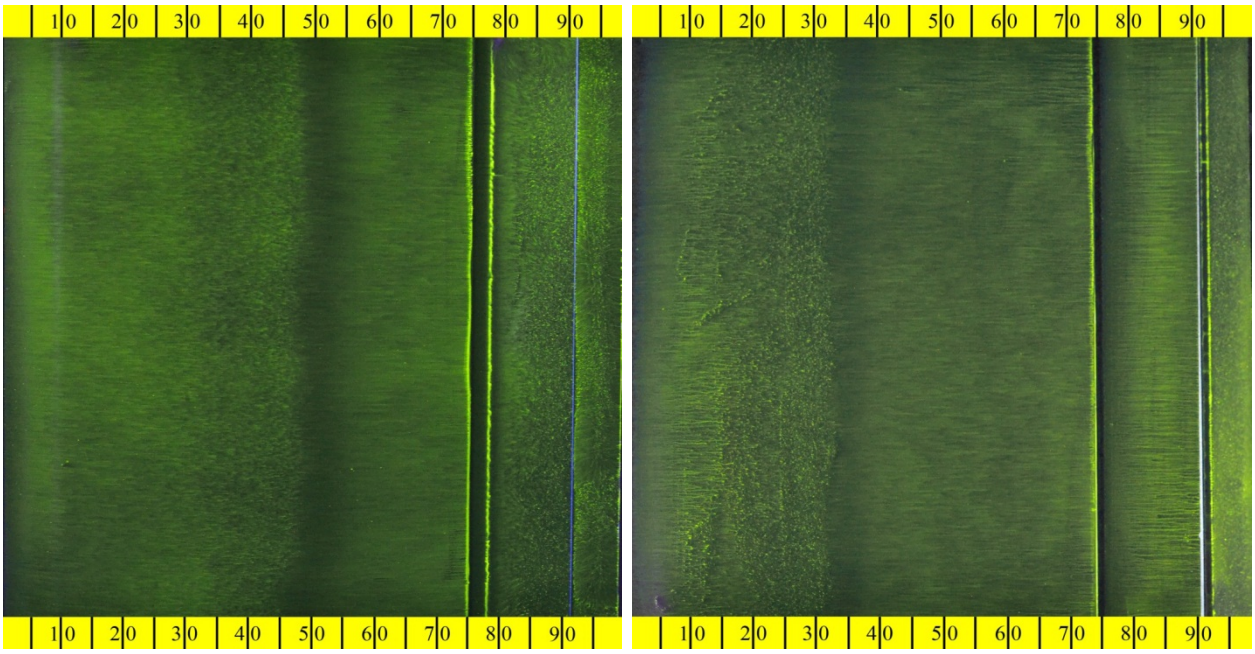

a) **b)**

Fig. 3.28 Flow visualization for δ_f = 10 deg. and δ_t = -30 deg. at α = 0 deg. on a) upper surface and b) lower surface.

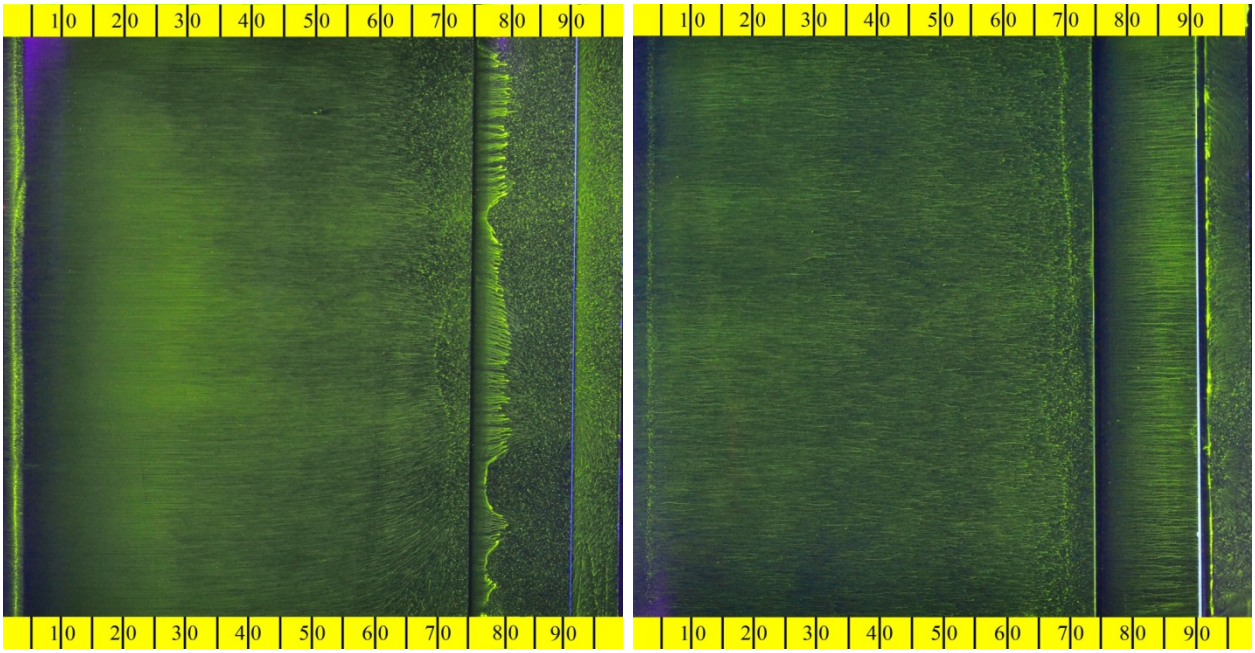

a) **b)**

Fig. 3.29 Flow visualization for δ_f = 10 deg. and δ_t = -30 deg. at α = 14 deg. on a) upper surface and b) lower surface.

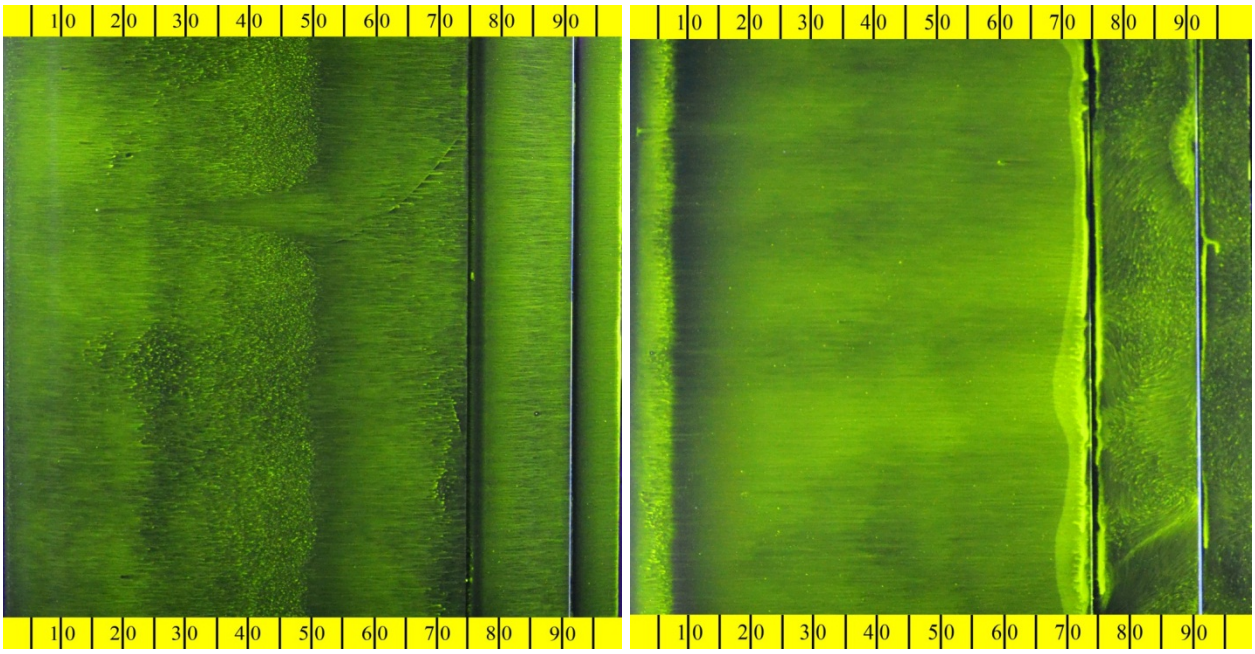

a) **b)**

Fig. 3.30 Flow visualization for δ_f = -30 deg. and δ_t = -30 deg. at α = 0 deg. on a) upper surface and b) lower surface.

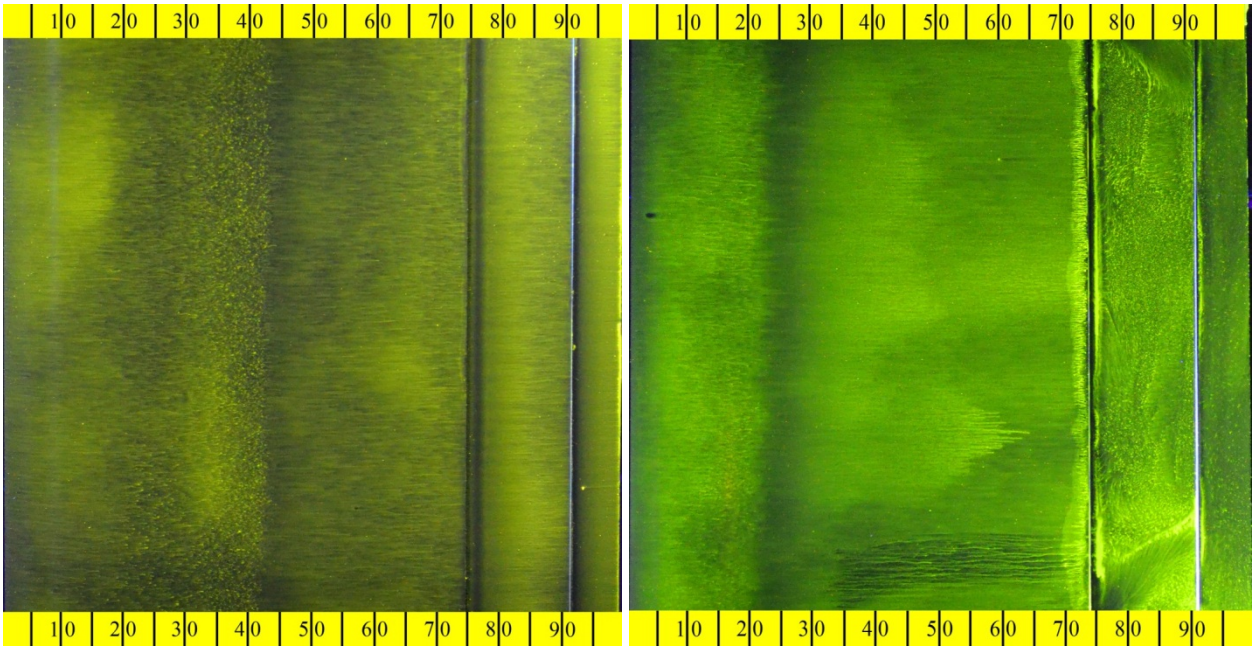

a) **b)**

Fig. 3.31 Flow visualization for δ_f = -30 deg. and δ_t = -30 deg. at α = 4 deg. on a) upper surface and b) lower surface.

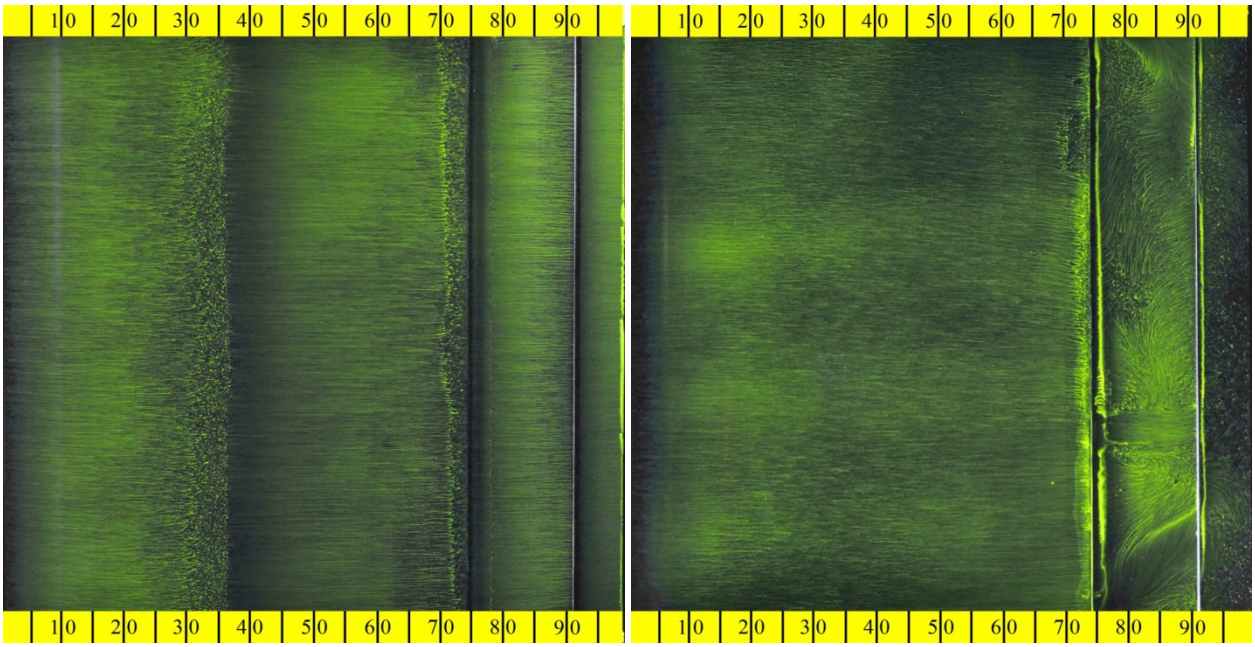

a) **b)**

Fig. 3.32 Flow visualization for δ_f = -30 deg. and δ_t = -30 deg. at α = 7 deg. on a) upper surface and b) lower surface.

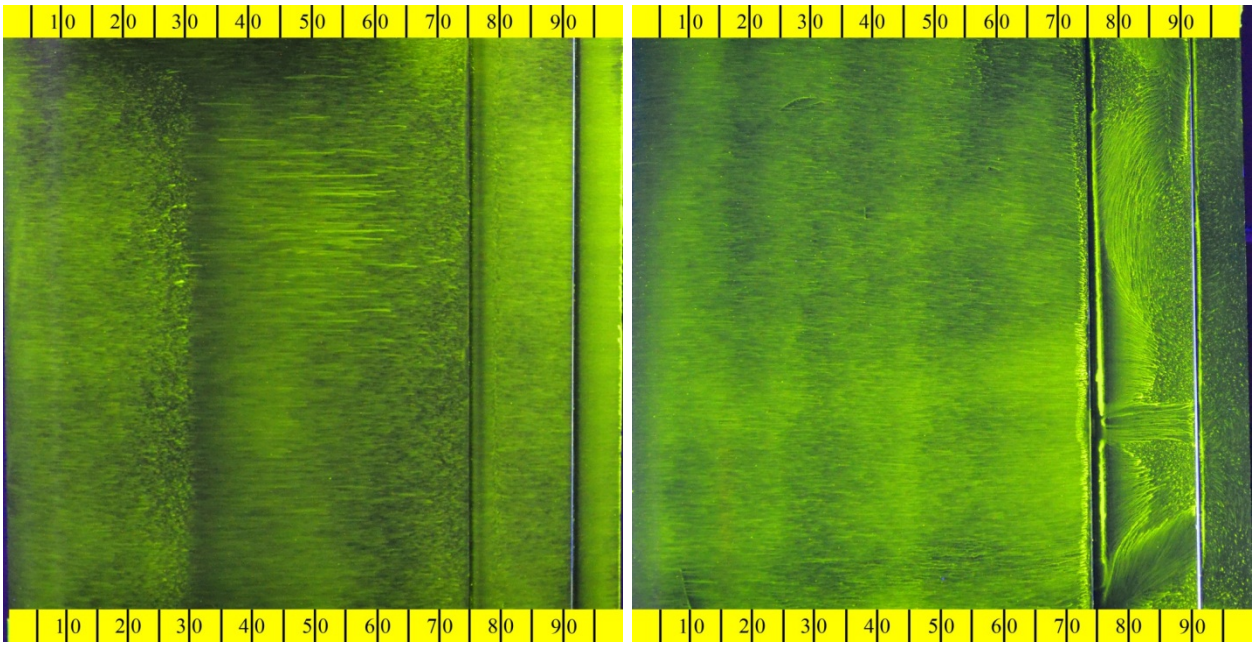

a) **b)**

Fig. 3.33 Flow visualization for δ_f = -30 deg. and δ_t = -30 deg. at α = 10 deg. on a) upper surface and b) lower surface.

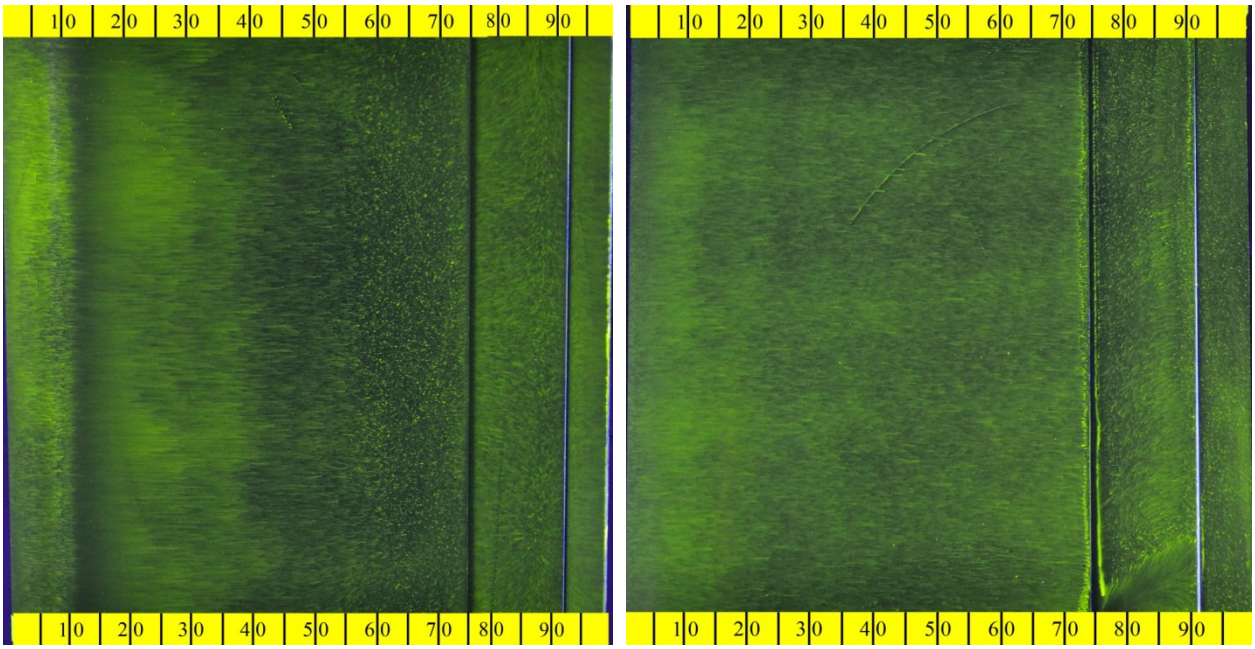

a) **b)**

Fig. 3.34 Flow visualization for δ_f = -30 deg. and δ_t = -30 deg. at α = 14 deg. on a) upper surface and b) lower surface.

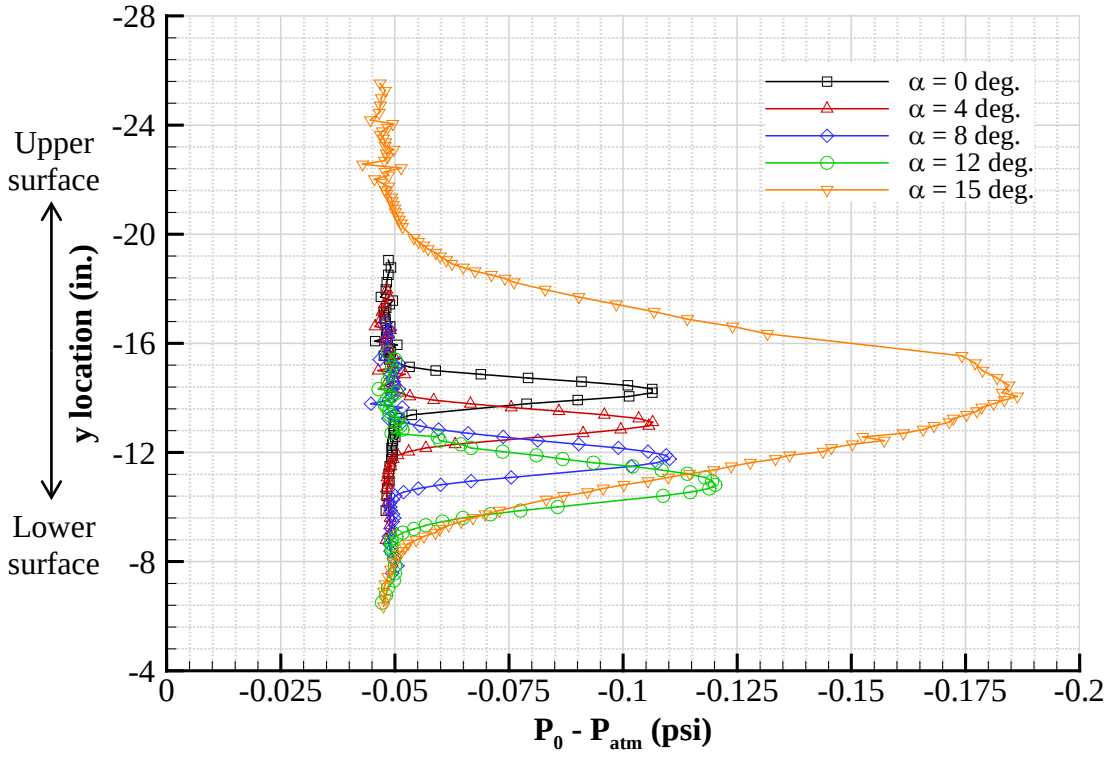

Fig. 3.35 Wake profiles for NACA 3415 with δ_f and δ_t = 0 deg. at several angles of attack.

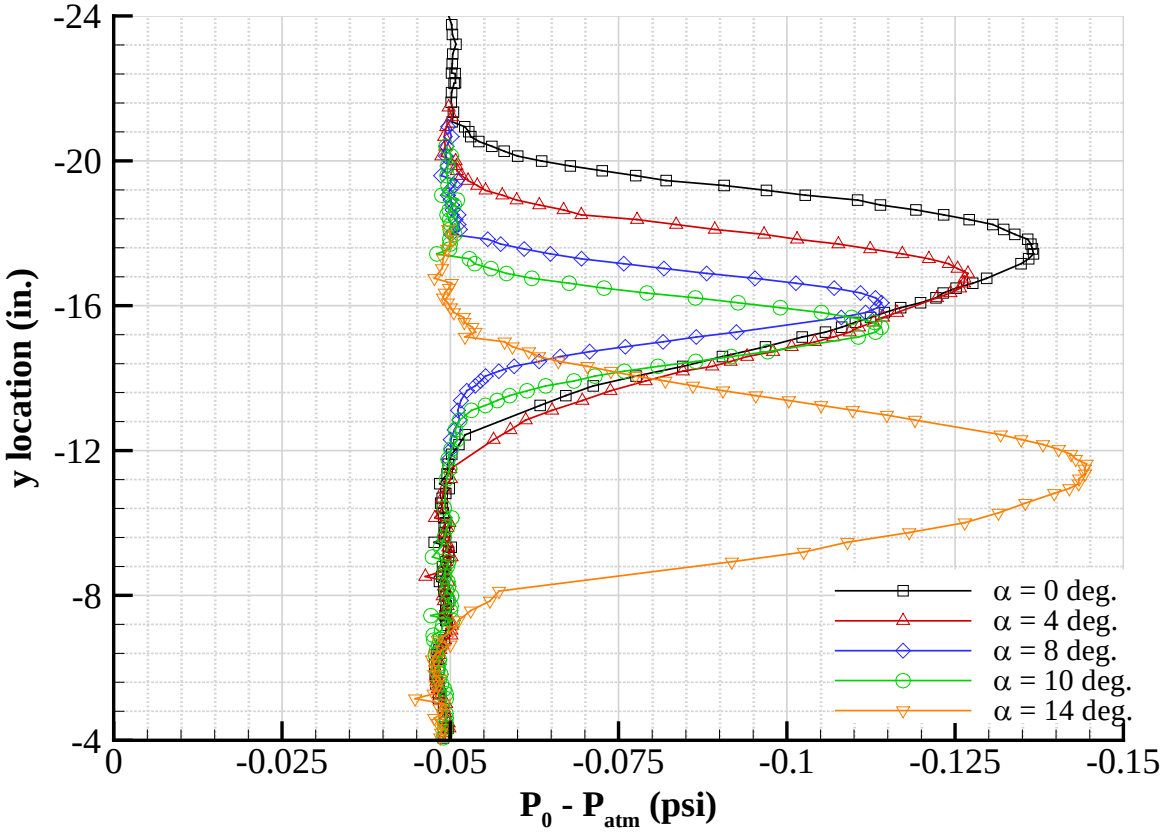

Fig. 3.36 Wake profiles for NACA 3415 with δ_f and δ_t = -30 deg. at several angles of attack.

Chapter 4

Summary, Conclusions and Recommendations

4.1 Summary

This paper presented a study on the feasibility of an airfoil model with a tab-assisted flap used to reduce control power. Two cases were studied: flap with a fixed tab (baseline) which represents the zero tab deflection case, as well as the tabbed case where the tab was actuated to move the flap as well as induce zero hinge moment on the flap. The experiment was conducted in the Illinois 3 by 4 ft. low-speed, low-turbulence wind tunnel with a NACA 3415 airfoil that was modified to include a 25%-chord flap and 25%-flap chord tab. The flap was deflected to 0, ±5, ±10, ±20 and ±30 deg. while the tab was deflected to 0, ±15, ±30, ±45 and ±60 deg. Pressure and force balance measurements were taken to calculate the lift, drag, pitching moment and hinge moments, for both the flap and tab, in both cases. These data were compared to computational fluid dynamic results generated by Winkler, reported by Bottalla et al.[1]

The measurements were then used to evaluate the tab performance in hinge moment reduction and the corresponding tradeoffs in lift and drag. The results revealed a significant reduction in hinge moment between the baseline and tabbed case reaching over 90% in most cases, as seen in Tables 3.1 and D.1. However, the drag was increased in the tabbed case and the lift was greatly reduced. Further analysis was made into the tab effect on lift, which translates into a loss of flap effectiveness, in Section 3.7.2. The lift coefficient was compared and the reduction in lift was calculated for each flap deflection and the corresponding tab deflection for trim (zero flap hinge moment). The flap deflection cases of ±30 deg. were examined additionally through flow visualization to diagnose the cause and revealed the large effect the tab has on the flowfield of the entire airfoil.

A quasi-dynamic study was completed using the static data for two simulated flap deflection schedules: 0 to 30 deg. and 0 to -30 deg. Tab deflections were limited to ±30 deg. Due to the lack of dynamic flap and tab deflections, the power savings could not be calculated in this experiment; therefore, the work savings due to the assistance of a tab were calculated instead. A true dynamic study is proposed for the second phase of this research which will account for the real-time movement of both surfaces and the inertia and unsteady aerodynamics that result. However, the work savings calculated here provided an initial estimate to the power-savings capability of a tab-assisted flap. For both flap deflection scenarios, work savings of 80% and higher were found.

Lastly, an extensive flow visualization investigation was conducted in cases where the data required further examination to explain trends and non-linear behavior. This study was important in understanding the effect of a flap and tab on the NACA 3415 airfoil though it was extraneous to the main research objectives.

4.2 Conclusions

1. The data presented in Sections 3.3 and 3.5 as well as Appendix C revealed substantial influence of a flap and tab on the NACA 3415 aerodynamic performance.
2. The CFD data comparison in Section 3.6 showed good agreement between the computational and experimental data before stall. The addition of unsteady simulations improved the agreement in the lift coefficient greatly but disagreement in the drag coefficient remained due to the effect of transition location movement.
3. Using a tab for assisting the flap resulted in large hinge moment reductions that reached above 90% in most cases but was accompanied with a loss of lift, which was studied further in Section 3.7.2, and an increase in drag.
4. A study of two different flap deflection scenarios revealed potentially high reductions in work required. Even though the calculations incorporated the static data, the results suggest the merit of a tab-assisted flap system and justify the dynamic simulation proposed for the second phase of this research.
5. Overall, the tab had a large influence on the flap effectiveness resulting in large changes in lift. The lift reduction was amplified for the larger flap deflections where larger tab

deflections were required for trim, demonstrating the extensive loading of the tab. At the largest tab deflections, the influence resulted in a reversal of effectiveness in the lift and hinge moment producing results similar to that of the small tab deflections.

6. The non-linear behavior observed in the flap and tab hinge moments for cases in which a positive flap deflection was combined with a larger negative tab deflection and the reverse was due to the complex flowfield progression with angle of attack. Sharp changes in slope with increasing angle of attack were caused by the behavior of the separation bubble formed in the pocket formed by the oppositely deflected surfaces.
7. The drop in drag, referred to as a drag "bucket" in Section 3.7.4.5, seen in the data for the δ_f = -30 and δ_t = -30 deg. case was the result of the laminarization of the main element lower surface, as seen in the flow visualization images. The laminarization reduced the drag from the lower surface as reflected in the wake measurement. This phenomenon was not evident in the computational results due to the location of transition being fixed.

4.3 Recommendations

To fully understand and quantify the benefits of a tab-assisted flap system, future experiments need to be undertaken on true real-time/dynamic flap and tab deflections for accurate simulation of control surface movement, resulting unsteady aerodynamics, and calculations on power consumption. Initial work has been done in preparation for these tests and has shown the difficulty in accurately simulating full-scale deflection schedules at the proper reduced frequency. Since matching the reduced frequency between the scale and full-scale simulations requires flap actuation from 0 to 30 deg. to occur in less than a tenth of a second, a study on the importance of unsteady aerodynamics has on the hinge moments will need to be completed. This study then may allow for longer actuation times that are feasible for this type of experiment while maintaining an accurate simulation.

As the experiment, documented in this paper, was in preparation of the dynamic simulation, it provided lessons on experimental methods as well as methods of model manufacturing. The following recommendations result from these lessons.

1. In the model design, structural integrity of the rapid-prototyped parts is of the utmost importance and a method of balancing rigidity and weight needs to be developed since

the dynamic movement of both control surfaces requires minimized weight and mass moment of inertia.

2. More hinge locations should be designed for both the flap and tab to reduce flex during high loading. The flex in the control surfaces was minimized in this experiment through the addition of a stiffener but was not the most effective method of eliminating the flex. The flap hinge design should also be slightly modified to force only rotational movement of the flap spar as the current design allows for small lateral movement.
3. The slot between the airfoil main element and flap should be reduced to minimize the slot effect which was observed with the flow visualization investigation. The flow at large flap deflections created significant three-dimensionality of the flowfield over the flap and tab.
4. The surface pressure tap density should be increased on the control surfaces, especially on the tab, to allow for improved resolution which would ease the diagnosis of flowfield phenomena.

References

[1] Bottalla, J.R., Bragg, M.B., Sheahan Jr., J.J., and Winkler, C.M., "Performance of an Airfoil with a Power-saving, Tab-assisted Flap System," *29th AIAA Applied Aerodynamics Conference*, Honolulu, HI, June 27 – 30, 2011.

[2] Holtzclaw, R.W. and Crane, R.M., "Wind-Tunnel Investigation of Ailerons on a Low-Drag Airfoil III – The Effect of Tabs," NACA ACR No. 4H15, 1944.

[3] Wenzinger, C.J., "Pressure Distribution over an Airfoil Section with a Flap and Tab," NACA TR-574, 1937.

[4] Jones, R.T. and Nerken, A.I., "The Reduction of Aileron Operating Force by Differential Linkage," NACA TN-586, 1936.

[5] Soulé, H.A. and Hootman, J.A., "A Flight Investigation of the Reduction of Aileron Operating Force by Means of Fixed Tabs and Differential Linkage, with Notes of Linkage Design," NACA TN No. 653, 1938.

[6] Sears, R. I., "Application of Balancing Tabs to Ailerons," NACA WR-L-346, 1942.

[7] Harris, T.A., "Reduction of Hinge Moments of Airplane Control Surfaces by Tabs," NACA TR-528, 1936.

[8] Ansell, P.J., Bragg, M.B., and Kerho, M.F., "Envelope Protection System Using Flap Hinge Moment Measurements," *28th AIAA Applied Aerodynamics Conference*, Chicago, IL, June 28 – July 1, 2010.

[9] Ansell, P.J., "Flight Envelope Protection Using Flap Hinge Moment Measurement," M.S. Thesis, University of Illinois at Urbana-Champaign, 2010.

[10] Sheahan Jr., J.J., Morris, C.E., and Roach, J.M., U.S. Patent Application for "Flight Controls Using Multiple Actuators on Primary Control Surfaces with Tabs," U.S Patent Application, Application No.: 11/953,567, Filed 7 Dec. 2007.

[11] Anderson, J.D., *Introduction to Flight*. McGraw-Hill Book Company, New York, 2007.

[12] Jones, B. M., "Measurement of Profile Drag by the Pitot-Traverse Method," Tech. Rep. 1688, British Aeronautical Research Council Reports & Memoranda, 1936.

[13] Lee, S., "Effects of Supercooled Large Droplet Icing on Airfoil Aerodynamics," Ph.D. Dissertation, University of Illinois at Urbana-Champaign, 2001.

[14] Barlow, J. B., W.H. Rae, J., and Pope, A., *Low-Speed Wind Tunnel Testing*, John Wiley & Sons, Inc., NY, 3rd ed., 1999.

[15] Busch, G.T., "Ice Accretion Aerodynamic Simulation on a Subscale Model," M.S. Thesis, University of Illinois at Urbana-Champaign, 2004.

[16] Jacobs, J. J., "Iced Airfoil Separation Bubble Measurements by Particle Image Velocimetry," Ph.D. Dissertation, University of Illinois at Urbana-Champaign, 2007.

[17] Kline, S. and McClintock, F. A., "Describing Uncertainty in Single-Sample Experiments," Mechanical Engineering, Vol. 75, 1953, pp. 3–8.

[18] Coleman, H. W. and W.G. Steel, J., Experimentation and Uncertainty Analysis for Engineers, Wiley-Interscience, NY, 1989.

Appendix A

Uncertainty Analysis

The experimental uncertainty in the measurements will be detailed in this section. The uncertainty in the measured data was due to two kinds of errors: bias and precision, the sum of which is the total error. However, this analysis could not calculate the absolute error of the experiment but is intended to result in a reasonable approximation of the error in the measured quantities. The bias error is a fixed, systematic error in an instrument in which the data measured favors an outcome. Bias error is commonly due to poor calibration so that the instrument will consistently measure values that are low or high. The precision error, also known as repeatability error, is attributable to an instrument measuring a constant value and outputting varying values.

The uncertainty will be calculated using the second-power equation given by Kline and McClintock[17] as well as Coleman and Steel.[18] To simplify the procedure, the precision error, small relative to the bias error, was considered negligible. Additionally, this procedure does not account for the uncertainty associated with the wind tunnel corrections, defined in Section 2.1.8. The calculated uncertainties of the measured performance characteristics are given in Section A.5.

For a desired result, R, which is a function of several measured values (x_1, x_2, …, x_n), as in Eq. A.1, the resulting uncertainty, U_R, is given by Eq. A.2 below.

$$R = R(x_1, x_2, \ldots x_n) \tag{A.1}$$

$$U_R = \sqrt{\left(\frac{\partial R}{\partial x_1} U_{x_1}\right)^2 + \left(\frac{\partial R}{\partial x_2} U_{x_2}\right)^2 + \cdots + \left(\frac{\partial R}{\partial x_n} U_{x_n}\right)^2} \tag{A.2}$$

The result, R, can also be expressed as shown in Eq. A.3 in which k is a constant and exponents (a, b, c, …) can be positive or negative. Equation A.2 then becomes Eq. A.4.

$$R = k{x_1}^a {x_2}^b {x_3}^c \ldots \tag{A.3}$$

$$\frac{U_R}{R} = \sqrt{a^2\left(\frac{U_{x_1}}{x_1}\right)^2 + b^2\left(\frac{U_{x_2}}{x_2}\right)^2 + c^2\left(\frac{U_{x_3}}{x_3}\right)^2 + \cdots} \tag{A.4}$$

A root-sum-square (RSS) method was used when a single uncertainty result consisted of multiple uncertainties. The RSS uncertainty, $U_{x,RSS}$, is then given by Eq. A.4 below.

$$U_{x,RSS} = \sqrt{{x_1}^2 + {x_2}^2 + \cdots + {x_n}^2} \tag{A.5}$$

The following sections will discuss the uncertainty analysis procedures for the force balance, flap and tab hinge balance, pressure system and wake drag.

A.1 Force Balance Uncertainty

The equations for the calculation of the performance coefficients from the force balance measurements are found in Section 2.1.4. Taking the variables from the equations and inputting into Eq. A.4 produces the following three equations, Eq. A.6 – A.8, below.

$$\frac{U_{C_l}}{C_l} = \sqrt{\left(\frac{U_L}{L}\right)^2 + \left(\frac{U_{q_\infty}}{q_\infty}\right)^2 + \left(\frac{U_b}{b}\right)^2 + \left(\frac{U_c}{c}\right)^2} \tag{A.6}$$

$$\frac{U_{C_d}}{C_d} = \sqrt{\left(\frac{U_D}{D}\right)^2 + \left(\frac{U_{q_\infty}}{q_\infty}\right)^2 + \left(\frac{U_b}{b}\right)^2 + \left(\frac{U_c}{c}\right)^2} \tag{A.7}$$

$$\frac{U_{C_m}}{C_m} = \sqrt{\left(\frac{U_{M_{c/4}}}{M_{c/4}}\right)^2 + \left(\frac{U_{q_\infty}}{q_\infty}\right)^2 + \left(\frac{U_b}{b}\right)^2 + 4\left(\frac{U_c}{c}\right)^2} \tag{A.8}$$

The variables *b* and *c* represent the span and chord, respectively, and were assumed to be measured within 0.02 inches. The dynamic pressure, q_∞, was measured by the PSI pressure system. To solve for the quantities U_L, U_D, and $U_{M,c/4}$; the lift, drag and pitching moment quantities calculated from the normal and axial forces measured by the force balance were put into Eq. A.2. The resulting equations are shown below in Eqs. A.9 – A.11, respectively.

$$U_L = \sqrt{\left(U_{F_N}\cos\alpha\right)^2 + \left(-U_{F_A}\sin\alpha\right)^2 + (-DU_\alpha)^2} \tag{A.9}$$

$$U_D = \sqrt{\left(U_{F_N}\sin\alpha\right)^2 + \left(U_{F_A}\cos\alpha\right)^2 + (LU_\alpha)^2} \tag{A.10}$$

$$U_{M_{c/4}} = \sqrt{{U_M}^2 + \left(x_o U_{F_N}\right)^2 + \left(y_o U_{F_A}\right)^2 - \left(F_N U_{x_o}\right)^2 + \left(F_A U_{y_o}\right)^2} \tag{A.11}$$

The values for the uncertainties in axial force, normal force and pitching moment were given by the manufacturer as 0.02%, 0.03% and 0.15%, respectively, of the full-scale value. These uncertainties then resulted in absolute uncertainty values of 0.09 lbs, 0.027 lbs and 0.0675 ft-lbs for the axial force, normal force and pitching moment, respectively. In addition, the force balance controlled the angle of attack within 0.02 deg.

A.2 Flap and Tab Hinge Balance Uncertainty

To calculate the uncertainty in both the flap and tab hinge balance, a similar method to that used for the force balance was utilized. Since the flap and tab hinge balances were identical in setup, the method described below was used for both balances with the only differences being the load cell and clamp arm lengths. Thus, the subscript, *s*, will again be used to represent the given surface when necessary. The relative uncertainty of the hinge moment coefficient was calculated using Eq. A.12 below, where the variables were obtained from Section 2.1.5 and Eq. 2.11.

$$\frac{U_{C_h}}{C_h} = \sqrt{\left(\frac{U_H}{H}\right)^2 + \left(\frac{U_{q_\infty}}{q_\infty}\right)^2 + \left(\frac{U_b}{b}\right)^2 + \left(\frac{U_{c_s}}{c_s}\right)^2} \tag{A.12}$$

In this case for calculating the uncertainty in the hinge moment (U_H), shown in Eq. 13; the calibration error needed to be accounted for in addition to the precision (operating) error.

$$\frac{U_H}{H} = \sqrt{\left(\frac{U_{H_{Oper}}}{H_{Oper}}\right)^2 + \left(\frac{U_{H_{Cal}}}{H_{Cal}}\right)^2} \tag{A.13}$$

The operating component of the uncertainty is a function of the load cell relative uncertainty ($U_{F,LC}/F_{LC}$), which was provided by the load cell manufacturer, and the relative uncertainty of the moment arm ($U_{d,h}/d_h$). This value was 0.15% of the full-scale value for both the flap and tab hinge balance load cells and resulted in an absolute uncertainty of 0.075 lbs and 0.0337 lbs for the flap and tab, respectively. The calculation of the operating uncertainty is shown below in Eq. 14.

$$\frac{U_{H_{Oper}}}{H_{Oper}} = \sqrt{\left(\frac{U_{F_{LC}}}{F_{LC}}\right)^2 + \left(\frac{U_{d_s}}{d_s}\right)^2} \tag{A.14}$$

The moment arm, d_s, was measured to be 2.97 inches for the flap and 1.675 inches for the tab. This distance was assumed to be measured within 0.02 inches and produces a relative uncertainty of 0.67% and 1.19% for d_s of the flap and tab, respectively.

The calibration uncertainty accounts for the uncertainty in both the applied weights and moment arm as shown below in Eq. A.15.

$$\frac{U_{H_{Cal}}}{H_{Cal}} = \sqrt{\left(\frac{U_{F_h}}{F_h}\right)^2 + \left(\frac{U_{d_h}}{d_h}\right)^2} \tag{A.15}$$

The moment arm for flap hinge balance calibration was measured to be 6.25 inches and was assumed to be measured within .0625 inches while the tab hinge balance was measured at 3.50 inches which was accurate to within 0.03125 inches. The accuracy leads to a relative uncertainty of 1.0% and 0.89% for the flap and tab hinge balance moment arms, respectively. As for the

relative uncertainty in the applied weights, this was determined through the listed uncertainty in the scale used to measure the applied weights. The Ohaus scale consisted of an Ohaus Defender base plate and CD11indicator and measured weights to within ±0.005 lbs. Therefore, this provided the uncertainty, U_F, for each of the four weights applied for the flap calibration (3, 6, 9 and 12 lbs.) and the three weights for the tab (1, 2 and 3 lbs.). The resulting calculation is shown below in Eq. A.16.

$$\frac{U_{F_h}}{F_h} = \sqrt{\left(\frac{U_{F_1}}{F_1}\right)^2 + \left(\frac{U_{F_2}}{F_2}\right)^2 + \left(\frac{U_{F_3}}{F_3}\right)^2 + \left(\frac{U_{F_4}}{F_4}\right)^2} \tag{A.16}$$

A.3 Pressure System Uncertainty

The uncertainty of the performance coefficients derived from measurements taken with the pressure system was due to the conversion of the pneumatic pressures to an analog signal as well the calibration of the pressure system. The conversion uncertainty was given by the ESP unit manufacturer as 0.07% of the full-scale value for the ± 5.0 psid transducer and 0.1% of the full-scale value for the ± 1.0 and ± 0.35 psid transducers. These values result in absolute uncertainties of ± 0.0035, ± 0.001 and ± 0.00035 psid for the ± 5.0, ± 1.0 and ± 0.35 psid units, respectively.

The calibration uncertainty was given for the PCU which calibrates the ESP units and uses the calibrations to convert the analog signal from the ESP units to a pressure value. There were two PCUs used for calibration in this experiment: a 5.0 psid PCU for the ± 5.0 and ± 1.0 psid ESP units and a 1.0 psid PCU for the ± 0.35 psid ESP units. The relative uncertainties for both PSUs were 0.02% of full-scale. Therefore, the resulting absolute uncertainty for the 5.0 psid PCU was ± 0.001 psid and ± 0.0002 psid for the 1.0 psid PSU. The total uncertainty was found by summing the calibration and conversion uncertainties leading to total uncertainties for the ± 5.0, ± 1.0 and ± 0.35 psid ESP units of ± 0.0036, ± 0.0014 and ± 0.0004 psid, respectively.

The uncertainty of the performance coefficients calculated with the pressure measurements was determined using Eqs. 2.24 – 2.26 along with Eq. A.2. The resulting equations for the uncertainty in lift coefficient, quarter-chord pitching moment coefficient and hinge moment coefficient are shown below in Eqs. A.17 – A.19.

$$U_{C_l} = \sqrt{\left(\frac{\partial C_l}{\partial L'} U_{L'}\right)^2 + \left(\frac{\partial C_l}{\partial q_\infty} U_{q_\infty}\right)^2 + \left(\frac{\partial C_l}{\partial c} U_c\right)^2} \tag{A.17}$$

$$U_{C_m} = \sqrt{\left(\frac{\partial C_m}{\partial M'_{c/4}} U_{M'_{c/4}}\right)^2 + \left(\frac{\partial C_m}{\partial q_\infty} U_{q_\infty}\right)^2 + \left(\frac{\partial C_m}{\partial c} U_c\right)^2} \tag{A.18}$$

$$U_{C_h} = \sqrt{\left(\frac{\partial C_h}{\partial H'} U_{H'}\right)^2 + \left(\frac{\partial C_h}{\partial q_\infty} U_{q_\infty}\right)^2 + \left(\frac{\partial C_h}{\partial c_s} U_{c_s}\right)^2} \tag{A.19}$$

For the lift coefficient uncertainty, the lift per unit span (*L'*) was split into the normal and axial components as in Eq. 2.19. The expanded equations for the two components are shown in Eqs. A.20 and A.21 below.

$$F_{N'} = \frac{1}{2}\left[P_1(x_2 - x_1) + \sum_{i=2}^{n-1} P_i(x_{i+1} - x_{i-1}) + P_n(x_n - x_{n-1})\right] \tag{A.20}$$

$$F_{A'} = \frac{1}{2}\left[P_1(y_2 - y_1) + \sum_{i=2}^{n-1} P_i(y_{i+1} - y_{i-1}) + P_n(y_n - y_{n-1})\right] \tag{A.21}$$

Substituting the above equations into Eq. 2.19 provides the following relation in Eq. A.22 for lift per unit span. The corresponding uncertainty for lift per unit span is also shown below in Eq. A.23.

$$\begin{aligned} L' = {} & \frac{1}{2}\cos\alpha\left[P_1(x_2 - x_1) + \sum_{i=2}^{n-1} P_i(x_{i+1} - x_{i-1}) + P_n(x_n - x_{n-1})\right] \\ & - \frac{1}{2}\sin\alpha\left[P_1(y_2 - y_1) + \sum_{i=2}^{n-1} P_i(y_{i+1} - y_{i-1}) + P_n(y_n - y_{n-1})\right] \end{aligned} \tag{A.22}$$

$$U_{L'} = \sqrt{\left(\frac{\partial L'}{\partial \alpha} U_\alpha\right)^2 + \sum_{i=1}^{n} \left(\frac{\partial L'}{\partial P_i} U_{P_i}\right)^2} \tag{A.23}$$

From Eq. A.22, Eq. A.24 was obtained by taking the partial derivative with respect to angle of attack which results in an expression for $\partial L'/\partial \alpha$ in Eq. A.23. The second term in Eq. A.23, $\partial L'/\partial P_i$, was found by taking the partial derivative of Eq. A.22 with respect to pressure which resulted in Eq. A.25.

$$\begin{aligned} \frac{\partial L'}{\partial \alpha} = &-\frac{1}{2}\sin\alpha \left[P_1(x_2 - x_1) + \sum_{i=2}^{n-1} P_i(x_{i+1} - x_{i-1}) + P_n(x_n - x_{n-1})\right] \\ &-\frac{1}{2}\cos\alpha \left[P_1(y_2 - y_1) + \sum_{i=2}^{n-1} P_i(y_{i+1} - y_{i-1}) + P_n(y_n - y_{n-1})\right] \end{aligned} \tag{A.24}$$

$$\frac{\partial L'}{\partial p_1} = \frac{1}{2}\cos\alpha\,(x_2 - x_1) - \frac{1}{2}\sin\alpha\,(y_1 - y_2)$$

$$\frac{\partial L'}{\partial p_i} = \frac{1}{2}\cos\alpha\,(x_{i+1} - x_{i-1}) - \frac{1}{2}\sin\alpha\,(y_{i-1} - y_{i+1}); \quad i = 2, n-1 \tag{A.25}$$

$$\frac{\partial L'}{\partial p_n} = \frac{1}{2}\cos\alpha\,(x_N - x_{N-1}) - \frac{1}{2}\sin\alpha\,(y_{n-1} - y_n)$$

The quarter-chord pitching moment per unit span was found with the same method as the lift per unit span by expanding Eqs. 2.17 and 2.18, shown in Eq. A.26. The uncertainty for the quarter-chord pitching moment per unit span is given as Eq. A.27.

$$M'_{c/4} = \frac{1}{4}\Bigg[P_1\left(x_1^2 - x_2^2 - 2x_1 x_{c/4} + 2x_2 x_{c/4} + y_1^2 - y_2^2\right) + \sum_{i=2}^{n-1}\left[P_i\left(x_{i-1}^2 - x_{i+1}^2 - 2x_{i-1}x_{c/4} + 2x_{i+1}x_{c/4} + y_{i-1}^2 - y_{i+1}^2\right)\right] + P_n\left(x_{n-1}^2 - x_n^2 - 2x_{n-1}x_{c/4} + 2x_n x_{c/4} + y_{n-1}^2 - y_n^2\right)\Bigg] \tag{A.26}$$

$$U_{M'_{c/4}} = \sqrt{\sum_{i=1}^{n}\left(\frac{\partial M'_{c/4}}{\partial P_i}U_{P_i}\right)^2} \tag{A.27}$$

Lastly, the uncertainty for the hinge moment per unit span was found using the same method for both the lift and quarter-chord pitching moment per unit span. The expanded equation for the hinge moment per unit span is shown below in Eq. A.28 and the resulting uncertainty is shown in Eq. A.29.

$$H' = \frac{1}{4}\Bigg[P_1(x_1^2 - x_2^2 - 2x_1x_h + 2x_2x_h + y_1^2 - y_2^2 - 2y_1y_h + 2y_2y_h) + \sum_{i=2}^{n_s-1}[P_i(x_{i-1}^2 - x_{i+1}^2 - 2x_{i-1}x_h + 2x_{i+1}x_h + y_{i-1}^2 - y_{i+1}^2 - 2y_{i-1}y_h + 2y_{i+1}y_h)] + P_{n_s}\left(x_{n_s-1}^2 - x_{n_s}^2 - 2x_{n_s-1}x_h + 2x_{n_s}x_h + y_{n_s-1}^2 - y_{n_s}^2 - 2y_{n_s-1}y_h + 2y_{n_s}y_h\right)\Bigg] \tag{A.28}$$

$$U_{H'} = \sqrt{\sum_{i=1}^{n_s}\left(\frac{\partial H'}{\partial P_i}U_{P_i}\right)^2} \tag{A.29}$$

A.4 Wake Drag Uncertainty

The drag coefficient uncertainty from the wake measurements was found first by combining Eqs. 2.38 and 2.39, as shown below.

$$D' = \sum_{i=1}^{n_{rake}} \left[\sqrt{q_\infty^2 - q_\infty\left(P_{0,\infty} - P_{0,w_i}\right)} + \sqrt{q_\infty^2 - q_\infty\left(P_{0,\infty} - P_{0,w_{i+1}}\right)} - 2q_\infty + 2P_{0,\infty} - P_{0,w_i} - P_{0,w_{i+1}} \right] (y_i - y_{i-1}) \tag{A.30}$$

Equation A.30 was nondimensionalized by dividing by q_∞ and c to attain the wake drag coefficient, below in Eq. A.31.

$$C_d = \frac{1}{q_\infty c} \sum_{i=1}^{n_{rake}} \left[\sqrt{q_\infty^2 - q_\infty\left(P_{0,\infty} - P_{0,w_i}\right)} + \sqrt{q_\infty^2 - q_\infty\left(P_{0,\infty} - P_{0,w_{i+1}}\right)} - 2q_\infty + 2P_{0,\infty} - P_{0,w_i} - P_{0,w_{i+1}} \right] (y_i - y_{i-1}) \tag{A.31}$$

The pressures in the above equation were referenced to the atmospheric pressure, P_{atm}, and the quantity $(2P_{0,\infty} - P_{0,w_i} - P_{0,w_{i+1}})$ can be calculated from measured values directly:

$$2P_{0,\infty} - P_{0,w_i} - P_{0,w_{i+1}} = 2\left(P_{0,\infty} - P_{atm}\right) - \left(P_{0,w_i} - P_{atm}\right) - \left(P_{0,w_{i+1}} - P_{atm}\right) \tag{A.32}$$

Therefore, the resulting uncertainty in the drag coefficient measured by the wake survey system can be given as:

$$U_{C_d} = \sqrt{\left(\frac{\partial C_d}{\partial c} U_c\right)^2 + \left(\frac{\partial C_d}{\partial q_\infty} U_{q_\infty}\right)^2 + \left(\frac{\partial C_d}{\partial P_{0,\infty}} U_{P_{0,\infty}}\right)^2 + \sum_{i=1}^{n_{rake-1}} \left(\frac{\partial C_d}{\partial P_{0,w_i}} U_{P_{0,w_i}}\right)^2} \tag{A.33}$$

To find the above partial derivatives quantities in Eq. A.33, the partial derivative of Eq. A.31 was taken with respect to c, q_∞, $P_{0,\infty}$, and $P_{0,w(i)}$. The results are shown in Eqs. A.34 – A.37 and can be substituted into Eq. A.33 to find the drag coefficient uncertainty.

$$\frac{\partial C_d}{\partial c} = -\frac{1}{q_\infty c^2}\sum_{i=1}^{n_{rake}}\left[\sqrt{q_\infty^2 - q_\infty\left(P_{0,\infty} - P_{0,w_i}\right)} + \sqrt{q_\infty^2 - q_\infty\left(P_{0,\infty} - P_{0,w_{i+1}}\right)} - 2q_\infty + 2P_{0,\infty} - P_{0,w_i} - P_{0,w_{i+1}}\right]\left(y_{i+1} - y_i\right) \tag{A.34}$$

$$\frac{\partial C_d}{\partial q_\infty} = -\frac{1}{q_\infty^2 c}\sum_{i=1}^{n_{rake}}\left[\sqrt{q_\infty^2 - q_\infty\left(P_{0,\infty} - P_{0,w_i}\right)} + \sqrt{q_\infty^2 - q_\infty\left(P_{0,\infty} - P_{0,w_{i+1}}\right)} - 2q_\infty + 2P_{0,\infty} - P_{0,w_i} - P_{0,w_{i+1}}\right]\left(y_{i+1} - y_i\right) + \frac{1}{q_\infty c}\sum_{i=1}^{n_{rake}}\left[\frac{2q_\infty - \left(P_{0,\infty} - P_{0,w_i}\right)}{2\sqrt{q_\infty^2 - q_\infty\left(P_{0,\infty} - P_{0,w_i}\right)}} + \frac{2q_\infty - \left(P_{0,\infty} - P_{0,w_{i+1}}\right)}{2\sqrt{q_\infty^2 - q_\infty\left(P_{0,\infty} - P_{0,w_{i+1}}\right)}}\right]\left(y_{i+1} - y_i\right) \tag{A.35}$$

$$\frac{\partial C_d}{\partial P_{0,\infty}} = -\frac{1}{q_\infty c}\sum_{i=1}^{n_{rake}}\left[2 - \frac{q_\infty}{2\sqrt{q_\infty^2 - q_\infty\left(P_{0,\infty} - P_{0,w_i}\right)}} - \frac{q_\infty}{2\sqrt{q_\infty^2 - q_\infty\left(P_{0,\infty} - P_{0,w_{i+1}}\right)}}\right]\left(y_{i+1} - y_i\right) \tag{A.36}$$

$$\frac{\partial C_d}{\partial P_{0,w_i}} = \frac{1}{q_\infty c}\left[\frac{q_\infty}{2\sqrt{q_\infty^2 - q_\infty\left(P_{0,\infty} - P_{0,w_i}\right)}} - 1\right]\left(y_{i+1} - y_i\right) \tag{A.37}$$

A.5 Sample Uncertainties

In order to demonstrate the propagation of the uncertainty in this experiment, sample uncertainties are shown below in Tables A.1 and A.2. The case selected was for a flap deflection of 5 deg. and tab deflection of 15 deg. at an angle of attack of 4 deg. and Reynolds number of 1.8 x 10^6.

Table A.1 Balance performance coefficient uncertainty.

Coefficient	*Measured Value*	*Absolute Uncertainty*	*Relative Uncertainty*
C_l	0.984	±0.00140	0.14%
C_d	0.0265	±0.000346	1.31%
C_m	-0.132	±0.000612	0.46%
Flap C_h	-0.200	±0.00294	1.47%
Tab C_h	-0.181	±0.00563	3.11%

Table A.2 Pressure system performance coefficient uncertainty.

Coefficient	*Measured Value*	*Absolute Uncertainty*	*Relative Uncertainty*
C_l	0.920	0.00583	0.63%
C_d	0.0198	0.000903	4.56%
C_m	-0.0855	0.00140	1.63%

Appendix B

Flap and Tab System Design

Due to the requirements of the wind-tunnel experiment, the pre-existing flap for the NACA 3415 airfoil model had to be replaced. Since the flap system would have to include a remotely-powered tab, simply modifying the pre-existing flap was not possible. Additionally, future experimentation with dynamic simulation of the flap and tab movement required the flap and tab system to be of minimum mass to allow for control by a reasonable size linear actuator. But the structure of the flap and tab system would have to allow for rapid movement and sustain the aerodynamic loads at the maximum Reynolds number. All of these requirements would have to be at minimum cost.

To minimize weight, material choice was determined to be most important thus eliminating metals as potential options for the majority of the flap and tab system. Aluminum would still be required for the main structure which would handle the loads and tie into the structure of the main element. The cost and structural properties of stereolithography (SLA), a method of rapid prototyping, made it the most appropriate choice to provide the airfoil shape and shell around the aluminum structure. Many materials are available with SLA but the structural requirements of the experiment necessitated the strongest available material. Thus, a polycarbonate-like material Accura® 60 was selected through Realize Inc.© The material and structural properties of the post-cured material are shown below in Table B.1. This method of manufacturing would allow for creation of parts directly from computer-aided design files, therefore, the system could be complex, designed with cavities and surface holes for pressure ports, without concern for increased costs. Incorporating pressure holes which could be instrumented by hand without the need for professional installation further reduced costs of such a flap and tab system.

Table B.1 Material and structure properties of Accura® 60 SLA material.

Measurement	*Condition*	*Value*
Solid Density	@ (77°F)	1.21 g/cm^3
Tensile Strength	ASTM D 638	8410 - 9860 psi
Tensile Modulus	ASTM D 638	390 - 450 ksi
Elongation at Break (%)	ASTM D 638	5 - 13%
Flexural Strength	ASTM D 790	12620 - 14650 psi
Flexural Modulus	ASTM D 790	392 - 435 ksi
Impact Strength (Notched Izod)	ASTM D 256	0.3 - 0.5 ft-lb/in
Hardness, Shore D	N/A	86
Coefficient of Thermal Expansion	ASTM E 831-93	
	TMA (T<Tg, 0 - 40°C)	71 μm/m-°C
	TMA (T<Tg, 75 - 140°C)	153 μm/m-°C

With the material selected for the flap and tab, the detailed design of the structure incorporating both materials followed. Due to the size limits of the SLA machine, each surface would be built in two pieces then joined with epoxy glue. The structure would have to account for the 14 pressure taps and the tubing that would run internally and out of the flap spar for pressure transducer connection. Eleven of the pressure taps would be located in the flap with 3 located in the tab. Beginning with the flap, the needed spanwise break to account for the SLA size limit was placed closest to the location of the taps. This was roughly 40% span from the tunnel floor, as shown in Fig. 2.4, and would allow for access to the cavity where the stainless steel tubing would be fitted to the surface holes. The stainless steel tubing provided a solid connection with the SLA material from which the polyvinyl tubing could be run the remaining length to the pressure transducers. The wall thickness in this cavity was set to 0.10 inches to be the minimum of which the structure could handle. A cross-sectional view of the flap cavity with the pressure holes is displayed below in Fig. B.1.

Alignment tabs, seen in Fig. B.1, were designed into the SLA for installation to ensure the separate flap parts fit correctly with the airfoil aligned. These tabs were also implemented into the tab. The remaining length of the flap had two types of smaller cavities for added strength: one in the location of the flap and tab hinges and one in the remaining areas. The flap and tab hinges, located at 22% and 78% span, needed more additional structure as these locations

handled most of the load. Therefore, the cavities were the smallest at these locations and covered 1.5 inches on each side of the flap hinge location. An example of the cross-section of the hinge location cavity is shown below in Fig. B.2. The other type of cavity used for the remainder of the flap is shown in Fig. B.3 and has larger cavities to reduce weight.

The flap spar was the next part to be designed and would be machined out of general purpose aluminum 6061. The cross-sectional shape, also seen in Figs. B.2 and B.3, was designed in a manner to prevent rotation within the flap SLA structure. To simplify the design, this was done by adding a triangular shape to a circle of 0.75 in. diameter. A hollow cylinder of 0.70 in. diameter integrated into the spar was added to extend below the wind-tunnel floor and allow for the pressure tubing to be run internally. The traverse platform and clamp arm part would then fit around this extension. Machined into the spar were two platforms to which the flap would be mounted to the main element. Details of the spar design can be seen in Fig. B.4. The flap spar was installed in the SLA flap parts with epoxy glue.

The tab design was of the same method but simpler due to the need for only 3 pressure taps. The small thickness of the tab also required it to be solid without cavities; therefore, the pressure lines were modeled internally from surface holes to the bottom of tab where tubing could then be run to the pressure transducer. With the tab being much smaller than the flap, the same hinge system could not be used and the spar could not be continuous in the spanwise direction. Instead, helicoils were implemented to allow for bolts to be fastened to the SLA material directly. A discontinuous spar was then designed to extend from tip to upper hinge location then from that hinge location to the lower hinge location. The spar would then run from the lower hinge location to below the wind tunnel for mounting to actuation system. Aluminum 7075 was chosen for the each of the spars to maximize strength as the maximum allowable spar diameter was 0.25 inches. A drawing of the complete flap and tab system is located below in Fig. B.5.

After several sets of data were taken at a Reynolds number of 1.8 million, the data were compared to previous data, as described in Section 3.1. The comparison exhibited an offset in each of the aerodynamic performance coefficients for the entire linear range of angle of attack. Additionally, the maximum lift coefficient was slightly less than that of the previous experiment. As mentioned in Section 3.1, the cause was determined to be the lateral movement of the flap spar and a stiffener piece was installed on the lower portion of the flap spar which extended

below the clamp arm for the traverse system. The design reduced the lateral movement while avoiding additional friction in the system. This was accomplished by calculating the exact parabolic arc of the flap spar movement over the entire deflection range. The resulting path was accounted in a nylon part that fit inside of a larger bearing. A hole was drilled into the nylon for the flap spar which was offset from the center of the larger bearing, as shown in Fig. B.6. The bearing was then installed in an aluminum piece that was fixed to the force plate such that any forces experienced in the stiffener were accounted for. As the flap spar was rotated to deflect the flap, the natural lateral movement of the spar along the parabolic arc was allowed by the stiffener. When the deflection was reached and the wind tunnel was run, the stiffener would only permit rotation due to the aerodynamic loads and prevent any lateral movement that would affect the hinge moment measurements. This was done with only a slight additional of friction, due to the ball bearing, to the system. A computer-aided design image of the entire assembly is shown below in Fig. B.7.

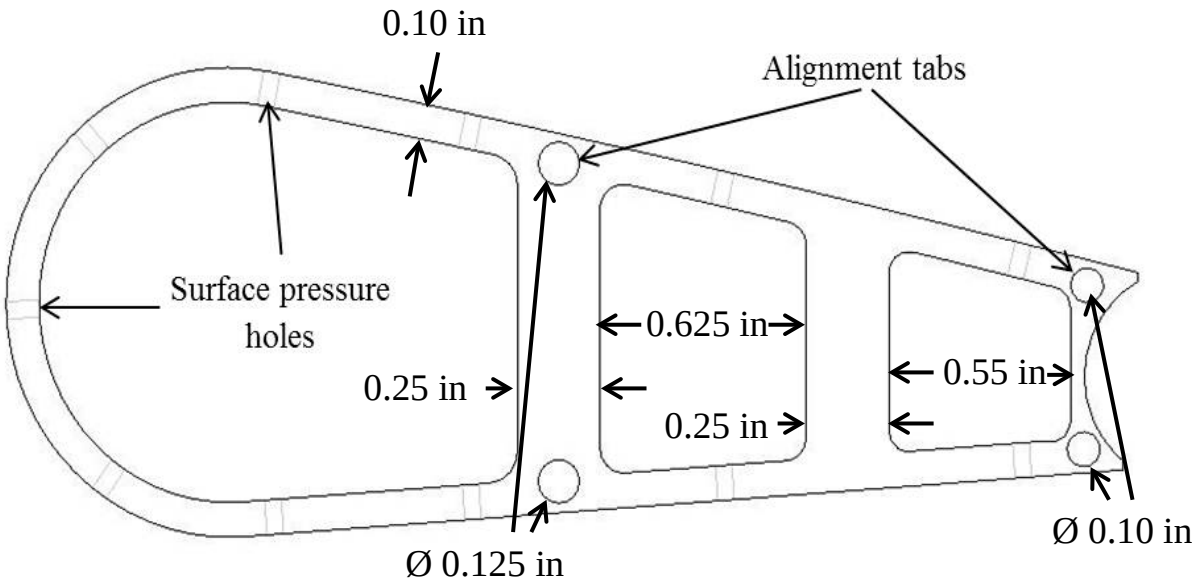

Fig. B.1 Flap cavity for surface pressure holes.

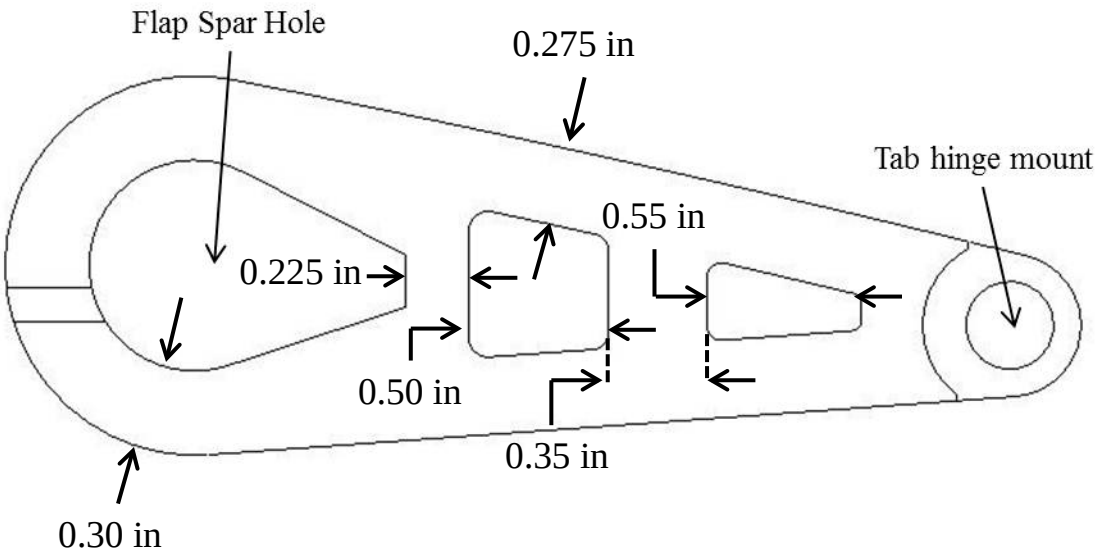

Fig. B.2 Flap cavity for hinge locations.

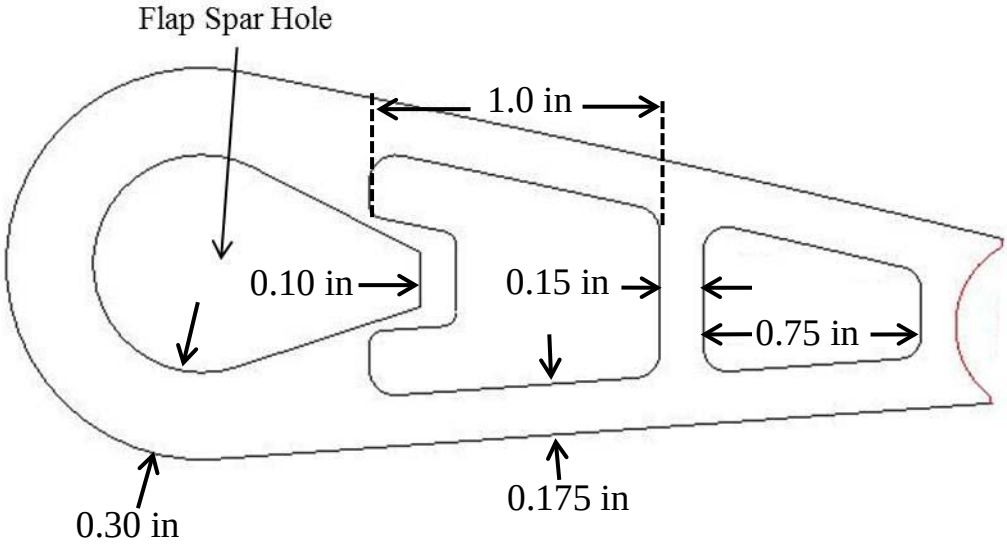

Fig. B.3 Flap cavity for remaining span of flap.

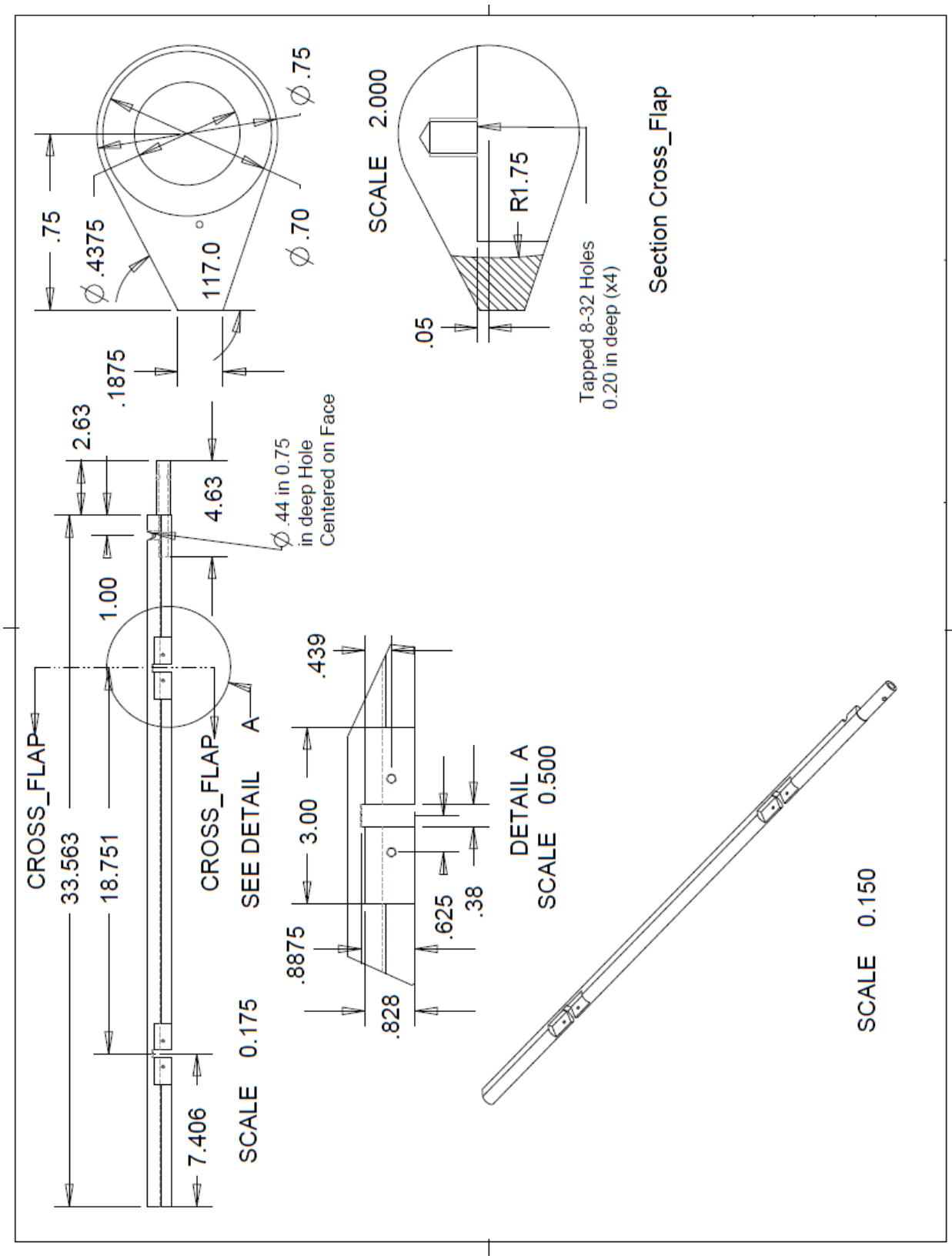

Fig. B.4 Detailed drawing of flap spar design.

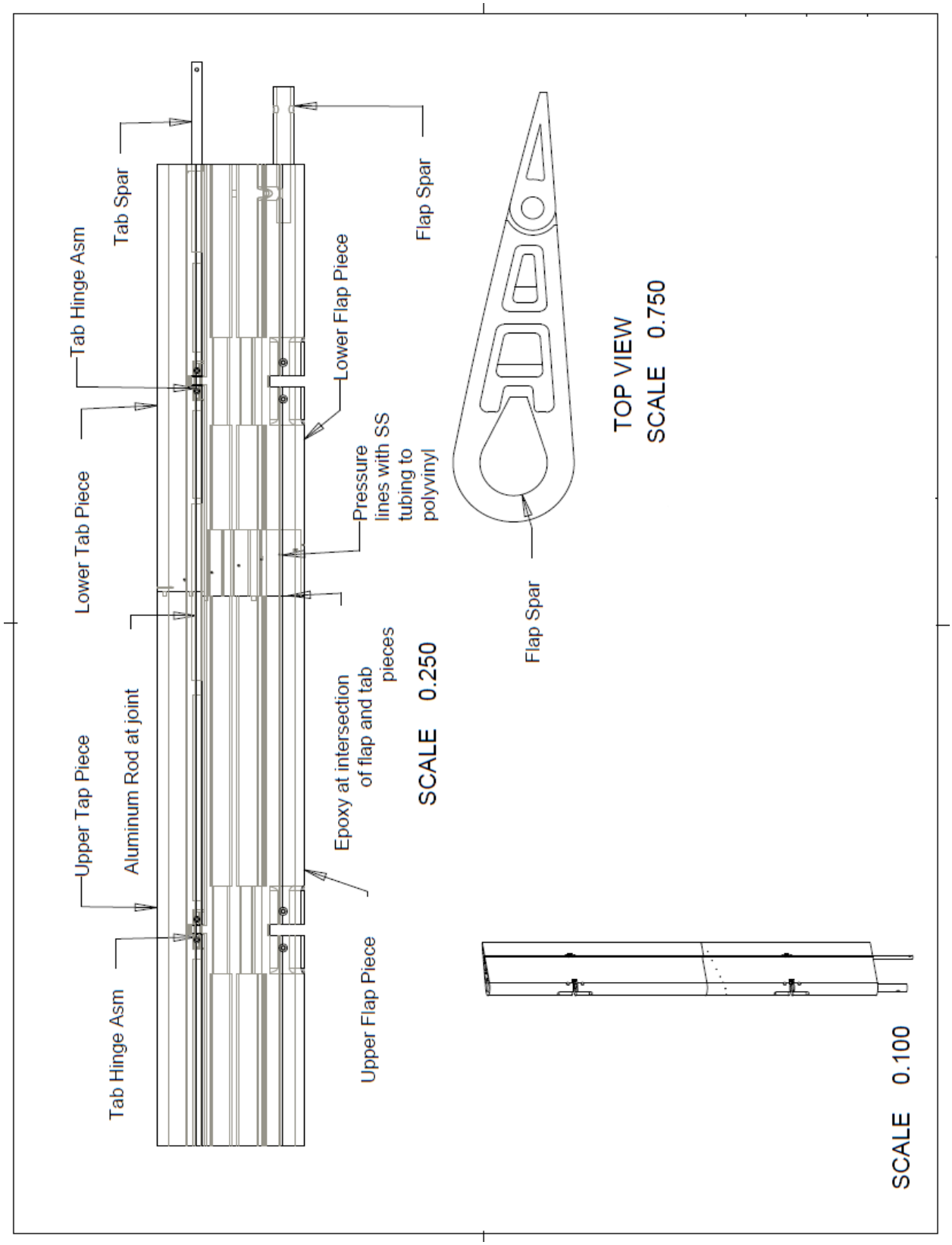

Fig. B.5 Schematic of flap and tab.

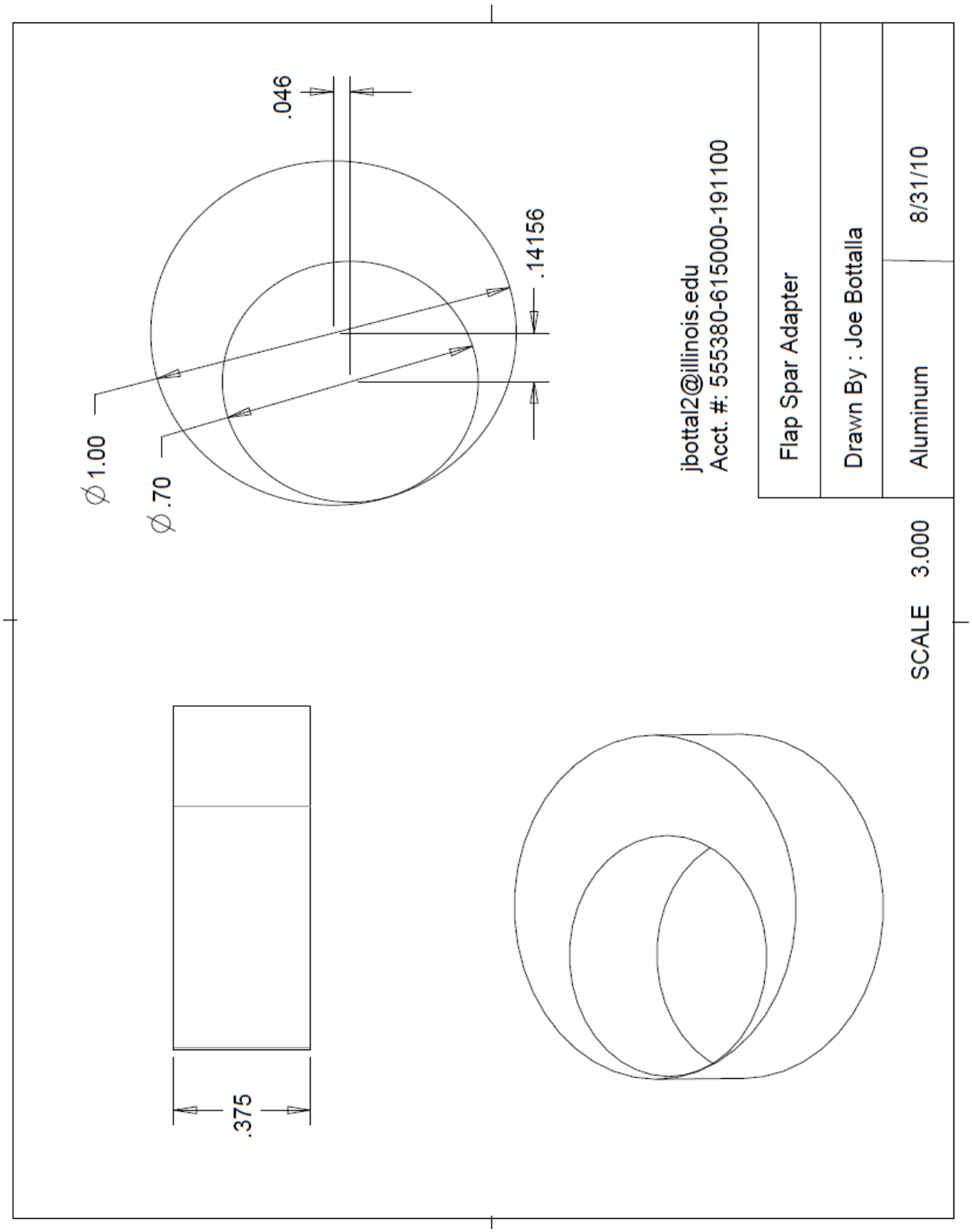

Fig. B.6 Nylon flap spar adapter.

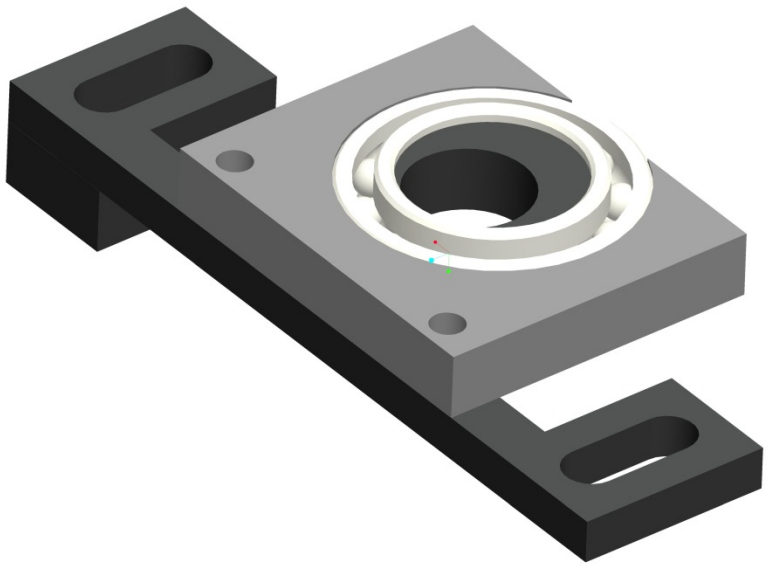

Fig. B.7 Flap spar stiffener assembly.

Appendix C

Additional Data for Tabbed Case

For brevity, the data for the flap deflections of ±5 and ±20 deg. were not included in Section 3.5. Therefore, for reference, the data for the remaining cases are presented below in Figs. C.1 – C.4. Since the tab deflections of ±45 and ±60 deg. were considered ineffective, the data for these deflections is excluded in the below Figures.

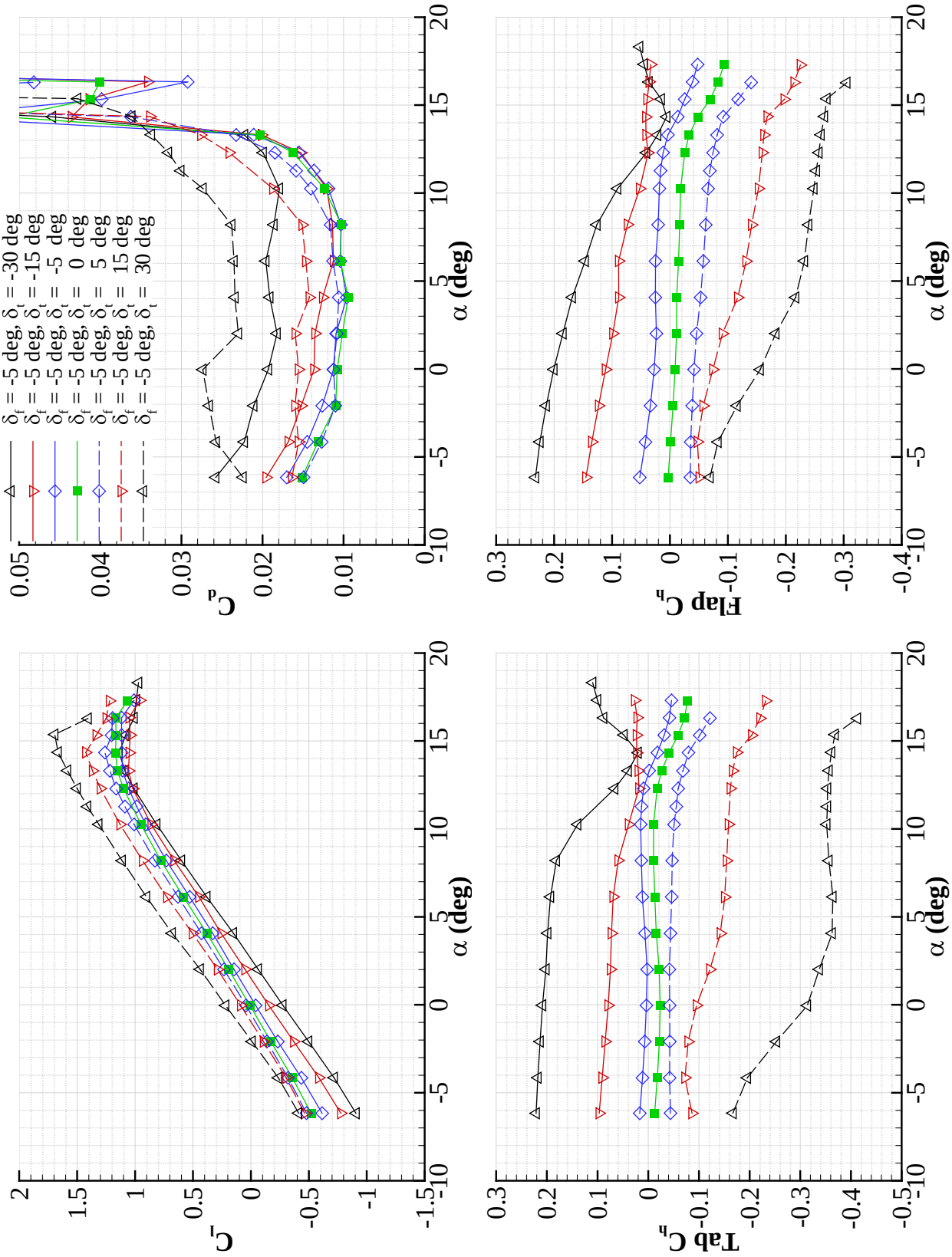

Fig. C.1 NACA 3415 performance with δ_f = -5 deg. and range of tab deflections.

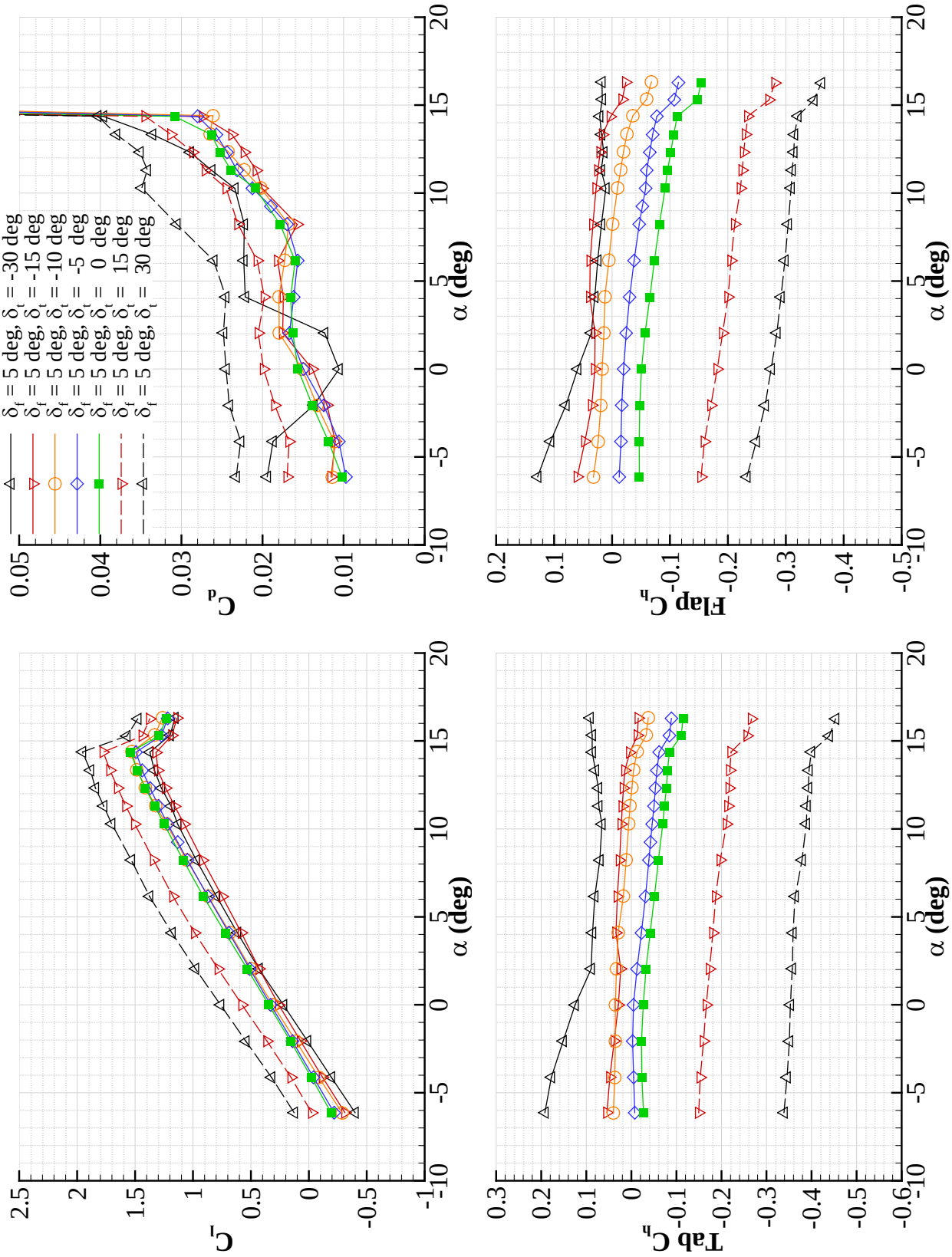

Fig. C.2 NACA 3415 performance with δ_f = 5 deg. and range of tab deflections.

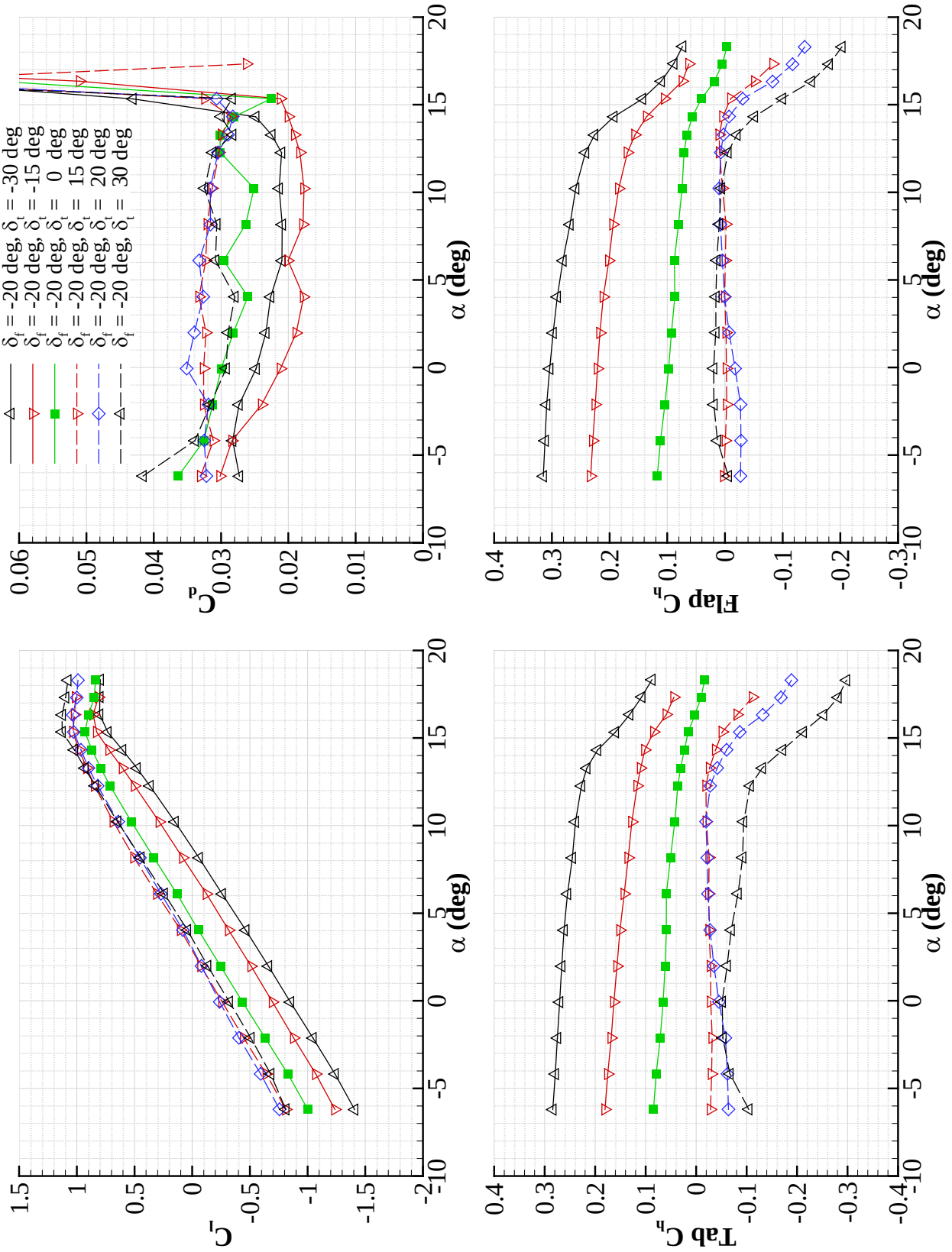

Fig. C.3 NACA 3415 performance with δ_f = -20 deg. and range of tab deflections.

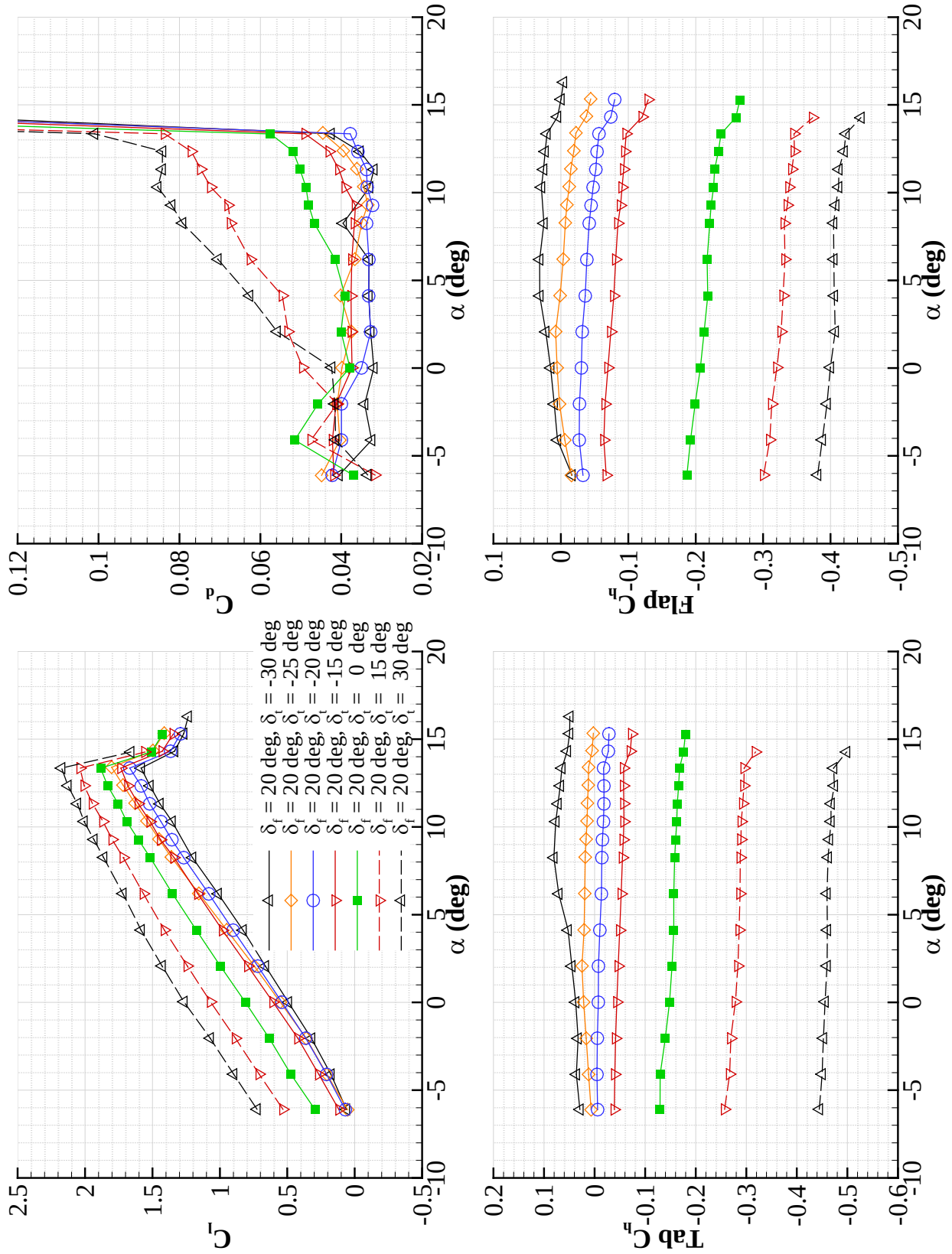

Fig. C.4 NACA 3415 performance with δ_f = 20 deg. and range of tab deflections.

Appendix D

Additional Data for Tab Performance

As mentioned in Section 3.7.1, the tab performance data for flap deflections of 0, ±5, ±20 and ±30 deg. were excluded from Table 3.1. Table D.1 below documents these flap deflections and the data for tab deflection for trim, reduction in hinge moment as well as the effect on lift and drag for several angles of attack.

Table D.1 Effect of using tab on flap hinge moment, drag and lift.

δ_f *(deg.)*	α *(deg.)*	$\delta_{t,trim}$ *(deg.)*	*% Reduction in Hinge Moment*	*% Drag Change*	*% Lift Change*
-30	-4	24	96.52	-4.14	26.51
	-2	25	96.5	12.06	30.87
	0	28	96.24	34.48	37.85
	2	30	96.35	33.52	49.69
	4	30	97.04	25.9	68.81
	6	30	97.45	40.87	183.33
-20	-4	15	98.19	-3.4	23.03
	-2	15	98	4.49	29.95
	0	15	98.05	9.03	40.79
	2	15	97.98	14.18	69.43
	4	15	98.07	27.69	270.6
	6	15	98.13	9.86	140.65

Table D.1 (cont.) Effect of using tab on flap hinge moment, drag and lift.

δ_f *(deg.)*	α *(deg.)*	$\delta_{t,trim}$ *(deg.)*	*% Reduction in Hinge Moment*	*% Drag Change*	*% Lift Change*
-10	-4	4	97.15	3.31	1.66
	-2	3.5	96.61	3.8	5.56
	0	2.5	96.14	2.17	13.76
	2	1.5	94.17	1.59	15.57
	4	1	81.4	1.85	3.96
	6	1	76.77	1.8	3.23
-5	-4	0	N/A		
	-2	0			
	0	-1	86.56	0.93	-83.39
	2	-1.5	91.57	1.96	-7.29
	4	-1.5	94.72	0.63	-4.27
	6	-2	98.51	0.1	-3.69
0	-4	-3.5	99.73	8.82	-32.61
	-2	-4	98.43	8.6	-1126.01
	0	-4	99.29	3.81	-22.58
	2	-4.5	99.73	-1.77	-8.22
	4	-4.5	99.08	-3.42	-3.7
	6	-5	98.8	-2.4	-0.8
5	-4	-7	98.37	-9.17	-327.03
	-2	-7.5	97.77	-7.19	-18.9
	0	-7.5	98.02	-3.21	-7.23
	2	-8	98.27	7.41	-5.3
	4	-8.5	98.59	6.06	-5.19
	6	-9	99.19	6.25	-4.58
10	-4	-12.5	97.88	-3.33	-62.82
	-2	-12.5	98.48	9.81	-39.44
	0	-13	99.06	13.06	-30.26
	2	-13.5	99.42	7.86	-25.35
	4	-14	99.61	11.76	-22.39
	6	-14.5	99.74	15.3	-18.17

Table D.1 (cont.) Effect of using tab on flap hinge moment, drag and lift.

δ_f *(deg.)*	α *(deg.)*	$\delta_{t,trim}$ *(deg.)*	*% Reduction in Hinge Moment*	*% Drag Change*	*% Lift Change*
20	-4	-27.5	99.18	-28.71	-58.63
	-2	-25	99.45	-9.89	-42.95
	0	-24	99.5	2.64	-32.35
	2	-24	99.43	-8.5	-25.86
	4	-25	99.37	2.3	-19.66
	6	-25.5	99.26	-11.38	-15.96
30	-4	-30	99.47	-35.14	-49.84
	-2	-30	99.49	-37.14	-39.25
	0	-30	99.53	-36.07	-32.14
	2	-30	99.57	-36.55	-27.03
	4	-30	99.62	-34.82	-23.39
	6	-30	99.65	-34.13	-20.72